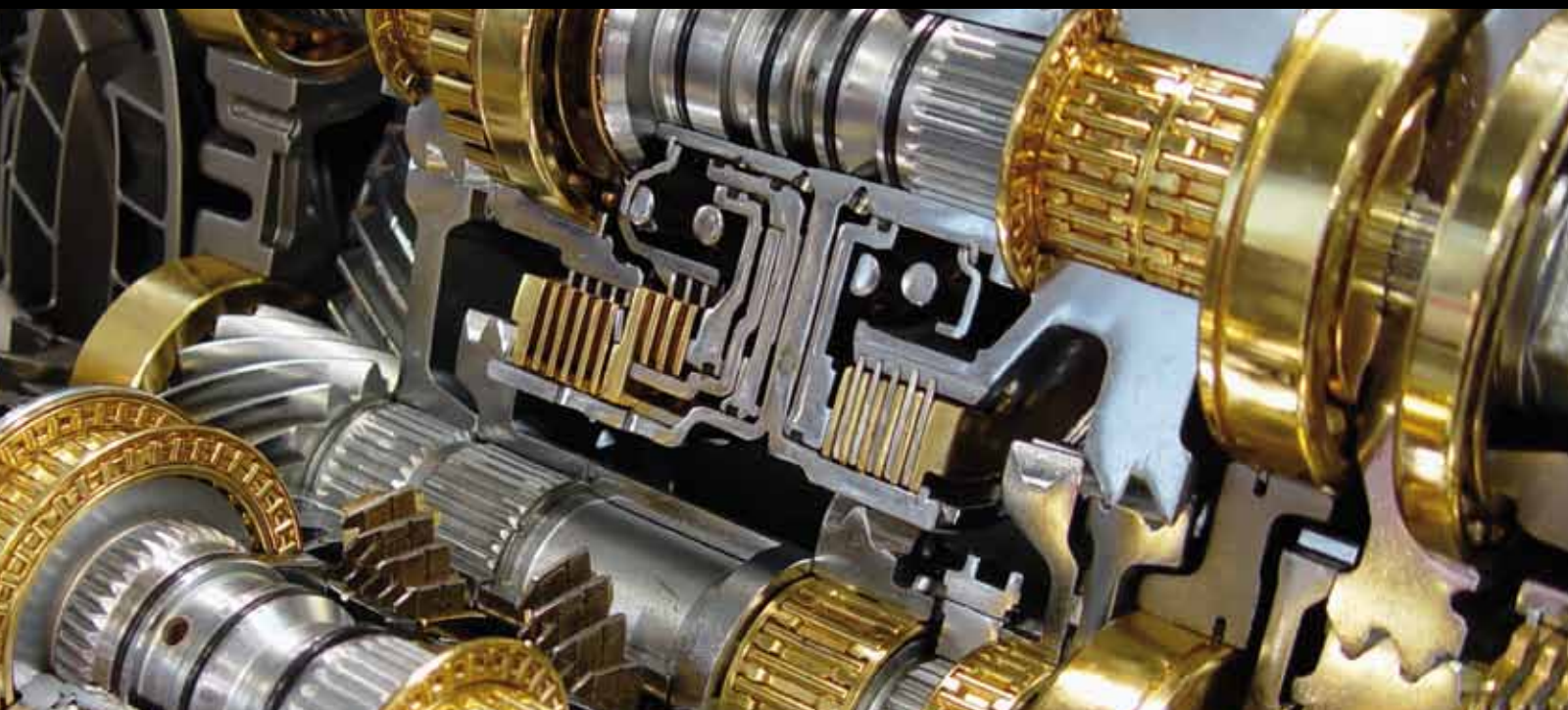


MICRO/NANOTRANSPORT PHENOMENA IN RENEWABLE ENERGY AND ENERGY EFFICIENCY

GUEST EDITORS: C. P. "BUD" PETERSON, CHEN LI, MORAN WANG,
AND GANG CHEN





Micro/Nanotransport Phenomena in Renewable Energy and Energy Efficiency

Advances in Mechanical Engineering

Micro/Nanotransport Phenomena in Renewable Energy and Energy Efficiency

Guest Editors: G. P. "Bud" Peterson, Chen Li, Moran Wang,
and Gang Chen



Copyright © 2010 Hindawi Publishing Corporation. All rights reserved.

This is a special issue published in volume 2010 of "Advances in Mechanical Engineering." All articles are open access articles distributed under the Creative Commons Attribution License, which permits unrestricted use, distribution, and reproduction in any medium, provided the original work is properly cited.

Editorial Board

Koshi Adachi, Japan
Mehdi Ahmadian, USA
Rehan Ahmed, UK
Claude Bathias, France
Adib Becker, UK
Leonardo Bertini, Italy
Liam Blunt, UK
Marco Ceccarelli, Italy
Hyung Hee Cho, South Korea
Seung Bok Choi, South Korea
Bijan K. Dutta, India
Bogdan I. Epureanu, USA
Mohammad Reza Eslami, Iran
Amir Faghri, USA
Ali Fatemi, USA
Siegfried Fouvry, France
Ian A. Frigaard, Canada
Mike Ian Friswell, UK
Yuebin Guo, USA
Zhen Huang, China
Thomas H. Hyde, UK

Jiin-Yuh Jang, Taiwan
Zhongmin Jin, UK
Essam Eldin Khalil, Egypt
Xianwen Kong, UK
Chungxiang Li, China
Jaw-Ren Lin, Taiwan
Cheng-Xian Lin, USA
Oronzio Manca, Italy
Aristide F. Massardo, Italy
Kim Choon Ng, Singapore
Cong Tam Nguyen, Canada
Hiroshi Noguchi, Japan
Andrew Ooi, Australia
Hakan F. Oztop, Turkey
Duc Pham, UK
Homer Rahnejat, UK
Subhash Rakheja, Canada
John E. Renaud, USA
Robert L. Reuben, UK
Bidyut Baran Saha, Singapore
Kazuhiro Saitou, USA

Dik J. Schipper, The Netherlands
Steven R. Schmid, USA
A. Seshadri Sekhar, India
A. A. Shabana, USA
C. S. Shin, Taiwan
Yung C. Shin, USA
Ray W. Snidle, UK
Christian Soize, France
Margaret Stack, UK
Neil Stephen, UK
Kumar K. Tamma, USA
Cho W. Solomon To, USA
Yoshihiro Tomita, Japan
Shandong Tu, China
Moran Wang, USA
Fengfeng (Jeff) Xi, Canada
Hiroshi Yabuno, Japan
Wei M. Yan, Taiwan
Byeng Youn, USA
Zhongrong Zhou, China

Contents

Micro/Nanotransport Phenomena in Renewable Energy and Energy Efficiency, G. P. “Bud” Peterson, Chen Li, Moran Wang, and Gang Chen
Volume 2010, Article ID 170590, 2 pages

Metallic Light Absorbers Produced by Femtosecond Laser Pulses, Anatoliy Y. Vorobyev and Chunlei Guo
Volume 2010, Article ID 452749, 4 pages

A Continuum Model for Water Transport in the Ionomer-Phase of Catalyst Coated Membranes for PEMFCs, Vladimir Gurau and J. Adin Mann Jr.
Volume 2010, Article ID 372795, 16 pages

Experimental and Numerical Study on the Cold Start Performance of a Single PEM Fuel Cell, Calvin H. Li and G. P. Peterson
Volume 2010, Article ID 403816, 11 pages

Mesoscopic Modeling of Multiphysicochemical Transport Phenomena in Porous Media, Qinjun Kang, Moran Wang, Partha P. Mukherjee, and Peter C. Lichtner
Volume 2010, Article ID 142879, 11 pages

Experimental Investigations on the Effects of Cerium Oxide Nanoparticle Fuel Additives on Biodiesel, V. Sajith, C. B. Sobhan, and G. P. Peterson
Volume 2010, Article ID 581407, 6 pages

Effect of Localized Heating on Three-Dimensional Flat-Plate Oscillating Heat Pipe, S. M. Thompson and H. B. Ma
Volume 2010, Article ID 465153, 10 pages

Turbulent Heat Transfer Behavior of Nanofluid in a Circular Tube Heated under Constant Heat Flux, Shuichi Torii
Volume 2010, Article ID 917612, 7 pages

Field Synergy Principle for Energy Conservation Analysis and Application, Qun Chen, Moran Wang, and Zeng-Yuan Guo
Volume 2010, Article ID 129313, 9 pages

Editorial

Micro/Nanotransport Phenomena in Renewable Energy and Energy Efficiency

G. P. “Bud” Peterson,¹ Chen Li,² Moran Wang,³ and Gang Chen⁴

¹The George W. Woodruff School of Mechanical Engineering, Georgia Institute of Technology, Atlanta, GA 30332-0325, USA

²Department of Mechanical Engineering, University of South Carolina, Columbia, SC 29208, USA

³Earth and Environmental Sciences Division, Los Alamos National Laboratory, Los Alamos, NM 87545, USA

⁴Department of Mechanical Engineering, Massachusetts Institute of Technology, MA 02139, USA

Correspondence should be addressed to G. P. “Bud” Peterson, bud.peterson@gatech.edu

Received 8 March 2010; Accepted 8 March 2010

Copyright © 2010 G. P. “Bud” Peterson et al. This is an open access article distributed under the Creative Commons Attribution License, which permits unrestricted use, distribution, and reproduction in any medium, provided the original work is properly cited.

As a result of serious concerns about climate change, high oil prices, and peak oil, energy has become one of the most important issues of our time. Renewable energy and energy-saving technologies are potentially crucial parts of the ultimate solutions to both energy sustainability and climate change. The set of papers in this special issue of “Micro/nanotransport phenomena in renewable energy and energy efficiency” address some of the basic aspects of renewable energy harvest/conversion, emission control, and optimization of energy issues of today.

Contained herein, Vorobyev and Guo [1] develop a new method based on Femtosecond laser to fabricate high-quality metallic light absorbers. This method significantly enhances broadband absorption of electromagnetic radiation by creating a complex of nano- and microstructures. These artificially made surfaces can be used to improve the energy conversion efficiency such as thermophotovoltaics and solar energy absorbers. Hydrogen and fuel cell technologies emerged as one of the most favorable solutions to diversity energy resources and to energy sustainability and environment. Fuel cell technology is a significant component in this special issue. Topics include the experimental and numerical study of cold startup of Proton Exchange Membrane (PEM) fuel cell [2], which is one of most promising solutions for the next generation of purely electric automobiles, development of a continuum model for water transport in the Ionomer-phase of catalyst-coated membranes for PEM [3], and mesoscopic modeling based on the lattice Boltzmann method for water management in

fuel cells [4]. Emission control is attracting more attention and is also addressed in this special issue. Nanosized cerium oxide particles as additives on biodiesel were found to appreciably reduce the emission levels of hydrocarbon and NO_x through enhancing hydrocarbon oxidation and promoting complete combustion [5]. Mesoscopic modeling of multiphysicochemical transport phenomena in porous media based on the lattice Boltzmann method (LBM) has been found to be especially effective to model the dissolving process of supercritical CO₂ into geologic formations such as limestone rock [4], which may provide a comprehensive numerical tool to simulate the long-term fate of CO₂ after injection into the geologic formations. Thermal management is important to concentrated solar technology. Flat-plate oscillating heat pipes are shown to be capable of cooling photovoltaic cells with high concentration ratios because of their superior performance under high-heat flux conditions [6]. Nanoparticles can be used to improve the convective heat transfer at high Reynolds number [7]. The optimization of energy in the end use is included in this special issue since it is important to energy sustainability and the environment. The “field synergy principle” proposed by Guo (see [8–11]) is illustrated to be an effective tool to optimize the energy and mass flow in energy system [12].

G. P. “Bud” Peterson
Chen Li
Moran Wang
Gang Chen

References

- [1] A. Y. Vorobyev and C. L. Guo, "Metallic light absorbers produced by femtosecond laser pulses," *Advances in Mechanical Engineering*, vol. 2010, Article ID 452749, 4 pages, 2010.
- [2] C. H. Li and G. P. Peterson, "Experimental and numerical study on the cold start performance of a single PEM fuel cell," *Advances in Mechanical Engineering*, vol. 2010, Article ID 403816, 11 pages, 2010.
- [3] V. Gurau and J. A. Mann Jr., "A continuum model for water transport in the ionomer-phase of catalyst coated membranes for PEMFCs," *Advances in Mechanical Engineering*, vol. 2010, Article ID 372795, 16 pages, 2010.
- [4] Q. J. Kang, M. R. Wang, P. P. Mukherjee, and P. C. Lichtner, "Mesoscopic modeling of multiphysicochemical transport phenomena in porous media," *Advances in Mechanical Engineering*, vol. 2010, Article ID 142879, 11 pages, 2010.
- [5] V. Sajith, C. B. Sobhan, and G. P. Peterson, "Experimental investigations on the effects of cerium oxide nanoparticle fuel additives on biodiesel," *Advances in Mechanical Engineering*, vol. 2010, Article ID 581407, 6 pages, 2010.
- [6] S. M. Thompson and H. B. Ma, "Effect of localized heating on three dimensional flat-plate oscillating heat pipe," *Advances in Mechanical Engineering*, vol. 2010, Article ID 465153, 10 pages, 2010.
- [7] S. Torii, "Turbulent heat transfer behavior of nanofluid in a circular tube heated under constant heat flux," *Advances in Mechanical Engineering*, vol. 2010, Article ID 917612, 7 pages, 2010.
- [8] Z. Y. Guo, W. Q. Tao, and R. K. Shah, "The field synergy (coordination) principle and its applications in enhancing single phase convective heat transfer," *International Journal of Heat and Mass Transfer*, vol. 48, no. 9, pp. 1797–1807, 2005.
- [9] W. Q. Tao, Z. Y. Guo, and B. X. Wang, "Field synergy principle for enhancing convective heat transfer—its extension and numerical verifications," *International Journal of Heat and Mass Transfer*, vol. 45, no. 18, pp. 3849–3856, 2002.
- [10] Z. Y. Guo, D. Y. Li, and B. X. Wang, "A novel concept for convective heat transfer enhancement," *International Journal of Heat and Mass Transfer*, vol. 41, no. 14, pp. 2221–2225, 1998.
- [11] W. Q. Tao, Y. L. He, Q. W. Wang, Z. G. Qu, and F. Q. Song, "A unified analysis on enhancing single phase convective heat transfer with field synergy principle," *International Journal of Heat and Mass Transfer*, vol. 45, no. 24, pp. 4871–4879, 2002.
- [12] Q. Chen, M. R. Wang, and Z. Y. Guo, "Field synergy principle for energy conservation analysis and application," *Advances in Mechanical Engineering*, vol. 2010, Article ID 129313, 9 pages, 2010.

Research Article

Metallic Light Absorbers Produced by Femtosecond Laser Pulses

Anatoliy Y. Vorobyev and Chunlei Guo

The Institute of Optics, University of Rochester, Rochester, NY 14627, USA

Correspondence should be addressed to Chunlei Guo, guo@optics.rochester.edu

Received 1 April 2009; Accepted 20 August 2009

Academic Editor: Chen Li

Copyright © 2010 A. Y. Vorobyev and C. Guo. This is an open access article distributed under the Creative Commons Attribution License, which permits unrestricted use, distribution, and reproduction in any medium, provided the original work is properly cited.

Using high-intensity femtosecond laser pulses for surface structuring, technologically important metallic light absorbers (dark Au, W, and Ti alloy) with absorption of about 85–95% over a broad wavelength range from ultraviolet to infrared were produced. It was found that the enhanced absorption of the dark metals is caused by a rich variety of nano-/microscale surface structures. The dark metals produced in this study may find a variety of applications in the fields of renewable energy and energy efficiency, such as thermophotovoltaics, solar energy absorbers, thermal radiation sources, and radiative heat transfer devices.

1. Introduction

The femtosecond laser has been shown to be an advanced tool in material processing and micromachining [1–4]. Recently, Vorobyev and Guo have developed a technique that allows to transform highly reflective metals to either totally absorptive or reflecting only a certain color of light, creating the so-called black and colored metals [5, 6]. Among different metallic materials, gold, tungsten, and Ti alloys are materials widely used in many applications. In this paper, by tailoring femtosecond laser-induced surface structures, dark Au, W, and Ti alloy (Ti90/Al6/V4) were produced and their spectral optical properties in the wavelength range of 250–2500 nm were studied. In the entire wavelength range, the absorptance of the darkened metals increases to about 85–95%. These measurements show that the darkened metals have high absorptance in the ultraviolet (uv), visible, and infrared (IR) spectral regions. The study shows that the enhanced absorption of the dark metals is caused by a rich variety of nano-/microscale surface structures. The technique used allows to produce a darkened area as small as a tightly focused laser spot, that is, down to about 10 μm , or as large as needed when a scanning laser beam is employed. The dark metals produced in this study may find a variety of applications in the fields of renewable energy and energy efficiency, such as thermophotovoltaics, solar

energy absorbers, thermal radiation sources, and radiative heat transfer devices.

2. Experimental Setup

Experimental setup for darkening metals is shown in Figure 1. An amplified Ti:sapphire femtosecond laser system that consists of a mode-locked oscillator and a two-stage amplifier including a regenerative amplifier and a two-pass power amplifier was used for surface structuring. To produce surface structures, the laser beam is horizontally polarized and normally focused onto the samples [5, 6]. We studied femtosecond laser darkening of a large area (with a diameter of 24 mm) on metal samples. To produce a large darkened surface area, we use raster scanning of the sample. In our experiment, the sample was moved by an X-Y motorized translation stage. The total reflectance of the blackened sample is measured at a constant light incidence angle of 8° over a wavelength range of 250–2500 nm using a Perkin-Elmer Lambda 900 spectrophotometer with an integrating sphere. Before laser surface treatment, the samples were mechanically polished and further cleaned with methanol. Surface structuring is performed in air at a pressure of 1 atm. Following laser treatment, the topography of surface structural modifications is studied using a scanning electron microscope (SEM).

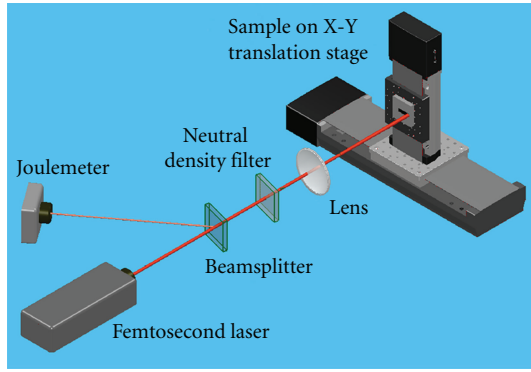


FIGURE 1: Experimental setup for processing of metal samples.

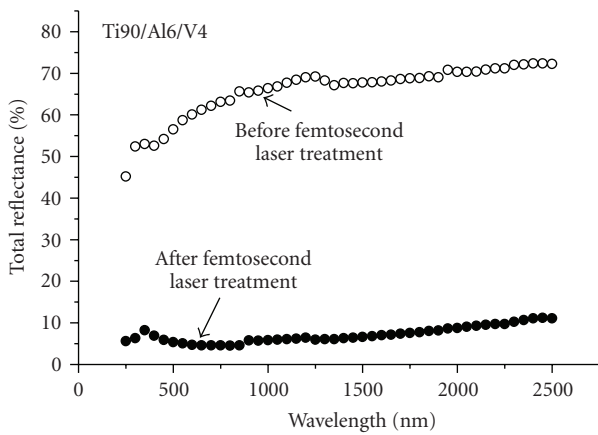


FIGURE 2: Spectral reflectance of the dark Ti90/Al6/V4 alloy as a function of wavelength. For a comparison, the reflectance of the polished sample before laser processing is also shown.

3. Experimental Results and Discussion

The measured total reflectance of darkened samples as a function of wavelength both before and after laser processing is shown in Figures 2, 3, 4. It can be seen that the total reflectance of the darkened samples drops significantly in the entire wavelength range between 250 and 2500 nm, and its new value is below 10% in average. Due to a dramatically decreased reflectance in the visible wavelength range, the treated surface appears pitch black, and a photograph of the darkened tungsten sample is shown in Figure 5 as an example. Note that the surface structures produced in this study are not yet optimized for maximum darkness, and the remaining few percent of the reflectance can be suppressed with further optimization of the processing conditions.

To identify the surface structures that cause metals to appear dark, a detailed SEM study of the surface topography was performed. Representative SEM images of the surface structure for dark gold are shown in Figure 6. The images show that the surface of the dark gold has a rich variety of surface structures, including nano-/microscale voids, nanoprotusions, microscale aggregates of nanoparticles that fuse onto each other and on the metal surface, and periodic grooves with a period equal to the vertical step between the adjacent horizontal scanning lines (about 100 μm as

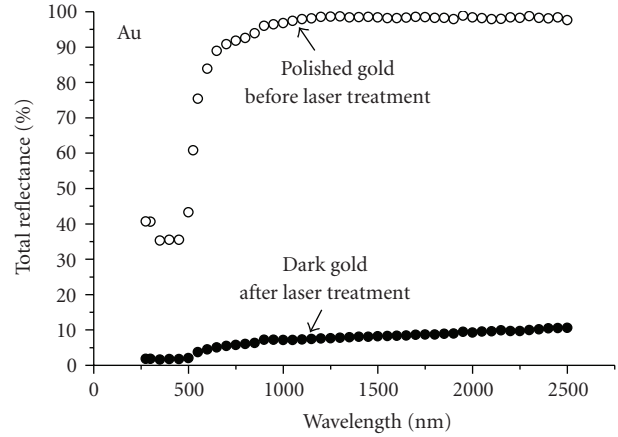


FIGURE 3: Spectral reflectance of the dark gold as a function of wavelength. For a comparison, the reflectance of the polished sample before laser processing is also shown.

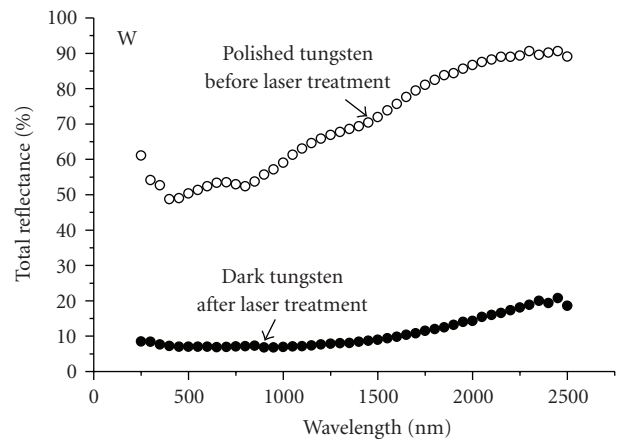


FIGURE 4: Spectral reflectance of the dark tungsten as a function of wavelength. For a comparison, the reflectance of the polished sample before laser processing is also shown.

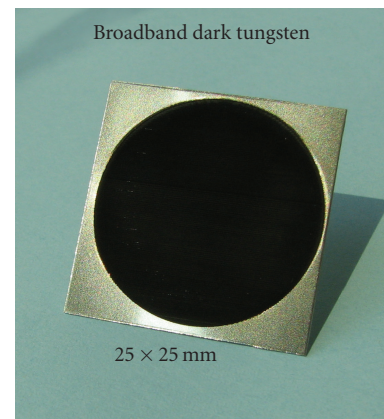


FIGURE 5: Photograph of the broadband dark tungsten sample.

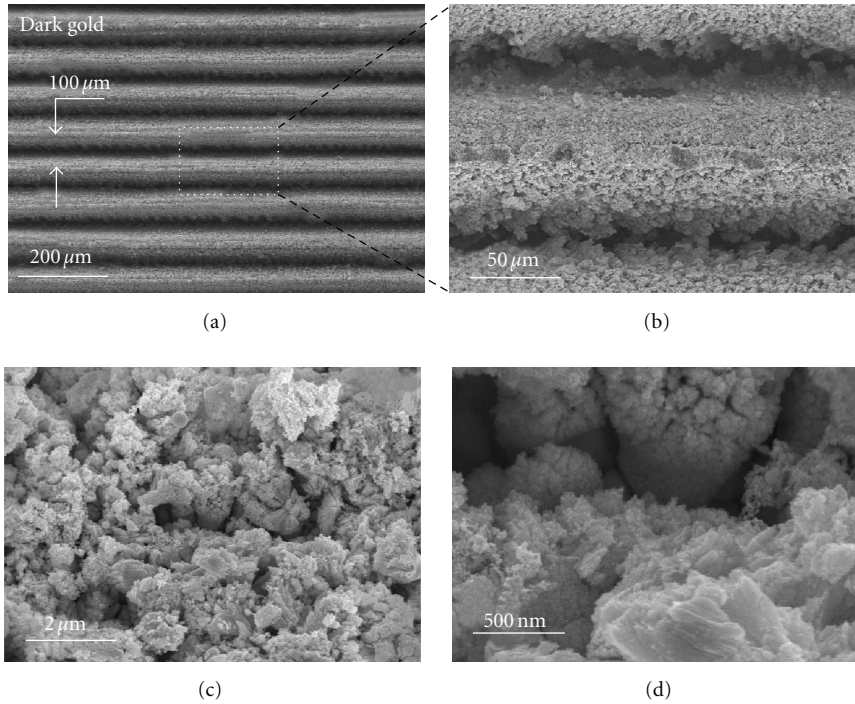


FIGURE 6: SEM images showing surface structural features of the dark gold.

shown in Figure 6(a)). Surface topography of the dark W and Ti90/Al6/V4 alloy is similar to that of the dark Au.

The observed strong broadband absorption due to femtosecond laser-induced surface structures can be explained as follows. The SEM study shows that the size of surface structural features ranges from nanoscale to microscale. Therefore, there are surface structures that are either larger or smaller than light wavelengths. The reduced reflectance observed in the experiments can result from several absorption mechanisms. The surface structures that are smaller than a certain light wavelength can contribute to light absorption due to antireflection effect of random subwavelength surface textures in terms of graded refractive index at the air/solid interface [7]. The surface structures that are smaller than light wavelength can also give rise to the enhanced absorptance due to plasmonic effect [8]. However, in contrast to isolated small metal particles, where surface-plasmon resonances occur at sharp individual frequencies [8], the aggregates of the coalesced nanoparticles of the dark metal cause a broadening of the resonances into a band of frequencies similar to the broadband optical response of random metallic fractals [9]. Another important contribution to the broadband absorptance of the black metal comes from a broadening of surface-plasmon absorption spectra induced by various sizes and shapes of surface nanostructures [10]. Lastly, there are also contributions to absorption from surface structures that are greater than the light wavelength due to trapping of the light in cavities and Fresnel angular dependence of reflection. The overall effect of all these absorption mechanisms results in a strong broadband absorption of electromagnetic waves.

Finally, we note that scanning a high-fluence laser beam across a sample surface can also be used for producing periodic groove structures on metals, as shown in Figure 6(a). The period of these periodic groove structures is determined by the vertical step between the adjacent horizontal scanning lines (about $100\ \mu\text{m}$ for surface structure shown in Figure 6(a)). Using this approach, it is possible to produce periodic groove structures with a period, D , in the range of $10\text{--}1000\ \mu\text{m}$ that provides an additional way to modify optical properties at infrared ($5\text{--}30\ \mu\text{m}$) [11], THz ($30\text{--}300\ \mu\text{m}$) [12], and even longer wavelengths. It is known that surface gratings with their period smaller than light wavelength can enhance absorption through both antireflection mechanism [13] and dissipation of excited surface plasmons polaritons into a metal surface [12]. Therefore, our femtosecond laser surface structuring technology can controllably enhance absorptance of metals from the uv to THz spectral range.

4. Conclusions

In summary, femtosecond laser surface structuring enables us to produce metallic light absorbers, the so-called dark metals, with high absorptance in a broad wavelength range covering uv, visible, and infrared. The enhanced broadband absorption of electromagnetic radiation is due to the creation of a unique combination of surface nano-/microstructures produced by femtosecond laser processing. In our study, the processing conditions for achieving maximum darkness were not optimized, and we believe that the remaining few percent of reflectance can be suppressed with further optimization of the processing conditions. By using this technique, the

size of the darkened surface area can be as small as a tightly focused laser spot, that is, down to about $10\ \mu\text{m}$, or as large as needed when a scanning laser beam is used. The broadband dark metals produced in this study may find a variety of applications in the fields of renewable energy and energy efficiency, such as thermophotovoltaics, solar energy absorbers, thermal radiation sources, and radiative heat transfer devices.

Acknowledgments

This work was supported by the US Air Force Office of Scientific Research and the National Science Foundation.

References

- [1] S. Ameer-Beg, W. Perrie, S. Rathbone, J. Wright, W. Weaver, and H. Champoux, "Femtosecond laser micro structuring of materials," *Applied Surface Science*, vol. 127–129, pp. 875–880, 1998.
- [2] A. Semerok, C. Chaléard, V. Detalle, et al., "Experimental investigations of laser ablation efficiency of pure metals with femto, pico and nanosecond pulses," *Applied Surface Science*, vol. 138–139, no. 1–4, pp. 311–314, 1999.
- [3] B. N. Chichkov, C. Momma, S. Nolte, F. Alvensleben, and A. Tunnermann, "Femtosecond, picosecond and nanosecond laser ablation of solids," *Applied Physics A*, vol. 63, no. 2, pp. 109–115, 1996.
- [4] R. Le Harzic, N. Huot, E. Audouard, et al., "Comparison of heat-affected zones due to nanosecond and femtosecond laser pulses using transmission electronic microscopy," *Applied Physics Letters*, vol. 80, no. 21, p. 3886, 2002.
- [5] A. Y. Vorobyev and C. Guo, "Enhanced absorptance of gold following multipulse femtosecond laser ablation," *Physical Review B*, vol. 72, no. 19, Article ID 195422, 5 pages, 2005.
- [6] A. Y. Vorobyev and C. Guo, "Colorizing metals with femtosecond laser pulses," *Applied Physics Letters*, vol. 92, no. 4, Article ID 041914, 2008.
- [7] F. Ghmari, T. Ghbara, M. Laroche, R. Carminati, and J.-J. Greffet, "Influence of microroughness on emissivity," *Journal of Applied Physics*, vol. 96, no. 5, pp. 2656–2664, 2004.
- [8] U. Kreibitz and M. Vollmer, *Optical Properties of Metal Clusters*, Springer, Berlin, Germany, 1995.
- [9] I. H. Zabel and D. Stroud, "Metal clusters and model rocks: electromagnetic properties of conducting fractal aggregates," *Physical Review B*, vol. 46, no. 13, pp. 8132–8138, 1992.
- [10] S. Lal, S. Link, and N. J. Halas, "Nano-optics from sensing to waveguiding," *Nature Photonics*, vol. 1, no. 11, pp. 641–648, 2007.
- [11] H. Sai, Y. Kanamori, K. Hane, and H. Yugami, "Numerical study on spectral properties of tungsten one-dimensional surface-relief gratings for spectrally selective devices," *Journal of the Optical Society of America A*, vol. 22, no. 9, pp. 1805–1813, 2005.
- [12] F. J. Garcia-Vidal, L. Martín-Moreno, and J. B. Pendry, "Surfaces with holes in them: new plasmonic metamaterials," *Journal of Optics A*, vol. 7, no. 2, pp. S97–S101, 2005.
- [13] N. F. Hartman and T. K. Gaylord, "Antireflection gold surface-relief gratings: experimental characteristics," *Applied Optics*, vol. 27, no. 17, pp. 3738–3743, 1988.

Research Article

A Continuum Model for Water Transport in the Ionomer-Phase of Catalyst Coated Membranes for PEMFCs

Vladimir Gurau and J. Adin Mann Jr.

Chemical Engineering Department, Case Western Reserve University, Cleveland, OH 44106, USA

Correspondence should be addressed to Vladimir Gurau, vxg29@cwru.edu

Received 19 August 2009; Revised 24 November 2009; Accepted 28 December 2009

Academic Editor: Chen Li

Copyright © 2010 V. Gurau and J. A. Mann Jr. This is an open access article distributed under the Creative Commons Attribution License, which permits unrestricted use, distribution, and reproduction in any medium, provided the original work is properly cited.

We study the problem of water transport in the ionomer-phase of catalyst coated membranes (CCMs) for proton exchange membrane fuel cells (PEMFCs), where microscopic-scale phenomena at the distributed interfaces between structural components control the water management. Existing models for water transport in CCMs describe the transport in systems which consist exclusively of an ionomer-phase. Interfacial water fluxes across distributed interfaces representing various mechanisms of water transfer between ionomer and catalyst layer pores are not captured properly in these models. Here we develop a continuum model for water transport in CCMs using the method of volume averaging. Water is exchanged between ionomer and the catalyst layer pores by electro-osmotic discharge (EOD) through the three-phase boundary (TPB) regions and by sorption and desorption across the ionomer-pore interfaces. While the former mechanism does not affect directly the water content in the ionomer-phase, it represents an effective mechanism for water transfer during fuel cell operation and controls directly the water saturation in the catalyst pores.

1. Introduction

Catalyst layers for proton exchange membrane fuel cells (PEMFCs) are heterogeneous porous structures consisting of interpenetrating phases for the transport of electrical charges, electroactive gaseous species, and water. During fuel cell operation, water is transferred between the catalyst layer pores and ionomer by parallel mechanisms. These phenomena control the water management and must be captured in models for water transport in the catalyst layer components. The macroscopic equation for water transport in catalyst coated membranes (CCMs) has been frequently derived for use in computational fluid dynamics (CFDs) simulations, by performing a water flux balance over a control volume representing 100% ionomer-phase. The resulting equation is thus valid solely for the water transport in proton exchange membranes (PEMs) and does not capture the interfacial transport phenomena at subgrid scale which are specific for catalyst layers. The consequence is that some of the mechanisms for water transfer between ionomer and catalyst layer pores have not been conceptualized and quantified

until recently. Moreover, there seems to have been a lack of consensus in the interpretation of the macroscopic equation for water transport in CCMs. The reader is referred to [1, Section 7] of the critical overview of CFD multiphase models for PEMFCs [1]. In the previous modeling works, interfacial transport phenomena *across* the ionomer boundaries have been interpreted as mechanisms of water transport *along* the ionomer-phase, or vice versa. This had a strong impact on the prediction of the water content in the ionomer-phase of CCMs and on the liquid saturation in the diffusion media. The misinterpretation of the effect that various terms have on the prediction of water accumulation in ionomer may be attributed in part to the lack in the literature of a formal derivation of a continuum model for water transport in CCMs.

An objective of this paper is to present a continuum model for water transport in the ionomer-phase of catalyst layers for PEMFCs, starting from the point equations for conservation of charge and for water concentration in ionomer-phase. Another objective is to emphasize various mechanisms of water transfer between the ionomer-phase

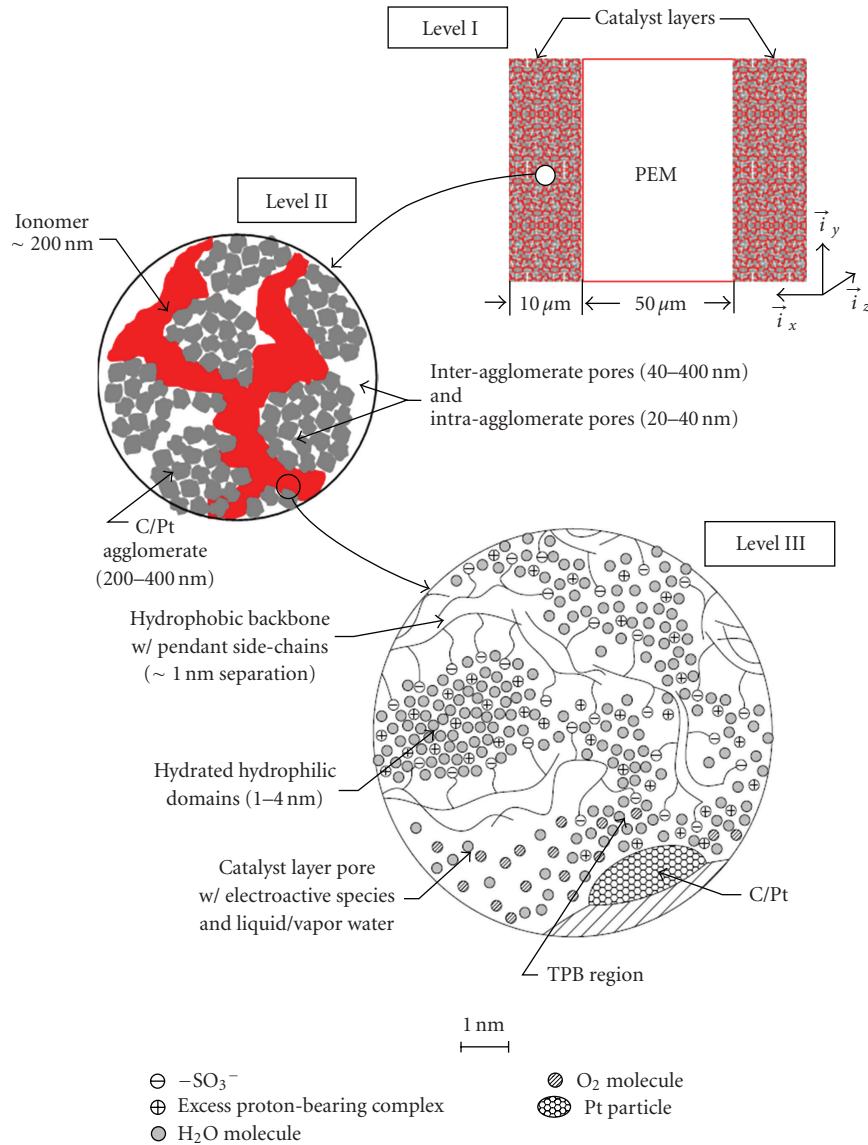


FIGURE 1: Hierarchical structure for catalyst layer system.

and its surroundings, some of which have not been conceptualized and quantified until recently [2–4]. Another objective is to identify those mechanisms that affect water accumulation in the ionomer-phase of the catalyst layer.

The study of water transport in the ionomer-phase of catalyst layers for PEMFCs requires the consideration of a hierarchy of length scales over which significant changes in the parameters related to structure, processes, and operating conditions occur. Figure 1 illustrates the hierarchical structure of the catalyst layer system representative of PEMFCs and some of its characteristic length scales are suggested.

Level I represents a CCM consisting of a PEM impermeable to gases and two catalyst layers bounded on each of its sides. The characteristic length scale associated with this level is the catalyst layer thickness ($\sim 10 \mu\text{m}$), which is the distance over which significant changes in current density, water content, and concentrations of electroactive species

occur. This is the *macroscale* at which the fuel cell operation is modeled and the parameters associated with this level, such as current density, water concentration, or water flux represent *macroscopic, averaged* quantities.

Level II evokes that catalyst layers are porous structures with a random composite morphology, consisting of a mixture of carbon-supported Platinum (C/Pt) and solid ionomer. They provide continuous paths for the protonated complexes to reach the catalyst sites through the ionomer network, for the electroactive species through the porous network and for the electrons through the C/Pt matrix. Level II defines the *microscale* at which the principal microstructural features of the catalyst layer morphology are described. The C/Pt matrix consists of carbon grains (20–40 nm) which form agglomerates of 200–400 nm size. Their porous structure is characterized by a bi-modal pore size distribution, with primary pores of 20–40 nm inside the

agglomerates and secondary pores of 40–400 nm between the agglomerates. The size of the catalyst particles dispersed on the carbon grains is $\sim 2\text{--}5$ nm. Ionomer, due to its molecular size, cannot penetrate the intra-agglomerates, but exist only in the interagglomerate space [5]. Since the electrochemical reactions take place at the three-phase boundary between the gas pores, ionomer and catalyst sites, only the Pt particles in the interagglomerate pores are electrochemically active. During the catalyst fabrication process, the ionomer organizes itself into clusters with diameters of a few hundred nm [6, 7]. The length scale associated with this level is a representative configuration length such as diameter of the C/Pt agglomerate or diameter of the ionomer cluster.

Level III illustrates the ionomer details at *nanometer scale*. The most widely investigated solid ionomers, the perfluorinated sulfonic acid polymers (e.g., Nafion) are heterogeneous media. They consist of a hydrophobic polytetrafluoroethylene framework with pendant side chains ending in sulfonic acid groups $-\text{SO}_3\text{H}$. When exposed to water, the acid groups dissociate and release the protons H^+ into the aqueous subphase while the remaining sulfonate groups $-\text{SO}_3^-$ hydrate. Perfluorinated sulfonic acid polymers separate in hydrophobic and hydrophilic domains. At nanometer-scale, their morphology consists of hydrophobic elongated domains that confer the polymer its morphological stability, and hydrated hydrophilic domains that consist of immobilized, negatively charged sulfonate groups $-\text{SO}_3^-$, water molecules, and mobile proton-bearing complexes. Even at low hydration levels, the hydrophilic domains define a well connected network of nanochannels for proton conduction and water transport. Their diameters range between 1 to 4 nm depending on water content λ , defined as the number of water molecules per sulfonate group. One distinguishes two water environments in the hydrophilic region: (i) the first 6 water molecules per acid group ($\lambda = 6$) representing the hydration water are strongly bound to the $-\text{SO}_3^-$ sites at the inner surface of the hydrophilic domains and can be only removed under vacuum conditions at high temperatures; (ii) additional water ($\lambda > 6$) that fills the volume of the hydrophilic domains behaves like bulk water and is free to equilibrate with the water in the catalyst layer pores, outside the ionomer.

The nanometer-size regions at the interface between ionomer, C/Pt and catalyst layer pores filled with electroactive gaseous species are referred to as three-phase boundary (TPB) regions. These are electrochemically active regions where the hydrogen oxidation reaction (HOR) or the oxygen reduction reaction (ORR) takes place. These regions are dynamic and their behavior depends on the hydration state of the ionomer. At the interface, the $-\text{SO}_3^-$ -ending side chains of the ionomer structure unfold towards the Pt particles as the water content in the ionomer increases and the interfacial region becomes hydrophilic [8]. At the cathode, the TPB regions contain (i) protonated complexes emerging from the hydrophilic domains of the ionomer and engaging in the ORR at the Pt surface, (ii) water molecules introduced in the interfacial region by the protonated complexes via electro-osmotic drag, (iii) water molecules produced in the ORR and desorbed from the Pt surface, and

(iv) oxygen molecules diffusing from the catalyst layer pores and engaging in ORR at the Pt surface.

At the nanometer-scale level, proton transfer is interpreted as a combination of proton transport in bulk-like water and interfacial interactions with the $-\text{SO}_3^-$ groups at the polymer-water interface [9]. Membranes at a high degree of hydration exhibit proton transport resembling that in bulk water [10]. In water, excess protons H^+ hydrate to form hydronium ions H_3O^+ , which in turn are hydrogen bonded to the three water molecules in its first solvation shell and form Eigen clusters H_9O_4^+ . Fluctuations between Eigen and Zundel (H_5O_2^+) complexes generate a transport mechanism for protons along the hydrogen bond network called the Grotthus mechanism or structure diffusion [10]. When an electrical field is applied, the structure diffusion relays the protons in the direction of the field along the hydrogen bond network without inducing a concerted transport of the water molecules. In addition to this mechanism, the electrical field exerts electrokinetic body forces on the protonated complexes, superposing a hydrodynamic motion of the protons over the structure diffusion. This transport is called the vehicle mechanism. The proton flux caused by structure diffusion and vehicle mechanism $\vec{N}_{\text{H}^+} = \vec{N}_{\text{H}^+}^{\text{struct diff}} + \vec{N}_{\text{H}^+}^{\text{veh mech}}$ generates a current density along the ionomer from anode to cathode $\vec{i} = \vec{N}_{\text{H}^+} F$.

The distribution of excess protons relative to the immobile $-\text{SO}_3^-$ groups is the result of electrostatic attractive interactions between the counterions and structural inhomogeneities in the vicinity of the electrified interface. The decreased dielectric constant in the interfacial region determines a stabilization of excess protons away from the fixed sulfonate groups, towards the center of the channels [11]. Since water within the hydrophilic regions of the ionomer and liquid water outside the ionomer forms a continuous medium, it has been postulated [12] that excess protons could leave the ionomer and migrate throughout the liquid water in the catalyst layer pores, towards the Pt sites in the C/Pt intra-agglomerates. These are regions where ionomer, due its molecular size cannot penetrate. This is an intriguing hypothesis, since it leads to the conclusion that all the Pt sites, including those in the TPB regions and those in the intra-agglomerates are electrochemically active. This hypothesis however, breaches the condition of electroneutrality. In liquid water, one expects a total depletion of protons within 1-2 nm away from the most peripheral array of sulfonate groups [11]. We will consider that protons may exit the hydrophilic domains of the ionomer into the adjacent liquid water, but will continue to migrate within a few nanometers away from the most peripheral array of $-\text{SO}_3^-$ groups towards the TPB regions. This thin layer of liquid water (1-2 nm thick) may be assimilated to the hydrophilic domains and may be considered to be integral part of the ionomer.

In their motion generated by the vehicle mechanism, excess protons carry the water molecules in their solvation shells as well as other water molecules due to viscous interactions, generating a water transport mechanism called electro-osmotic drag. The electro-osmotic drag coefficient

n_{drag} is defined as the ratio of the water flux $\vec{N}_{\text{H}_2\text{O}}^{\text{drag}}$ through the ionomer to the flux of protons \vec{N}_{H^+} when current is passed under conditions of no water concentration gradient. The flux of water induced by electro-osmotic drag increases the water concentration along the ionomer from anode to cathode. This effect is balanced by the chemical diffusion of water, $\vec{N}_{\text{H}_2\text{O}}^{\text{diff}} = -D_{\text{H}_2\text{O}} \nabla c_{\text{H}_2\text{O}}$, which acts in the direction from regions with higher water concentration towards regions with lower water concentration.

Whereas at nanometer scale (Level III) the ionomer represents a heterogeneous system with the characteristic length of only a few nanometers, the average size of the ionomer clusters (~ 100 nm) is large enough so that at the microscale (Level II) the ionomer-phase may be considered homogeneous. The consequence of this assumption is that one may prescribe *microscopic, point equations* for the transport of protons and water in the ionomer-phase. This is considered a trivial practice when modeling transport phenomena in PEM systems consisting of 100% ionomer-phase, in which case the microscale (Level II) and macro scale (Level I) are indistinguishable. In the case of catalyst layers, the microscopic point equations governing the transport in the ionomer-phase at micro scale (Level II) must be solved along with the boundary conditions describing various mechanisms of water and proton transport across ionomer-TPB and ionomer-catalyst layer pore interfaces. However, this direct analysis is impractical due to the complex morphology of the catalyst. The practical solution is to apply the method of volume averaging [13–18] for the derivation of continuum transport equations that are valid anywhere in the catalyst layer. These transport equations, called *volume-averaged equations*, may be solved at the macro scale (Level I) and allow the consideration of the catalyst layer as a macro-homogeneous domain. The volume-averaged equations retain the information regarding interfacial transport across ionomer-phase boundaries.

In the following sections we will present the local, microscopic equations governing proton and water transport in *ionomer-phase* (Level II) along with their boundary conditions and we will derive the volume-averaged equations for conservation of charge and water transport in *catalyst layers* (Level I). The scope of this analysis is to emphasize various mechanisms of water transfer between the ionomer-phase and its surroundings, some of which have not been conceptualized and quantified until very recently. For this analysis we consider the following assumptions.

- (1) At the micro scale (Level II) the ionomer-phase is considered a homogeneous medium for the transport of water and proton-bearing complexes.
- (2) The TPB regions are envisioned as *surfaces* of discontinuity between the ionomer-phase and electrically conductive solid phase (C/Pt), rather than *lines* of discontinuity between ionomer, C/Pt and catalyst layer pores filled with electroactive species. Indeed, the diffusion coefficient of oxygen is sufficiently large, so that oxygen can diffuse efficiently through the ionomer towards the Pt sites up to ~ 200 nm [19]

(compared to ~ 1 nm interface thickness) and the reaction rate is not controlled by mass transport limitations in the Nafion coating. Furthermore, this interface is considered immaterial and therefore unable of accumulating mass and charge, namely, $\partial c_{\text{H}^+,is}/\partial t = 0$, $\partial c_{\text{H}_2\text{O},is}/\partial t = 0$.

- (3) Protons may enter and exit the ionomer-phase only when they cross the TPB regions (ionomer/electrically-conductive solid interfaces, labeled *is*) as they participate in electrochemical reactions. In order to satisfy ionomer-phase electroneutrality, protonated complexes do not leave the ionomer across the interfaces with the liquid water in the catalyst layer pores and thus are unable to migrate towards the Pt sites in the intra-agglomerate space. The liquid water layer ~ 1 -2 nm thick adjacent to the ionomer-phase and containing protonated complexes is assimilated to the hydrophilic domains and is considered to be integral part of the ionomer. Therefore, the proton flux across the ionomer-fluid interfaces, labeled *if*, is zero, $c_{\text{H}^+,i} \vec{v}_{\text{H}^+,i} \cdot \vec{n}_{if} = 0$.
- (4) The C/Pt agglomerates are fixed solid structures. Their interface with the ionomer is fixed once the ionomer has been hydrated and the velocity of this interface is zero, $\vec{w}_{is} = 0$. As a consequence, the ionomer-phase may swell or contract as a function of hydration only across the interfaces with the fluids in the catalyst layer pores (*if*-interfaces). Even if we relax this constraint, the velocity of the ionomer-solid interface \vec{w}_{is} is negligibly small compared to the proton mobility $\vec{v}_{\text{H}^+,i}$ or velocity of water molecules $\vec{v}_{\text{H}_2\text{O},i}$.

2. Microscopic Equations for Conservation of Charge and Water Transport in the Ionomer-Phase

The catalyst layer system under consideration is a porous mixture with a solid matrix consisting of an electrically conductive phase-*s* (carbon-supported Pt) and a proton-conductive phase-*i* (ionomer) available for protons and water transport. The primary and secondary pores of the C/Pt are filled with gaseous electroactive species and liquid water. For the derivation of the governing equations for the concentration of protons and water in ionomer we will be focusing on the transport phenomena in the ionomer and will not make distinction between the fluid phases-*f* in the primary and secondary pores of the carbon-supported Pt.

2.1. Microscopic Equation for Conservation of Charge in Ionomer-Phase. The microscopic equation which governs the proton transport in ionomer-phase (equation for conservation of charge) can be expressed as

$$\frac{\partial c_{\text{H}^+,i}}{\partial t} + \nabla \cdot (c_{\text{H}^+,i} \vec{v}_{\text{H}^+,i}) = 0 \quad (1)$$

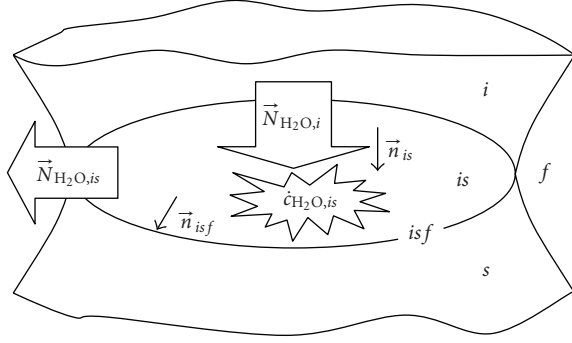


FIGURE 2: Water fluxes between the TPB regions (*is*-Interface), ionomer (*i*), and catalyst layer pores (*f*).

in which the second subscript *i* indicates that the variables are related to the ionomer phase. At the TPB regions (*is*-interface), the boundary condition associated with (1) is

$$\begin{aligned} \frac{\partial c_{H^+,is}}{\partial t} + \nabla_s \cdot (c_{H^+,is} \vec{v}_{H^+,is}) \\ = c_{H^+,i} (\vec{v}_{H^+,i} - \vec{w}_{is}) \cdot \vec{n}_{is} + \dot{c}_{H^+,is} \end{aligned} \quad (\text{B.C.1})$$

in which ∇_s represents the surface gradient operator along the *is*-interface and \vec{n}_{is} is the unit vector normal to the *is*-interface and pointing outwards from the ionomer-phase. The terms in the left-hand side (LHS) represent proton accumulation and proton transport in the TPB region. The terms in the right-hand side (RHS) represent the interfacial molar flux of protons between the bulk ionomer and the TPB region and the molar rate of proton production in HOR at anode or proton consumption in ORR at cathode. Considering the second and the fourth assumptions and considering the proton flux within the TPB region constant ($c_{H^+,is} \vec{v}_{H^+,is} = \text{const}$), the resulting boundary condition at the TPB regions reduces to the following expression:

$$c_{H^+,i} \vec{v}_{H^+,i} \cdot \vec{n}_{is} + \dot{c}_{H^+,is} = 0, \quad (\text{B.C.1a})$$

which states that the proton flux between the ionomer and the TPB region is balanced by the rate of proton production at anode during HOR or the rate proton consumption at cathode during ORR.

2.2. Microscopic Equation for Water Transport in Ionomer-Phase. The microscopic equation that governs the water transport in ionomer is

$$\frac{\partial c_{H_2O,i}}{\partial t} + \nabla \cdot (c_{H_2O,i} \vec{v}_{H_2O,i}) = 0. \quad (2)$$

The local velocity of water may be decomposed into an average hydrodynamic fluid velocity and a diffusion velocity

$$\vec{v}_{H_2O,i} = \vec{v}_{(H_2O/H^+),i} + \vec{u}_{H_2O,i}, \quad (3)$$

such that the total water flux $\vec{N}_{H_2O,i} = c_{H_2O,i} \vec{v}_{H_2O,i}$ is the sum of the electro-osmotic drag flux $\vec{N}_{H_2O,i}^{\text{drag}} = c_{H_2O,i} \vec{v}_{(H_2O/H^+),i}$ and the diffusion flux $\vec{N}_{H_2O,i}^{\text{diff}} = c_{H_2O,i} \vec{u}_{H_2O,i}$.

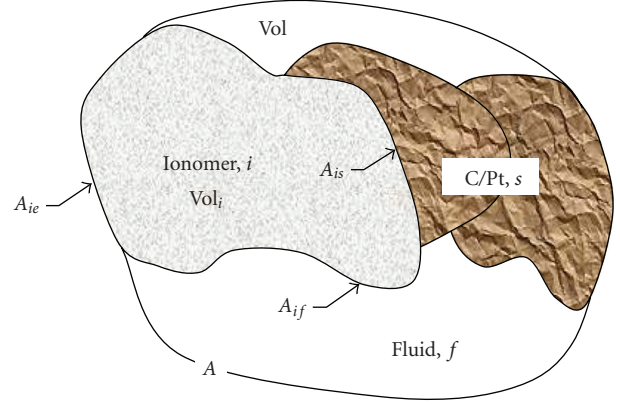


FIGURE 3: Averaging volume.

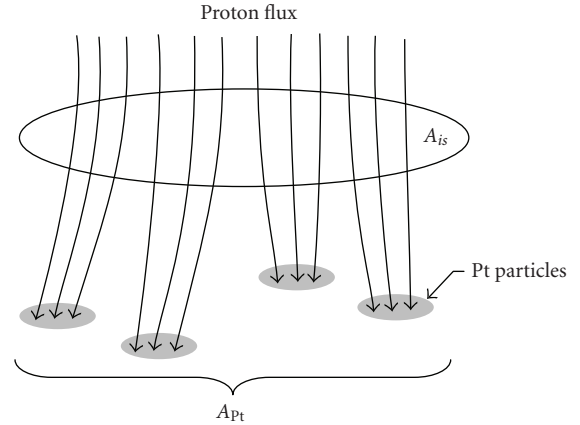


FIGURE 4: The proton flux across the ionomer/solid electrically conductive phase (C/Pt) interface A_{is} .

Considering that TPB regions do not accumulate mass and the velocity of the TPB regions is zero (second and fourth assumptions) and considering the water flux within the TPB region to be constant, the boundary condition associated to (2) at the TPB regions reduces to the following form:

$$c_{H_2O,is} \vec{v}_{H_2O,is} \cdot \vec{n}_{isf} = c_{H_2O,i} \vec{v}_{H_2O,i} \cdot \vec{n}_{is} + \dot{c}_{H_2O,is}, \quad (\text{B.C.2})$$

which states that the water entering the TPB region from the ionomer-phase and the water produced in the ORR exits the TPB region into the catalyst layer pores (Figure 2).

Unlike protons, water may be transferred by sorption or desorption across the *if*-interfaces between the ionomer and the catalyst layer pores. At these interfaces, the boundary condition associated to (2) is

$$c_{H_2O,i} (\vec{v}_{H_2O,i} - \vec{w}_{if}) \cdot \vec{n}_{if} = c_{H_2O,f} (\vec{v}_{H_2O,f} - \vec{w}_{if}) \cdot \vec{n}_{if}. \quad (\text{B.C.3})$$

3. Volume-Averaged Equations for Conservation of Charge and Water Transport in CCMs

The volume-averaged transport equations are obtained by application of the averaging theorems to the local, microscopic transport equations. An averaging control volume (Figure 3) has volume Vol fixed in space and time surrounded by an enveloping surface of area A . Its size $\sqrt[3]{\text{Vol}}$ must be larger than the length scale associated with Level II, which may be the diameter of the C/Pt agglomerates or diameter of the ionomer clusters, but smaller compared to the computational subdomain (length scale associated to Level I). The averaging control volume must include all catalyst layer ingredients, including ionomer-phase, electrically conductive C-Pt agglomerates with fluids in its primary and secondary pores and the TPB regions defined by their contiguity.

The ionomer-phase within the averaging control volume has volume Vol_i surrounded by the interfacial area A_i with the following constituents: ionomer-C/Pt interfacial area A_{is} , ionomer-fluid interfacial area A_{if} and the control volume entrances and exits crossing the ionomer A_{ie} (Figure 3). The volume fraction of ionomer within an averaging control volume is defined as $\varepsilon_i = \text{Vol}_i/\text{Vol}$. The volume Vol_i occupied by ionomer in an averaging control volume may change in time when the hydrated hydrophilic domains expand or contract as a function of hydration level. The ratio between area A_{ie} available for protons and water to enter or exit the control volume and the total enveloping surface area A , $\underline{\varepsilon}_A = A_{ie}/A$, is called directional surface permeability tensor. For a property ψ_i which can be a scalar or a tensor associated with the ionomer-phase are defined the local volume average ${}^3\langle\psi_i\rangle = 1/\text{Vol}\int_{\text{Vol}_i}\psi_i dV$, the intrinsic volume average ${}^{3i}\langle\psi_i\rangle = 1/\text{Vol}_i\int_{\text{Vol}_i}\psi_i dV$, and the intrinsic surface average ${}^{2i}\langle\psi_i\rangle = 1/A_{ie}\int_{A_{ie}}\psi_i \vec{n}_i dA$. The local volume and the intrinsic volume averages satisfy the relation

$${}^3\langle\psi_i\rangle = \varepsilon_i {}^{3i}\langle\psi_i\rangle. \quad (4)$$

The following averaging theorems that relate the averages of the space and time derivatives of property ψ_i to the space and time derivatives of the average of ψ_i have been proposed [13, 14]

$${}^3\langle\nabla\psi_i\rangle = \nabla{}^3\langle\psi_i\rangle + \frac{1}{\text{Vol}}\int_{A_{if}+A_{is}}\psi_i \vec{n}_i dA, \quad (5a)$$

$${}^3\langle\nabla\cdot\vec{\psi}_i\rangle = \nabla\cdot{}^3\langle\vec{\psi}_i\rangle + \frac{1}{\text{Vol}}\int_{A_{if}+A_{is}}\vec{\psi}_i\cdot\vec{n}_i dA, \quad (5b)$$

$${}^3\left\langle\frac{\partial\psi_i}{\partial t}\right\rangle = \frac{\partial{}^3\langle\psi_i\rangle}{\partial t} - \frac{1}{\text{Vol}}\int_{A_{if}+A_{is}}\psi_i \vec{w}_i \vec{n}_i dA \quad (5c)$$

in which \vec{n}_i is the unit outward vector normal to the interfaces surrounding the ionomer and \vec{w}_i is the velocity

vector of the ionomer-phase interfaces within the averaging volume. It can be shown (see, e.g., [17]) that

$$\nabla\cdot{}^3\langle\vec{\psi}_i\rangle = \nabla\cdot\left(\underline{\varepsilon}_A{}^{2i}\langle\vec{\psi}_i\rangle\right). \quad (6)$$

3.1. Volume-Averaged Equation for Conservation of Charge in CCMs. Application of the averaging theorems (5b) and (5c) to the microscopic transport equation (1) yields the volume-averaged equation for conservation of charge

$$\begin{aligned} \frac{\partial{}^3\langle c_{H^+,i}\rangle}{\partial t} + \nabla\cdot{}^3\langle c_{H^+,i}\vec{v}_{H^+,i}\rangle \\ + \frac{1}{\text{Vol}}\int_{A_{if}+A_{is}}c_{H^+,i}(\vec{v}_{H^+,i}-\vec{w}_i)\cdot\vec{n}_i dA = 0. \end{aligned} \quad (7)$$

We note first that $\partial/\partial t{}^3\langle c_{H^+,i}\rangle = 0$ since due to electroneutrality, the volume-averaged proton concentration is constant and equal to the concentration of the immobile negatively charged sulfonate groups $-\text{SO}_3^-$. The last term in (7), which emerges as a consequence of employing the averaging theorems, represents the interfacial flux of protons across the ionomer boundaries laying inside the averaging volume. According to the third assumption, the flux of protons across the *if*-interface is zero and the area of integration reduces to A_{is} . Since the protons crossing the *is*-interface converge towards the Pt sites (Figure 4), the area of integration A_{is} reduces further to the total catalyst area A_{Pt} in the averaging volume. According to the fourth assumption $\vec{w}_{is} = 0$ and the term reduces to $1/\text{Vol}\int_{A_{Pt}}c_{H^+,i}\vec{v}_{H^+,i}\cdot\vec{n}_i dA$. Considering relation (6), (7) becomes

$$\nabla\cdot\left(\underline{\varepsilon}_A{}^{2i}\langle c_{H^+,i}\vec{v}_{H^+,i}\rangle\right) + \frac{1}{\text{Vol}}\int_{A_{Pt}}c_{H^+,i}\vec{v}_{H^+,i}\cdot\vec{n}_i dA = 0 \quad (8)$$

in which ${}^{2i}\langle c_{H^+,i}\vec{v}_{H^+,i}\rangle = {}^{2i}\langle\vec{N}_{H^+,i}\rangle$ represents the *macroscopic* flux of protons along the CCM (macro scale) and $c_{H^+,i}\vec{v}_{H^+,i}\cdot\vec{n}_i = \vec{N}_{H^+,i}\cdot\vec{n}_i$ represents the *local* interfacial flux of protons crossing the TPB regions (nanometer scale) when protons engage in electrochemical reactions.

The volume-averaged equation for conservation of charge (8) states that:

“The change in proton flux across a control volume (averaging volume) is equal to the total interfacial flux of protons across the TPBs distributed in the control volume, when protons engage in electrochemical reactions”.

The total interfacial flux of protons across the TPBs within the averaging volume $1/\text{Vol}\int_{A_{Pt}}c_{H^+,i}\vec{v}_{H^+,i}\cdot\vec{n}_i dA$ is a subgrid-scale phenomenon. It represents a distributed source of protons at anode and a distributed sink of protons at cathode. In a membrane this term is zero since $A_{Pt} = 0$.

Considering the boundary condition (B.C.1a) we can write

$$\begin{aligned} \frac{1}{\text{Vol}}\int_{A_{Pt}}c_{H^+,i}\vec{v}_{H^+,i}\cdot\vec{n}_i dA &= -\frac{1}{\text{Vol}}\int_{A_{Pt}}\dot{c}_{H^+,is}dA \\ &= -\frac{A_{Pt}}{\text{Vol}}\text{Pt}\langle\dot{c}_{H^+,is}\rangle, \end{aligned} \quad (9)$$

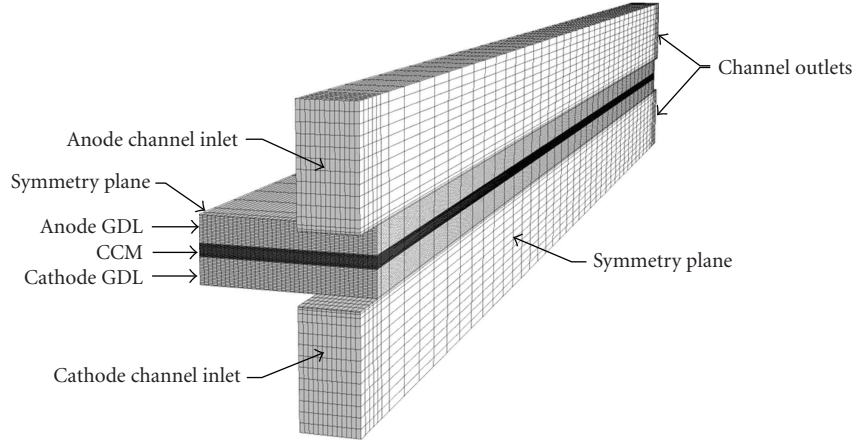
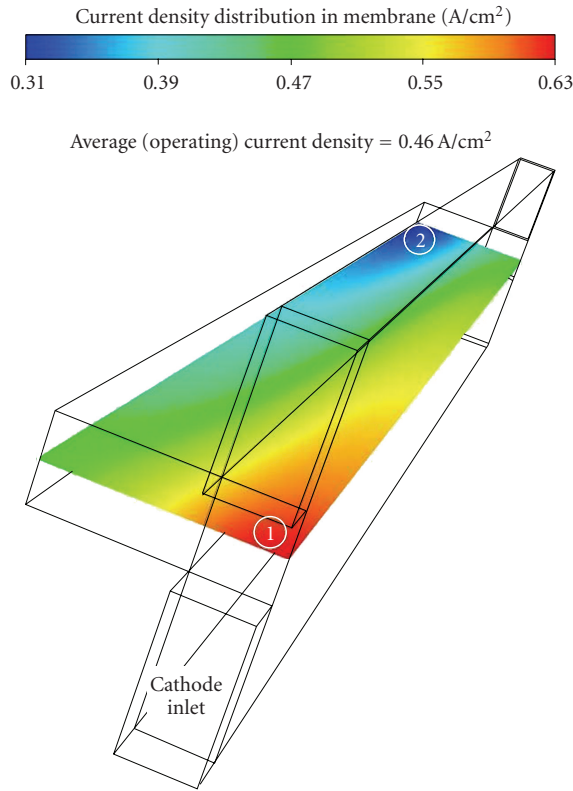


FIGURE 5: Computational domain and mesh.


 FIGURE 6: Current density distribution in the membrane for an operating current density of 0.46 A/cm^2 and cell voltage of 0.7 V .

where the operator $\text{Pt}\langle \cdot \rangle$ defines a surface average over the effective Pt surface area $\text{Pt}\langle \psi_{is} \rangle = 1/A_{\text{Pt}} \int_{A_{\text{Pt}}} \psi_{is} dA$ and A_{Pt}/Vol [m^2/m^3] represents the effective catalyst layer surface area (within the TPB regions) per unit geometric volume. $\text{Pt}\langle \dot{c}_{\text{H}^+,is} \rangle$ represents the averaged rate of proton production during HOR or proton consumption during ORR.

The volume-averaged equation for conservation of charge can now be written as

$$\nabla \cdot \left(\underline{\underline{\epsilon}}_A^{2i} \langle \vec{N}_{\text{H}^+,i} \rangle \right) = \frac{A_{\text{Pt}}}{\text{Vol}} \text{Pt} \langle \dot{c}_{\text{H}^+,is} \rangle, \quad (10)$$

which states that:

“The change in proton flux across a control volume (averaging volume) is equal to the volumetric rate of proton production during HOR or proton consumption during ORR”.

Multiplying(8) by the Faraday constant we obtain the equation for current density

$$\nabla \cdot \left(\underline{\underline{\epsilon}}_A^{2i} \langle \vec{i} \rangle \right) + \frac{1}{\text{Vol}} \int_{A_{\text{Pt}}} \vec{i} \cdot \vec{n}_{is} dA = 0 \quad (11)$$

in which $^{2i} \langle \vec{i} \rangle = ^{2i} \langle N_{\text{H}^+,i} \rangle \vec{i}_k F$ is the *macroscopic, longitudinal* current density representing the macroscopic flux of protons along the ionomer, throughout the anode catalyst layer, membrane and cathode catalyst layer and $\vec{i}_k = (\vec{i}_x, \vec{i}_y, \vec{i}_z)$ are the versors of the macroscopic coordinate system (Figure 1). The $\vec{i} = N_{\text{H}^+,i} \vec{n}_{is} F$ is the *local, transversal* current density generated by the protons that engage in electrochemical reactions. The local transversal component of the current density defines the charge transfer current $j = (1/\text{Vol}) \int_{A_{\text{Pt}}} \vec{N}_{\text{H}^+,i} \cdot \vec{n}_{is} F dA$ [A/cm^3] [1] and the equation for current density may be written as

$$\nabla \cdot \left(\underline{\underline{\epsilon}}_A^{2i} \langle \vec{i} \rangle \right) + j = 0. \quad (12)$$

3.2. Volume-Averaged Equation for Water Transport in the Ionomer-Phase of CCMs. Application of the averaging theorems (5b) and (5c) to the microscopic equation for water

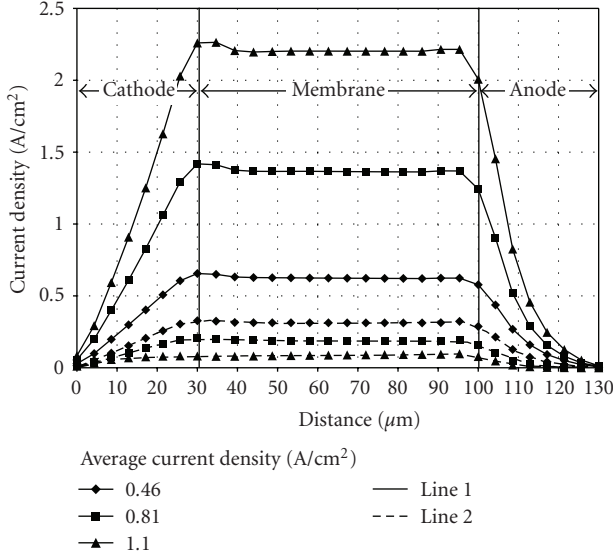


FIGURE 7: Current density profiles along two lines crossing the CCM and situated in the regions marked 1 and 2 in Figure 6; operating conditions: (i) 0.46 A/cm² and 0.7 V, (ii) 0.81 A/cm² and 0.6 V, (iii) 1.1 A/cm² and 0.5 V.

transport in ionomer (2) and using relations (4) and (6) yield the volume-averaged equation for water transport in CCM

$$\begin{aligned} & \frac{\partial(\varepsilon_i^{3i} \langle c_{\text{H}_2\text{O},i} \rangle)}{\partial t} + \nabla \cdot \left(\underline{\varepsilon}_A^{2i} \langle \vec{N}_{\text{H}_2\text{O},i}^{\text{drag}} \rangle \right) \\ & + \nabla \cdot \left(\underline{\varepsilon}_A^{2i} \langle \vec{N}_{\text{H}_2\text{O},i}^{\text{diff}} \rangle \right) \\ & + \frac{1}{\text{Vol}} \int_{A_{ij}+A_{is}} c_{\text{H}_2\text{O},i} (\vec{v}_{\text{H}_2\text{O},i} - \vec{w}_i) \cdot \vec{n}_i dA = 0 \end{aligned} \quad (13)$$

in which the total water flux was written as the sum between an electro-osmotic drag flux and a diffusion flux (Section 2.2).

The electro-osmotic drag coefficient is obtained experimentally [20] by measuring the current density (total proton flux) and the water flux throughout a PEM ($\underline{\varepsilon}_A = 1$) and is defined as

$$n_{\text{drag}} = \frac{N_{\text{H}_2\text{O},i}^{\text{drag}}}{N_{\text{H}^+,i}}. \quad (14)$$

Using (8), (11), and (14), the second term in (13) may be further written as

$$\begin{aligned} & \nabla \cdot \left(\underline{\varepsilon}_A n_{\text{drag}}^{2i} \langle \vec{N}_{\text{H}^+,i} \rangle \right) \\ & = n_{\text{drag}} \nabla \cdot \left(\underline{\varepsilon}_A^{2i} \langle \vec{N}_{\text{H}^+,i} \rangle \right) + \underline{\varepsilon}_A^{2i} \langle \vec{N}_{\text{H}^+,i} \rangle \cdot \nabla n_{\text{drag}} \quad (15) \\ & = n_{\text{drag}} \frac{\nabla \cdot \left(\underline{\varepsilon}_A^{2i} \langle \vec{i} \rangle \right)}{F} + \frac{\underline{\varepsilon}_A^{2i} \langle \vec{i} \rangle}{F} \cdot \nabla n_{\text{drag}}. \end{aligned}$$

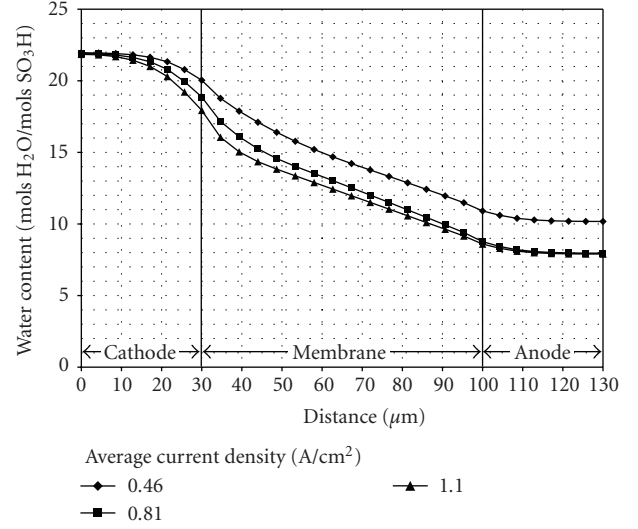


FIGURE 8: Water content profiles across the CCM (along line 1) for three operating regimes.

The term $n_{\text{drag}} \nabla \cdot (\underline{\varepsilon}_A^{2i} \langle \vec{i} \rangle) / F$ represents the volumetric rate at which water accumulates in the ionomer-phase of a control volume as a result of the difference between the incoming and outgoing proton fluxes. In cathode catalyst layers, the proton flux $\langle \vec{N}_{\text{H}^+,i} \rangle$ decreases in the direction of the current as protons are consumed in the ORR at a rate of $\nabla \cdot (\underline{\varepsilon}_A^{2i} \langle \vec{i} \rangle) / F$ (8). In this case, the water flux generated by electro-osmotic drag will decrease as well, the difference between the outgoing and incoming fluxes representing the water accumulated in the ionomer-phase of a control volume. In anode catalyst layers the proton flux increases in the direction of the current as protons are produced in the HOR and the water flux generated by electro-osmotic drag will increase as well. In this case, water in ionomer will be depleted.

The second term, $\nabla n_{\text{drag}} \cdot \underline{\varepsilon}_A^{2i} \langle \vec{i} \rangle / F$, represents the volumetric rate at which water accumulates locally in the ionomer-phase of a control volume when the hydrodynamic motion of the protons occurs along a water concentration gradient, or equivalently, along a gradient of hydrophilic domain sizes. This term is the macroscopic representation of the phenomenon called “stripping off” the water molecules in the peripheral solvation shells of the protonated complexes when the latter are transported from larger hydrophilic domains (higher water content) to smaller hydrophilic domains (lower water content) [1]. When the hydrodynamic motion of the protons is in the opposite direction, from smaller to larger hydrophilic domains (lower to higher water contents), it describes a local depletion of water. In this case, the protonated complexes engage more water molecules in the hydrodynamic motion as the number of molecules in their solvation shells increases.

The third term in (13) represents water transport by diffusion and is equal to $-\nabla \cdot (\underline{\varepsilon}_A D_{\text{H}_2\text{O},i} \nabla^{2i} \langle c_{\text{H}_2\text{O},i} \rangle)$.

The last term in (13) representing the fluxes of water across the interface with the fluids in the catalyst layer pores and across the TPB regions may be deconvolved as

$$\begin{aligned} & \frac{1}{\text{Vol}} \int_{A_{if}+A_{is}} c_{\text{H}_2\text{O},i} (\vec{v}_{\text{H}_2\text{O},i} - \vec{w}_i) \cdot \vec{n}_i dA \\ &= \frac{1}{\text{Vol}} \int_{A_{if}} c_{\text{H}_2\text{O},i} (\vec{u}_{\text{H}_2\text{O},i} - \vec{w}_{if}) \cdot \vec{n}_{if} dA \\ &+ \frac{1}{\text{Vol}} \int_{A_{is}} c_{\text{H}_2\text{O},i} \vec{v}_{\text{H}_2\text{O},i} \cdot \vec{n}_{is} dA \\ &+ \frac{1}{\text{Vol}} \int_{A_{Pt}} c_{\text{H}_2\text{O},i} \vec{v}_{(\text{H}_2\text{O}/\text{H}^+),i} \cdot \vec{n}_{is} dA. \end{aligned} \quad (16)$$

The first term in the RHS represents the water exchanged between ionomer and catalyst layer pores by sorption and desorption. The second term in the RHS represents the water exchanged between ionomer and TPB regions by diffusion at nonequilibrium and is equal to

$$-\frac{1}{\text{Vol}} \int_{A_{is}} D_{\text{H}_2\text{O}} \nabla \mu_{\text{H}_2\text{O}} \cdot \vec{n}_{is} dA. \quad (17)$$

The last term represents the volumetric rate at which water molecules in the solvation shells of the protonated complexes are dragged in or out of the ionomer when they cross the TPB as they participate in the HOR or ORR. This transfer mechanism was called ‘‘electro-osmotic discharge’’ (EOD) [1]. Using (14) and (11), this term is equal to

$$\begin{aligned} & \frac{1}{\text{Vol}} \int_{A_{Pt}} c_{\text{H}_2\text{O},i} \vec{v}_{(\text{H}_2\text{O}/\text{H}^+),i} \cdot \vec{n}_{is} dA \\ &= n_{\text{drag}} \frac{1}{\text{Vol}} \int_{A_{Pt}} c_{\text{H}^+,i} \vec{v}_{\text{H}^+,i} \cdot \vec{n}_{is} dA \\ &= -n_{\text{drag}} \frac{\nabla \cdot (\underline{\varepsilon}_A^{2i} \langle \vec{i} \rangle)}{F}, \end{aligned} \quad (18)$$

and therefore it cancels with the first term in the RHS of (15). Indeed, the water that would accumulate in the ionomer-phase of a control volume at cathode as a result of the difference between the incoming and outgoing electro-osmotic drag fluxes is removed from the ionomer by electro-osmotic discharge.

Inserting expressions (15)–(18) in (13) and considering the relation between molar concentration of water in ionomer and water content $c_{\text{H}_2\text{O},i} = \lambda \rho_{\text{dry}}/\text{EW}$, one obtains the conservation equation for water content in CCMs

$$\begin{aligned} & \frac{\rho_{\text{dry}}}{\text{EW}} \frac{(\partial \varepsilon_i^{3i} \langle \lambda \rangle)}{\partial t} + \frac{\underline{\varepsilon}_A^{2i} \langle \vec{i} \rangle}{F} \\ & \cdot \nabla n_{\text{drag}} - \frac{\rho_{\text{dry}}}{\text{EW}} \nabla \cdot (\underline{\varepsilon}_A D_{\text{H}_2\text{O},i} \nabla^{2i} \langle \lambda \rangle) \\ & + \frac{1}{\text{Vol}} \int_{A_{if}} c_{\text{H}_2\text{O},f} (\vec{v}_{\text{H}_2\text{O},f} - \vec{w}_{if}) \cdot \vec{n}_{if} dA \\ & - \frac{1}{\text{Vol}} \int_{A_{is}} D_{\text{H}_2\text{O}} \nabla \mu_{\text{H}_2\text{O}} \cdot \vec{n}_{is} dA = 0. \end{aligned} \quad (19)$$

The integral terms in (19) which are subgrid-scale phenomena represent distributed sources or sinks for water in ionomer that are zero in a PEM. If water does not accumulate in the TPB regions, it will be at equilibrium with the adjacent water in ionomer and the last term in (19) is zero. The volume-averaged equation for water transport in the ionomer-phase of CCMs may be finally written as

$$\begin{aligned} & \underbrace{\frac{\rho_{\text{dry}}}{\text{EW}} \frac{\partial (\varepsilon_i \lambda)}{\partial t}}_{\text{bulk accumulation}} + \underbrace{\frac{\underline{\varepsilon}_A}{F} \nabla n_{\text{drag}} \cdot \vec{i}}_{\text{‘‘stripping off’’ water from peripheral solvation shells}} \\ & - \frac{\rho_{\text{dry}}}{\text{EW}} \nabla \cdot \left(\underline{\varepsilon}_A D_{\text{H}_2\text{O},i} \nabla \lambda \right) + \underbrace{S_{\lambda \text{ sorption/desorption}}}_{\text{water exchanged by sorption/desorption}} = 0, \end{aligned} \quad (20)$$

where for the sake of simple notations the averaging symbols were dropped. $S_{\lambda \text{ sorption/desorption}}$ represents the volumetric rate of water exchanged between ionomer and catalyst layer pores by sorption and desorption and must be determined experimentally. Note that even though the EOD term $\nabla \cdot (\underline{\varepsilon}_A \vec{i})/F$ does not appear explicitly in the transport equation (20), it does represent an effective mechanism of water transfer between ionomer and catalyst layer pores during fuel cell operation. Indeed, boundary condition (B.C.2) indicates that EOD water and ORR water exit the TPB regions into the catalyst layer pores (see Figure 2). EOD and ORR water represent distributed sources for the water in catalyst layer pores and must appear explicitly in its transport equation. This transfer mechanism may be accessed experimentally using an electrochemical cell with Pd-H electrodes [21]. Zawodzinski et al. [21] performed electro-osmotic drag measurements across membranes exposed on both sides to deionized water and compressed between two Pd-H electrodes. Current was passed between the electrodes, thus passing protons through the membrane from anode to cathode. The amount of water dragged across the membrane with the protons was determined by measuring the change in height of water capillary columns. Since the membrane was equilibrated at both sides with liquid water, it results that the mechanism responsible for passing water between the ionomer and the chambers filled with liquid water was not sorption/desorption, but EOD.

In PEMs, $\varepsilon_i = \underline{\varepsilon}_A = 1$, $S_{\lambda \text{ sorption/desorption}} = 0$ and the volume-averaged equation for water transport becomes

$$\frac{\rho_{\text{dry}}}{\text{EW}} \frac{\partial \lambda}{\partial t} + \nabla n_{\text{drag}} \cdot \frac{\vec{i}}{F} - \frac{\rho_{\text{dry}}}{\text{EW}} \nabla \cdot (D_{\text{H}_2\text{O},i} \nabla \lambda) = 0. \quad (21)$$

In this case, the term standing for EOD is zero, since in PEMs $\nabla \cdot \vec{i} = 0$.

4. Calculations

Equations (12) and (20) for current density and water content in CCM were solved along with the volume

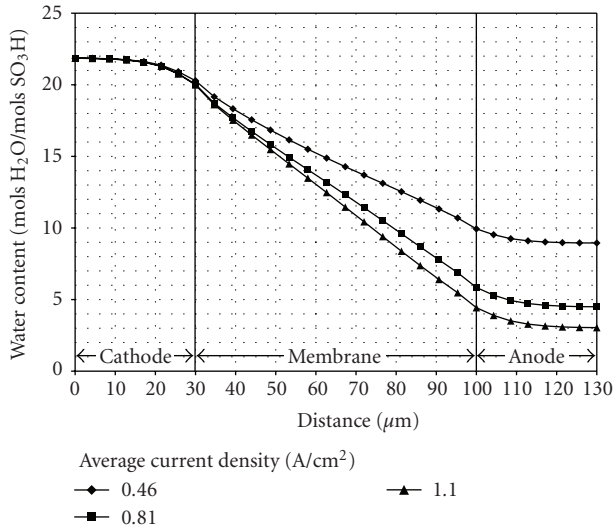


FIGURE 9: Water content profiles across the CCM (along line 2) for three operating regimes.

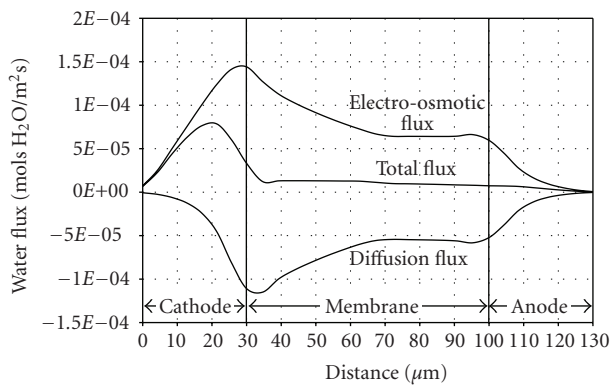


FIGURE 10: Water flux profiles across the CCM (along line 1) for an operating current of 0.64 A/cm^2 .

averaged-equations for the conservation of mass, species, and momentum in the PEMFC components using ANSYS-CFX 4.4 software. The 3-dimensional computational domain consisting of an anode channel, anode gas diffusion layer (GDL), CCM, cathode GDL, and cathode channel is illustrated in Figure 5. It extends from the channel inlets to channel outlets and from the symmetry plane along the channels to the symmetry plane between two adjacent channels.

The transport equations of the isothermal, single-phase model are presented in Appendix A, where for the sake of simple notations the averaging symbols were dropped. The reader may turn to [1] for a detailed presentation of the transport equations and their constitutive relations. The model considers that hydrogen and air enter the channels fully saturated. In the anode flow field, hydrogen is consumed in the HOR (A.17) and (C.27) and water is exchanged between the catalyst layer pores and ionomer by EOD (water leaves the pores) and by sorption/desorption at nonequilibrium equation (A.18), (C.28), and (C.30). In the cathode flow field, oxygen is consumed in the ORR

(A.15) and (C.26) and water is produced in the ORR and is exchanged between the catalyst layer pores and ionomer by EOD (water enters the pores) and by sorption/desorption at nonequilibrium equations (A.16), (C.25), (C.28), and (C.29).

Figure 6 illustrates the current density distribution in the membrane for the case of an operating (average) current density of 0.46 A/cm^2 and a cell voltage of 0.7 V . As hydrogen and oxygen are consumed, their concentrations decrease along the channels. Since the rates of HOR and ORR depend on their concentrations (C.33) and (C.34), the current density distribution follows the distributions of hydrogen and oxygen, being higher above the channel inlets and lower above the land in the vicinity of the outlets.

In Figure 7 are shown the current density profiles along two lines crossing the CCM situated in the regions marked 1 and 2 in Figure 6. Current density increases at anode (protons are produced in the HOR), is constant in the membrane, and decreases at cathode (protons are consumed in the ORR). The current density increases in region 1, and decreases in region 2 when the operating current increases. This is due to a decreasing oxygen and hydrogen concentrations in region 2 when the operating current increases. The slight increase in current density at the cathode-membrane interface indicates the increase in proton flux as the ionomer fraction reduces from 100% in membrane to 30% in catalyst layer.

Figures 8 and 9 show the water content profiles across the CCM, along the lines marked 1 and 2 in Figure 6. In catalyst layers, the water in the ionomer-phase equilibrates with the water vapor at its local activity a and/or the liquid water present in the catalyst layer pores according to isopiestic curves such as the one for Nafion 117 equation (C.44) [21]. Supersaturated conditions are encountered at cathode and the ionomer-phase is surrounded by a liquid water film. At cathode, the water content in the ionomer-phase is therefore constant at any operating regime ($\lambda = 22$). At anode, the vapor concentration (activity) decreases with increasing operating current. This determines the water in the ionomer-phase of the anode catalyst layer to equilibrate at lower values when the operating current increases. Inside the membrane, water is depleted when the current density flows along a positive gradient of water content (from smaller to larger hydrophilic domains) according to $\vec{i} \cdot \nabla n_{\text{drag}}/F$. In this case, the protonated complexes engage more water molecules in hydrodynamic motion as the number of water molecules in their solvation shells increases. The electro-osmotic drag coefficient equation (C.48) was measured by the Los Alamos National Laboratories group [22, 23] for membranes immersed in liquid water ($n_{\text{drag}} = 2.5$) and for membranes at equilibrium with water vapor over a wide range of activities ($n_{\text{drag}} = 1$). Water inside the ionomer-phase will be therefore depleted only when the water content is higher than 14. Above this value, the water content will depart from a linear profile (see the membrane area towards the cathode catalyst layer in Figure 8). This feature is less evident when the local current density is lower (Figure 9). Note that in our computations, we allowed the

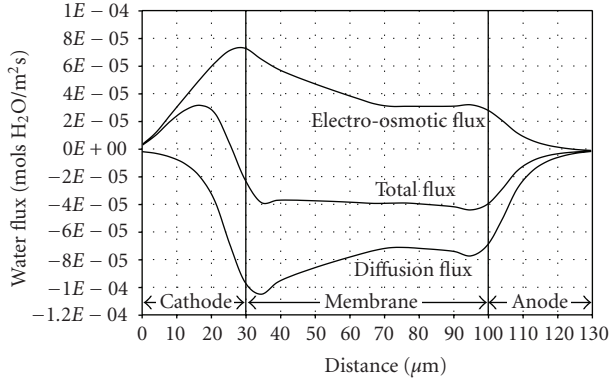


FIGURE 11: Water flux profiles across the CCM (along line 2) for an operating current of 0.64 A/cm^2 .

electro-osmotic drag coefficient to increase linearly when λ increases from 14 to 22.

Figures 10 and 11 depict the water flux profiles in the ionomer-phase across the CCM along lines 1 and 2. The electro-osmotic drag flux $\vec{i} n_{\text{drag}}/F$ increases at anode following the increase in current density, is constant in membrane where the water content is below 14 (areas towards the anode catalyst layer), increases in membrane areas towards the cathode catalyst layer (electro-osmotic drag coefficient increases), and decreases with the current at cathode. The back-diffusion flux $-D_{\text{H}_2\text{O},i} \nabla \lambda$ is highest in the membrane areas towards the cathode catalyst layer, where it acts to bring back the water carried away by the protonated complexes in electro-osmotic drag. Note that the latter mechanism displaces water from areas with lower water content towards areas with higher water content. The back-diffusion flux is constant in the membrane areas close to the anode catalyst layer where the water content gradient is constant. In region 2 (Figure 10), the electro-osmotic flux is lower than in region 1 (Figure 9) as the current density is lower (see Figures 6 and 7), but the back-diffusion flux is similar in both regions. The resulting total water flux is positive in region 1 and negative in region 2. As a consequence, water is transported from anode to cathode across the CCM in region 1 and is transported in the opposite direction in region 2.

Figure 12 illustrates the water vapor distribution in the anode catalyst layer at the interface with membrane. Water mass fraction decreases downstream as water is transported from anode to cathode, but increases towards the channel outlets (region 2), where water is transported across the CCM in the opposite direction.

5. Conclusions

We derive a continuum model for water transport in the ionomer-phase of CCMs for PEMFCs using the method of volume averaging. Water accumulates in the ionomer-phase of CCMs as a result of

- (i) “stripping off” the water molecules in the peripheral solvation shells of the protonated complexes

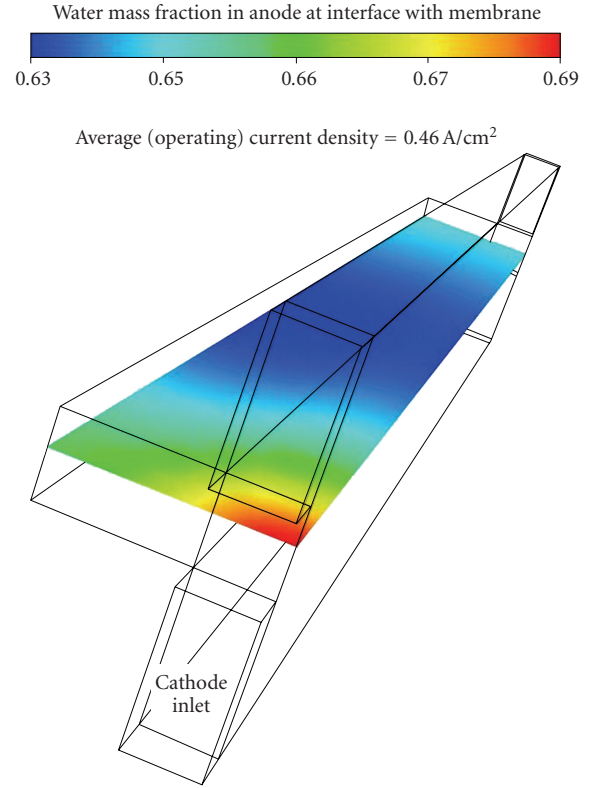


FIGURE 12: Water vapor distribution in the anode catalyst layer at the interface with membrane an operating current of 0.64 A/cm^2 .

when the hydrodynamic motion of the latter occurs along a gradient of water content (along a gradient of hydrophilic domain sizes), and expressed by $\underline{\varepsilon}_A \nabla n_{\text{drag}} \cdot \vec{i}/F$,

- (ii) the difference between the incoming and outgoing water diffusive fluxes, expressed by $-(\rho_{\text{dry}}/EW) \nabla \cdot (\underline{\varepsilon}_A D_{\text{H}_2\text{O},i} \nabla \lambda)$,
- (iii) exchanges by sorption and desorption between the ionomer-phase distributed in catalyst layers and the catalyst layer pores, $S_{\text{sorption/desorption}}$.

A second mechanism of water transfer between the ionomer-phase and the TPB regions distributed in the catalyst layers, referred to as electro-osmotic discharge and expressed by $n_{\text{drag}} \nabla \cdot (\underline{\varepsilon}_A \vec{i})/F$, does not affect the water accumulation in the ionomer-phase but affects the water accumulation in the catalyst pores. This term does not appear explicitly in the equation for water transport in the ionomer-phase, (20) and (21), but appears as source/sink terms in the transport equations for water in the catalyst layer pores.

To our best knowledge, the previous models for water transport in CCMs have been exclusively derived for use in CFD analysis intuitively, or by performing a balance of water fluxes across a control volume consisting of 100% ionomer-phase. These equations are therefore valid solely in PEMs and cannot capture correctly the mechanisms of water transfer between the ionomer-phase and the catalyst pores or the

mechanisms that affect water accumulation in the ionomer-phase. Appendix Group

Appendices

A. Transport Equations in the Flow Field

A.1. *Mass.* In both channels,

$$\frac{\partial \rho}{\partial t} + \nabla \cdot (\rho \vec{U}) = 0. \quad (\text{A.1})$$

In GDLs,

$$\frac{\partial}{\partial t} (\varepsilon_V \rho) + \nabla \cdot (\varepsilon \rho \vec{U}) = 0. \quad (\text{A.2})$$

In cathode catalyst layer,

$$\begin{aligned} \frac{\partial}{\partial t} (\varepsilon_V \rho) + \nabla \cdot (\varepsilon \rho \vec{U}) &= \varepsilon_V \left[H(Y_{\text{H}_2\text{O}}^{\text{sat}} - Y_{\text{H}_2\text{O}}) \dot{m}_{\text{H}_2\text{O}} + \dot{m}_{\text{O}_2} \right] \\ &+ \varepsilon_V \left[-\dot{m}_{\text{sorption}} + H(Y_{\text{H}_2\text{O}}^{\text{sat}} - Y_{\text{H}_2\text{O}}) (\dot{m}_{\text{desorption}} + \dot{m}_{\text{EOD},c}) \right]. \end{aligned} \quad (\text{A.3})$$

In anode catalyst layer,

$$\begin{aligned} \frac{\partial}{\partial t} (\varepsilon_V \rho) + \nabla \cdot (\varepsilon \rho \vec{U}) \\ &= \varepsilon_V \left[\dot{m}_{\text{H}_2} - \dot{m}_{\text{sorption}} - \dot{m}_{\text{EOD},a} \right. \\ &\quad \left. + H(Y_{\text{H}_2\text{O}}^{\text{sat}} - Y_{\text{H}_2\text{O}}) \dot{m}_{\text{desorption}} \right]. \end{aligned} \quad (\text{A.4})$$

A.2. *Momentum.* In both channels,

$$\begin{aligned} \frac{\partial}{\partial t} (\rho \vec{U}) + \nabla \cdot (\rho \vec{U} \vec{U}) - \nabla \cdot \left\{ \mu \left[\nabla \vec{U} + (\nabla \vec{U})^T \right] \right\} \\ &= -\nabla p. \end{aligned} \quad (\text{A.5})$$

In both GDLs,

$$\frac{\partial}{\partial t} (\varepsilon_V \rho \vec{U}) = -\varepsilon_V \nabla p + \varepsilon_V \frac{\mu}{K_V} \vec{U}. \quad (\text{A.6})$$

In cathode catalyst layer,

$$\frac{\partial}{\partial t} (\varepsilon_V \rho \vec{U}) = -\varepsilon_V \nabla p + \varepsilon_V \frac{\mu}{K_V} \vec{U} + \varepsilon_V (\dot{m}_{\text{O}_2} - \dot{m}_{\text{sorption}}) \vec{U}. \quad (\text{A.7})$$

In anode catalyst layer,

$$\begin{aligned} \frac{\partial (\varepsilon_V \rho \vec{U})}{\partial t} \\ &= -\varepsilon_V \nabla p + \varepsilon_V \frac{\mu}{K_V} \vec{U} + \varepsilon_V (\dot{m}_{\text{H}_2} - \dot{m}_{\text{sorption}} - \dot{m}_{\text{EOD},a}) \vec{U}. \end{aligned} \quad (\text{A.8})$$

A.3. *Species.* In cathode channel,

$$\frac{\partial (\rho Y_{\text{O}_2})}{\partial t} + \nabla \cdot (\rho \vec{U} Y_{\text{O}_2}) - \nabla \cdot (\rho D_{\text{O}_2} \nabla Y_{\text{O}_2}) = 0. \quad (\text{A.9})$$

In both channels,

$$\frac{\partial (\rho Y_{\text{H}_2\text{O}})}{\partial t} + \nabla \cdot (\rho \vec{U} Y_{\text{H}_2\text{O}}) - \nabla \cdot (\rho D_{\text{H}_2\text{O}} \nabla Y_{\text{H}_2\text{O}}) = 0. \quad (\text{A.10})$$

In anode channel,

$$\frac{\partial (\rho Y_{\text{H}_2})}{\partial t} + \nabla \cdot (\rho \vec{U} Y_{\text{H}_2}) - \nabla \cdot (\rho D_{\text{H}_2} \nabla Y_{\text{H}_2}) = 0. \quad (\text{A.11})$$

In cathode GDL,

$$\frac{\partial (\varepsilon_V \rho Y_{\text{O}_2})}{\partial t} + \nabla \cdot (\varepsilon \rho \vec{U} Y_{\text{O}_2}) - \nabla \cdot (\varepsilon \rho D_{\text{O}_2} \nabla Y_{\text{O}_2}) = 0. \quad (\text{A.12})$$

In both GDLs,

$$\frac{\partial (\varepsilon_V \rho Y_{\text{H}_2\text{O}})}{\partial t} + \nabla \cdot (\varepsilon \rho \vec{U} Y_{\text{H}_2\text{O}}) - \nabla \cdot (\varepsilon \rho D_{\text{H}_2\text{O}} \nabla Y_{\text{H}_2\text{O}}) = 0. \quad (\text{A.13})$$

In anode GDL,

$$\frac{\partial (\varepsilon_V \rho Y_{\text{H}_2})}{\partial t} + \nabla \cdot (\varepsilon \rho \vec{U} Y_{\text{H}_2}) - \nabla \cdot (\varepsilon \rho D_{\text{H}_2} \nabla Y_{\text{H}_2}) = 0. \quad (\text{A.14})$$

In cathode catalyst layer,

$$\frac{\partial (\varepsilon_V \rho Y_{\text{O}_2})}{\partial t} + \nabla \cdot (\varepsilon \rho \vec{U} Y_{\text{O}_2}) - \nabla \cdot (\varepsilon \rho D_{\text{O}_2} \nabla Y_{\text{O}_2}) = \varepsilon_V \dot{m}_{\text{O}_2}. \quad (\text{A.15})$$

In cathode catalyst layer,

$$\begin{aligned} \frac{\partial (\varepsilon_V \rho Y_{\text{H}_2\text{O}})}{\partial t} + \nabla \cdot (\varepsilon \rho \vec{U} Y_{\text{H}_2\text{O}}) - \nabla \cdot (\varepsilon \rho D_{\text{H}_2\text{O}} \nabla Y_{\text{H}_2\text{O}}) \\ &= \varepsilon_V \left[H(Y_{\text{H}_2\text{O}}^{\text{sat}} - Y_{\text{H}_2\text{O}}) \dot{m}_{\text{H}_2\text{O}} \right] \\ &+ \varepsilon_V \left[-\dot{m}_{\text{sorption}} + H(Y_{\text{H}_2\text{O}}^{\text{sat}} - Y_{\text{H}_2\text{O}}) \right. \\ &\quad \left. \times (\dot{m}_{\text{desorption}} + \dot{m}_{\text{EOD},c}) \right]. \end{aligned} \quad (\text{A.16})$$

In anode catalyst layer,

$$\frac{\partial (\varepsilon_V \rho Y_{\text{H}_2})}{\partial t} + \nabla \cdot (\varepsilon \rho \vec{U} Y_{\text{H}_2}) - \nabla \cdot (\varepsilon \rho D_{\text{H}_2} \nabla Y_{\text{H}_2}) = \varepsilon_V \dot{m}_{\text{H}_2}. \quad (\text{A.17})$$

In anode catalyst layer,

$$\begin{aligned} \frac{\partial (\varepsilon_V \rho Y_{\text{H}_2\text{O}})}{\partial t} + \nabla \cdot (\varepsilon \rho \vec{U} Y_{\text{H}_2\text{O}}) - \nabla \cdot (\varepsilon \rho D_{\text{H}_2\text{O}} \nabla Y_{\text{H}_2\text{O}}) \\ &= \varepsilon_V \left[-(\dot{m}_{\text{sorption}} + \dot{m}_{\text{EOD},a}) \right. \\ &\quad \left. + H(Y_{\text{H}_2\text{O}}^{\text{sat}} - Y_{\text{H}_2\text{O}}) \dot{m}_{\text{desorption}} \right]. \end{aligned} \quad (\text{A.18})$$

where the Heaviside step function is defined as,

$$H(x) = \begin{cases} 1 & \text{if } x \geq 0, \\ 0 & \text{if } x < 0. \end{cases} \quad (\text{A.19})$$

B. Transport Equations in the CCM

B.1. Charge. In cathode catalyst layer,

$$\nabla \cdot (\varepsilon_A \sigma \nabla \Phi_i) + j_c = 0, \quad (\text{B.20})$$

see also (12)

In membrane,

$$\nabla \cdot (\sigma \nabla \Phi_i) = 0. \quad (\text{B.21})$$

In anode catalyst layer,

$$\nabla \cdot (\varepsilon_A \sigma \nabla \Phi_i) + j_a = 0. \quad (\text{B.22})$$

B.2. Water Content. In both catalyst layers,

$$\begin{aligned} \frac{\rho_{\text{dry}}}{EW} \frac{\partial(\varepsilon_i \lambda)}{\partial t} + \varepsilon_A \frac{\vec{i}}{F} \cdot \nabla n_{\text{drag}} \\ - \frac{\rho_{\text{dry}}}{EW} \nabla \cdot (\varepsilon_A D_{\text{H}_2\text{O},i} \nabla \lambda) + S_{\text{adsorption/desorption}} = 0 \end{aligned} \quad (\text{B.23})$$

see also (20)

In membrane,

$$\frac{\rho_{\text{dry}}}{EW} \frac{\partial \lambda}{\partial t} + \frac{\vec{i}}{F} \cdot \nabla n_{\text{drag}} - \frac{\rho_{\text{dry}}}{EW} \nabla \cdot (D_{\text{H}_2\text{O},i} \nabla \lambda) = 0, \quad (\text{B.24})$$

see also (21)

C. Constitutive Relations

Expression

$$\dot{m}_{\text{H}_2\text{O}} = \omega_c \nu_{\text{H}_2\text{O}} W_{\text{H}_2\text{O}}, \quad (\text{C.25})$$

$$\dot{m}_{\text{O}_2} = -\omega_c \nu_{\text{O}_2} W_{\text{O}_2}, \quad (\text{C.26})$$

$$\dot{m}_{\text{H}_2} = -\omega_a \nu_{\text{H}_2} W_{\text{H}_2}, \quad (\text{C.27})$$

$$m_{\text{sorption/desorption}} = C_\lambda (\lambda - \lambda_{\text{equilibrium}}) \left(\frac{\rho_{\text{dry}}}{EW} \right) W_{\text{H}_2\text{O}} \quad (\text{C.28})$$

(see [4]),

$$\dot{m}_{\text{EOD},c} = n_{\text{drag}} \left(\frac{j_c}{F} \right) W_{\text{H}_2\text{O}} \quad (\text{C.29})$$

(see [4])

$$\dot{m}_{\text{EOD},a} = n_{\text{drag}} \left(\frac{j_a}{F} \right) W_{\text{H}_2\text{O}} \quad (\text{C.30})$$

(see [4]),

$$D_i = \frac{(1 - Y_i)}{\sum_{i \neq j} (W_g W_j) (Y_j / D_{ij})} \quad \begin{array}{l} i = \text{O}_2, \text{H}_2\text{O}, \text{N}_2 \text{ at cathode,} \\ i = \text{H}_2, \text{H}_2\text{O at anode} \end{array} \quad (\text{C.31})$$

(see [24]),

$$\begin{aligned} p D_{ij} = a_1 \left(\frac{T}{\sqrt{T_{\text{cr},i} T_{\text{cr},j}}} \right)^{b_1} (p_{\text{cr},i} p_{\text{cr},j})^{1/3} (T_{\text{cr},i} T_{\text{cr},j})^{5/12} \\ \times \sqrt{\frac{1}{W_i} + \frac{1}{W_j}} \cdot 10^{-4}, \end{aligned} \quad (\text{C.32})$$

(see [25])

$$\omega_c = \frac{(a_{i_0}^{\text{ref}})_c}{\nu_{\text{H}^+} F} \cdot \frac{Y_{\text{O}_2}}{Y_{\text{O}_2}^{\text{ref}}} \left[\exp\left(\frac{\eta_c}{b_c}\right) - \exp\left(-\frac{\eta_c}{b_c}\right) \right], \quad (\text{C.33})$$

$$\omega_a = \frac{(a_{i_0}^{\text{ref}})_a}{\nu_{\text{H}^+} F} \cdot \sqrt{\frac{Y_{\text{H}_2}}{Y_{\text{H}_2}^{\text{ref}}}} \left[\exp\left(\frac{\eta_a}{b_a}\right) - \exp\left(-\frac{\eta_a}{b_a}\right) \right], \quad (\text{C.34})$$

$$\eta_c = \Phi_s - \Phi_i - U_0, \quad (\text{C.35})$$

$$\eta_a = \Phi_s - \Phi_i, \quad (\text{C.36})$$

$$j_c = \omega_c F \nu_{\text{H}^+}, \quad (\text{C.37})$$

$$j_a = \omega_a F \nu_{\text{H}^+}, \quad (\text{C.38})$$

$$\vec{i} = -\varepsilon_A \sigma \nabla \Phi_i \quad (\text{C.39})$$

$$\sigma = (0.5139\lambda - 0.326) \exp \left[1268 \left(\frac{1}{303} - \frac{1}{T} \right) \right] \quad (\text{C.40})$$

(see [22]),

$$D_{\text{H}_2\text{O},i} = \left(\frac{\partial \ln a}{\partial \ln c} \right) D_\lambda^{\text{self-diffusion}}, \quad (\text{C.41})$$

$$\begin{aligned} D_{\text{H}_2\text{O},i}^{\text{self-diffusion}} = 10^{-10} \exp \left[2416 \left(\frac{1}{303} - \frac{1}{T} \right) \right] \\ \times (2.563 - 0.33\lambda + 0.0264\lambda^2 - 0.000671\lambda^3) \end{aligned} \quad (\text{C.42})$$

(see [26]),

$$S_{\lambda \text{ sorption/desorption}} = C_\lambda (\lambda - \lambda_{\text{equilibrium}}) \left(\frac{\rho_{\text{dry}}}{EW} \right) \quad (\text{C.43})$$

(see [4]),

$$\lambda_{\text{equilibrium}} = \begin{cases} 0.043 + 17.18a - 39.85a^2 + 36.0a^3, & a \in [0, 1] (\text{vapor}), \\ 22, & a = 1 (\text{liquid}), \end{cases} \quad (\text{C.44})$$

(see [21]),

$$a = \frac{WpY_{\text{H}_2\text{O}}}{W_{\text{H}_2\text{O}}p_{\text{H}_2\text{O}}^{\text{sat}}}, \quad (\text{C.45})$$

$$W = \frac{\sum_i Y_i}{W_i} \quad \begin{array}{l} i = \text{O}_2, \text{H}_2\text{O}, \text{N}_2 \text{ at cathode,} \\ i = \text{H}_2, \text{H}_2\text{O} \text{ at anode,} \end{array} \quad (\text{C.46})$$

$$\begin{aligned} \ln p_{\text{H}_2\text{O}}^{\text{sat}} &= -\frac{5800.2206}{T} + 1.3914993 - 0.048640239T \\ &+ 0.41764768 \times 10^{-4}T^2 - 0.14452093 \\ &\times 10^{-7}T^3 + 6.5459673 \ln T \end{aligned} \quad (\text{C.47})$$

$$n_{\text{drag}} = \begin{cases} 1 & \text{if } 2 \leq \lambda \leq 14, \\ 2.5 & \text{if } \lambda = 22. \end{cases} \quad (\text{C.48})$$

(see [22, 23]),

Nomenclature

$\langle \rangle$:	Volume average operator
$\langle \rangle^i$:	Intrinsic volume average operator
$\langle \rangle^s$:	Intrinsic surface average operator
A :	Interfacial area [cm^2]
a :	Effective catalyst surface area per unit volume, [cm^2/cm^3] (C.33), (C.34)
a :	Water activity (C.44), (C.45)
a_1 :	Constant in Slattery-Bird correlation (C.32)
b_1 :	Exponent in Slattery-Bird correlation (C.32)
$c_{\text{H}_2\text{O}}$:	Molar concentration of water in ionomer [$\text{mols H}_2\text{O}/\text{cm}^3$]
c_{H^+} :	Molar concentration of protons [$\text{mols H}^+/\text{cm}^3$]
\dot{c}_{H^+} :	Molar rate of proton production or consumption [$\text{mols H}^+/\text{cm}^2\text{s}$]
$\dot{c}_{\text{H}_2\text{O}}$:	Molar rate of water production in ORR [$\text{mols H}_2\text{O}/\text{cm}^2\text{s}$]
C_λ :	Rate of water sorption in ionomer, [s^{-1}] (C.43)
$D_{\text{H}_2\text{O}}$:	Diffusion coefficient of water in ionomer [cm^2/s]
EW:	Equivalent weight [$\text{mols SO}_3^-/\text{g}$]
F :	Faraday constant 96487 [$\text{C}/\text{mols H}^+$]
$H(x)$:	Heaviside step function
i_0^{ref} :	Reference exchange current density, [a/m^3]
\vec{i} :	Current density [A/cm^2]
$\vec{i}_x, \vec{i}_y, \vec{i}_z$:	Versors of the macroscopic coordinate system
j :	Charge transfer current [A/cm^3]
K_V :	Absolute viscous permeability, [cm^2]

\dot{m} :	Mass source, [$\text{g}/\text{cm}^3\text{s}$]
n_{drag} :	Electro-osmotic drag coefficient [$\text{mols H}_2\text{O}/\text{mols H}^+$]
\vec{n}_i :	Unit vector normal to the i -phase interfaces and pointing outwards from i
\vec{n}_{is} :	Unit vector normal to the is -interface and pointing from i to s
\vec{n}_{isf} :	Unit vector in the is surface normal to the isf -interface with f -phase and pointing outwards from is
n_e :	Number of electrons participating in electrochemical reaction
\vec{N}_{H^+} :	Total proton flux [$\text{mols H}^+/\text{cm}^2\text{s}$]
$\vec{N}_{\text{H}^+}^{\text{structdiff}}$:	Proton flux caused by structure diffusion [$\text{mols H}^+/\text{cm}^2\text{s}$]
$\vec{N}_{\text{H}^+}^{\text{vehmech}}$:	Proton flux caused by the vehicle mechanism [$\text{mols H}^+/\text{cm}^2\text{s}$]
$\vec{N}_{\text{H}_2\text{O}}$:	Total water flux in ionomer [$\text{mols H}_2\text{O}/\text{cm}^2\text{s}$]
$\vec{N}_{\text{H}_2\text{O}}^{\text{drag}}$:	Water flux in ionomer generated by electro-osmotic drag [$\text{mols H}_2\text{O}/\text{cm}^2\text{s}$]
$\vec{N}_{\text{H}_2\text{O}}^{\text{diff}}$:	Diffusion water flux in ionomer [$\text{mols H}_2\text{O}/\text{cm}^2\text{s}$]
p :	Pressure, [Pa]
S_λ :	Distributed source for water content in ionomer [$\text{mols H}_2\text{O}/\text{cm}^3\text{s}$]
t :	Time [s]
T :	Temperature, [K]
\vec{u} :	Diffusion velocity [cm/s]
U_0 :	Thermodynamic equilibrium potential, [V]
\vec{U} :	Velocity vector, [cm/s]
\vec{v} :	Velocity [cm/s]
$\vec{v}_{(\text{H}_2\text{O}/\text{H}^+)}$:	Proton and water velocity in hydrodynamic motion [cm/s]
Vol:	Averaging volume
\vec{w} :	Interface velocity [cm/s]
W :	Molecular weight, [g/mols]
Y :	Mass fraction.

Greek Symbols

α_c^e, α_a^e :	Cathodic and anodic transfer coefficients
ε :	Surface porosity
ε_i :	Volume fraction of ionomer in the averaging volume
$\underline{\varepsilon}_A$:	Directional surface permeability of ionomer
ε_V :	Volumetric porosity
η :	Activation polarization, [V]
λ :	Water content [$\text{mols H}_2\text{O}/\text{mols SO}_3^-$]
μ :	Chemical potential [J]
ω_c :	Electrochemical reaction rate at cathode, [$\text{mols}/\text{cm}^3\text{s}$]
ρ :	Density, [g/cm^3]
ρ_{dry} :	Density of dry ionomer [g/cm^3]
μ :	Viscosity, [Ns/cm^2]
ν :	Stoichiometric coefficient

σ : Ionomer conductivity, [$\Omega^{-1}\text{cm}^{-1}$]

Φ : Potential, [V].

Subscripts

a : Anode

c : Cathode

cr : Critic

EOD: Electro-osmotic discharge

$,i$: Parameter defined in ionomer-phase

$,s$: Parameter defined in the solid electrically conductive phase

$,f$: Parameter defined in any of the fluid phases in catalyst layer pores

$,is$: Parameter defined in the at is -interface (three-phase boundary region)

$,if$: Parameter defined in the at if -interface

$,isf$: Parameter defined at the line between i , s and f phases.

Superscripts

a : Anodic

c : Cathodic

sat: Saturation.

Acknowledgment

This material was prepared with the financial support of the U.S. Department of Energy under Award no. DE-PS36-07G097012.

References

- [1] V. Gurau and J. A. Mann, "A critical overview of computational fluid dynamics multiphase models for proton exchange membrane fuel cells," *SIAM Journal on Applied Mathematics*, vol. 70, no. 2, pp. 410–454, 2009.
- [2] V. Gurau, T. A. Zawodzinski, and J. A. Mann, "Two-phase transport in PEM fuel cell cathodes," in *Proceedings of the PEMSIM Workshop on Modeling and Simulation of PEM Fuel Cells*, Berlin, Germany, September 2006.
- [3] V. Gurau, T. A. Zawodzinski Jr., and J. A. Mann Jr., "Numerical investigation of water transport in the PEMFC components," *ECS Transactions*, vol. 3, no. 1, pp. 1095–1104, 2006.
- [4] V. Gurau, T. A. Zawodzinski Jr., and J. A. Mann Jr., "Two-phase transport in PEM fuel cell cathodes," *Journal of Fuel Cell Science and Technology*, vol. 5, no. 2, Article ID 2821597, 12 pages, 2008.
- [5] M. Uchida, Y. Aoyama, N. Eda, and A. Ohta, "Investigation of the microstructure in the catalyst layer and effects of both perfluorosulfonate Ionomer and PTFE-loaded carbon on the catalyst layer of polymer electrolyte fuel cells," *Journal of the Electrochemical Society*, vol. 142, no. 12, pp. 4143–4149, 1995.
- [6] A. S. Aricò, P. Cretì, P. L. Antonucci, J. Cho, H. Kim, and V. Antonucci, "Optimization of operating parameters of a direct methanol fuel cell and physico-chemical investigation of catalyst-electrolyte interface," *Electrochimica Acta*, vol. 43, no. 24, pp. 3719–3729, 1998.
- [7] S. Wang, G. Sun, Z. Wu, and Q. Xin, "Effect of Nafion[®] ionomer aggregation on the structure of the cathode catalyst layer of a DMFC," *Journal of Power Sources*, vol. 165, no. 1, pp. 128–133, 2007.
- [8] K. Kanamura, H. Morikawa, and T. Umegaki, "Observation of interface between Pt electrode and Nafion membrane," *Journal of the Electrochemical Society*, vol. 150, no. 2, pp. A193–A198, 2003.
- [9] M. Eikerling, S. J. Paddison, L. R. Pratt, and T. A. Zawodzinski Jr., "Defect structure for proton transport in a triflic acid monohydrate solid," *Chemical Physics Letters*, vol. 368, no. 1–2, pp. 108–114, 2003.
- [10] N. Agmon, "The Grotthuss mechanism," *Chemical Physics Letters*, vol. 244, no. 5–6, pp. 456–462, 1995.
- [11] K.-D. Kreuer, S. J. Paddison, E. Spohr, and M. Schuster, "Transport in proton conductors for fuel-cell applications: simulations, elementary reactions, and phenomenology," *Chemical Reviews*, vol. 104, no. 10, pp. 4637–4678, 2004.
- [12] M. H. Eikerling, K. Malek, and Q. Wang, "Catalyst layer modeling: structure, properties and performance," in *PEM Fuel Cell Electrocatalysts and Catalyst Layers, Fundamentals and Applications*, J. Zhang, Ed., pp. 381–446, Springer, London, UK, 2008.
- [13] J. C. Slattery, "Flow of viscoelastic fluids through porous media," *American Institute of Chemical Engineers Journal*, vol. 13, p. 1066, 1967.
- [14] S. Whitaker, "Diffusion and dispersion in porous media," *American Institute of Chemical Engineers Journal*, vol. 13, p. 420, 1967.
- [15] J. C. Slattery, *Momentum, Energy and Mass Transfer in Continua*, Robert E. Krieger Publishing, New York, NY, USA, 1981.
- [16] S. Whitaker, *The Method of Volume Averaging*, Kluwer Academic Publishers, Dordrecht, The Netherlands, 1999.
- [17] N. I. Kolev, *Multiphase Flow Dynamics. 1. Fundamentals*, Springer, Berlin, Germany, 2002.
- [18] W. T. Sha and B. T. Chao, "Novel porous media formulation for multiphase flow conservation equations," *Nuclear Engineering and Design*, vol. 237, no. 9, pp. 918–942, 2007.
- [19] M. Watanabe, H. Igarashi, and K. Yosioka, "An experimental prediction of the preparation condition of Nafion-coated catalyst layers for PEFCs," *Electrochimica Acta*, vol. 40, no. 3, pp. 329–334, 1995.
- [20] B. S. Pivovar, "An overview of electro-osmosis in fuel cell polymer electrolytes," *Polymer*, vol. 47, no. 11, pp. 4194–4202, 2006.
- [21] T. A. Zawodzinski Jr., C. Derouin, S. Radzinski, et al., "Water uptake by and transport through Nafion[®] 117 membranes," *Journal of the Electrochemical Society*, vol. 140, no. 4, pp. 1041–1047, 1993.
- [22] T. A. Zawodzinski, T. E. Springer, J. Davey, J. Valerio, and S. Gottesfeld, "Water transport properties of fuel cell ionomers," in *Proceedings of the Symposium on Modeling of Batteries and Fuel Cells*, R. E. White, M. W. Verbrugge, and J. F. Stockel, Eds., p. 187, The Electrochemical Society, Pennington, NJ, USA, 1990, PV- 91-10.
- [23] T. A. Zawodzinski, J. Davey, J. Valerio, and S. Gottesfeld, "The water content dependence of electro-osmotic drag in proton-conducting polymer electrolytes," *Electrochimica Acta*, vol. 40, no. 3, pp. 297–302, 1995.
- [24] T. Y. Toong, *Combustion Dynamics: The Dynamics of Chemically Reacting Fluids*, McGraw-Hill, New York, NY, USA, 1983.
- [25] R. B. Bird, W. E. Stewart, and E. N. Lightfoot, *Transport Phenomena*, John Wiley & Sons, New York, NY, USA, 1960.

- [26] T. E. Springer, T. A. Zawodzinski, and S. Gottesfeld, "Pseudo homogeneous catalyst layer model for polymer electrolyte fuel cell," in *Proceedings of the Symposium on Modeling of Batteries and Fuel Cells*, R. E. White, M. W. Verbrugge, and J. F. Stockel, Eds., The Electrochemical Society Proceedings Series, pp. 197–208, Pennington, NJ, USA, 1990, PV 91-10.

Research Article

Experimental and Numerical Study on the Cold Start Performance of a Single PEM Fuel Cell

Calvin H. Li¹ and G. P. Peterson²

¹Department of Mechanical, Industrial, and Manufacturing Engineering, The University of Toledo, Toledo, OH 43606, USA

²Woodruff School of Mechanical Engineering, Georgia Institute of Technology, Atlanta, GA 30332-0325, USA

Correspondence should be addressed to Calvin H. Li, calvin.li@utoledo.edu

Received 7 May 2009; Revised 30 July 2009; Accepted 14 August 2009

Academic Editor: Moran Wang

Copyright © 2010 C. H. Li and G. P. Peterson. This is an open access article distributed under the Creative Commons Attribution License, which permits unrestricted use, distribution, and reproduction in any medium, provided the original work is properly cited.

A combined experimental and analytical investigation of single proton exchange membrane (PEM) fuel cells, during cold start, has been conducted. The temperature influence on the performance of a single PEM fuel cell and the cold start failure of the PEM fuel cell was evaluated experimentally to determine the failure mechanisms and performance. The voltage, current, and power characteristics were investigated as a function of the load, the hydrogen fuel flow rate, and the cell temperature. The characteristics of cold start for a single PEM fuel cell were analyzed, and the various failure mechanisms were explored and characterized. In an effort to better understand the operational behavior and failure modes, a numerical simulation was also developed. The results of this analysis were then compared with the previously obtained experimental results and confirmed the accuracy of the failure mechanisms identified.

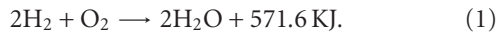
1. Introduction

Since the energy crisis of the early 70s, U.S. dependence on imported petroleum has remained one of the most pressing national security issues. Moreover, the fossil fuels consumption has brought about a number of social problems, as well, such as air quality deterioration, greenhouse gas emissions, and concentrated fossil fuel energy infrastructure. Hydrogen and fuel cell technologies emerged as one of the most favorable solutions to diversify energy resources and to solve the social problems along with other renewable energy explorations. Much research and developments have been carried out to advance hydrogen and fuel cell technologies, which could reduce the cost and enhance the efficiency and performance. Those efforts have successfully accelerated the advancement of hydrogen generation and storage, fuel cell applications, and related infrastructure. The Proton Exchange Membrane (PEM) fuel cells have been recognized as an outstanding candidate to be employed in the portable applications, such as automobile engines, to reduce fossil fuel demand and air pollution. The first use of a fuel cell system in space was in the Gemini program in August 21,

1962. More recently, successful applications of PEM fuel cells in automobiles have been reported in the past several years, and it promises to be a huge market in the next decades to offer clean energy for people [1]. Most hydrogen cars are currently only available in demonstration models or in a lease construction in limited numbers and are not yet ready for general public use [2]. Honda Inc. has leased its PEM fuel cells cars for the Japanese government and the U.S. government since 2008 and Nissan Inc. started testing a new fuel cell vehicle in Japan in 2009 [3, 4]. Despite the exciting advantages of the PEM fuel cells, there is a thermal issue on the PEM fuel cells working temperature range. Generally, when the temperature drops below freezing, not only will the performance of the fuel cells be severely reduced but also it is difficult to start up PEM fuel cells, as well, due to the temperature requirement for the liquid phase water in the Membrane Electrode Assembly (MEA) and Gas Diffusion Layers (GDLs).

The chemical reaction behind the fuel cell operation is surprisingly simple. The PEM fuel cells consume hydrogen and oxygen (from the air) to produce electricity with by-products of water and waste heat. The chemical reaction

between hydrogen and oxygen is shown below.



The above equation indicates that for every two moles of hydrogen combining with one mole of oxygen, 571.6 KJ of energy is generated. Converting this to a more common unit of watts, a perfectly efficient fuel cell would deliver 7.94 W of heating power if it consumed hydrogen at a mass rate of 0.1 mol/h which would be 0.333 cc/s for the experiments under the standard conditions. When a large amount of hydrogen was consumed, waste heat would accumulate and the temperature would rise beyond the limit of the fuel cell working range. This raised temperature needs thermal management to keep the fuel cell temperature within the working range. Along with waste heat, water is another main issue of PEM fuel cells.

Since the heat and water management is critically important to the optimization of the steady state performance of PEM fuel cells and the cold start of subfreezing environmental temperature, many experiments have been conducted to study the water and temperature effects on the PEM fuel cells working and starting at a subfreezing temperature. [1–8]. These PEM fuel cell experiments or simulations were subjected to a series of freeze/thaw cycles to understand how the freeze/thaw cycles affected the inner components of the fuel cells as well as their performance. Hishinuma et al. [5] discussed the performance of a PEM fuel cell at the working temperature from -3°C to -25°C through experimental and simulation work. The results showed that heat generated in the PEM fuel cell would be enough to keep the fuel cell warm enough and self start at a temperature of -5°C . It also demonstrated with simulation results that freezing started at the downstream side of the cathode channel where the partial pressure of the steam was higher. Oszcipok et al. [6] focused their study on subfreezing temperature startup behavior of PEM fuel cells. It was found that startup water production would lead to decay in the performance by forming ice layers in the electrode and gas diffusion layers (GDLs). The effects of membrane thickness, gas flow rate, and the humidification have been investigated experimentally. It was concluded that, in order to start up at -10°C , a high load with a high air flow rate was recommended. Um and Wang [7] studied the water transport in a PEM fuel cell with the numerical method. The water diffusion, convection, and electro-osmotic transport models were investigated to find out the fuel cell water transport characteristics under various inlet gas humidifications and membrane humidifications. It was shown that a thick membrane would reduce the back-diffusion of water and the humidification of gas would change the fuel cell performance with a counter-flow arrangement. Bao et al. [8] simulated the whole water and thermal management in a PEM fuel cell system, that is, the fuel cell stack itself, the radiator, the condenser, and humidifier. The effects of humidification of different components and work conditions on the water and thermal management design were studied. Hou et al. [9] experimentally studied the residual water effects on the PEM fuel cell after cold starts. Three different current densities and operation times were used to obtain different

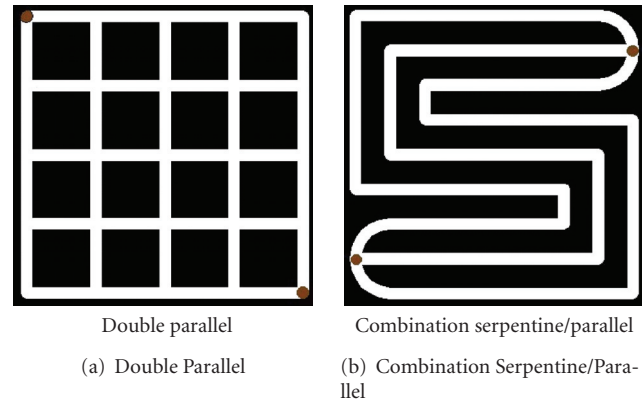


FIGURE 1: Sketch of Channel configurations.

amounts of residual water in the fuel cells. The fuel cells were also frozen at a temperature of -5°C for 1.5 hours after the desired residual water amount was achieved. It was reported that there were no changes on cell resistance or fuel cell performance with regard to the amount of residual water in the fuel cells. It was then concluded that only a very small portion of residual water was in the catalyst layer and more of the water was frozen in the gas diffusion layers or gas channels. More recently, Pinton et al. [10] studied the PEM fuel cell startup performance at subfreezing temperatures with both experiments and analysis. It was observed that there was an optimal wetting level of the PEM fuel cell membrane at which accumulated heat could achieve its maximum. It was concluded that ice forming both on the cathode layer pores and in active reaction sites would introduce starving by increasing the electrical resistance.

Based on the previous literature results, an experimental study has been conducted to study the PEM fuel cell performance and start-up behavior at the temperature above and below freezing. The temperature distribution within the fuel cell was monitored with a number of strategically placed thermocouples that were placed in the gas flow channel of the fuel cell and positioned in direct contact with the membrane electrode assembly (MEA). The information about temperature distribution could affect a better understanding how MEA temperature affects the fuel cell performance. Additionally, the flow rates of the two gasses used by the fuel cell—hydrogen and air—were measured as they entered the fuel cell and that data recorded. Current and voltage produced by the fuel cell were recorded, thus allowing the power output of the fuel cell to be calculated. The data collected along with other, gained through experiments, enabled the knowledge of PEM fuel cell performance in a harsh environment to assist commercialization of PEM fuel cell automobiles operating at subfreezing temperatures.

2. Experimental Facility

The in-house constructed PEM fuel cells were a double parallel gas flow channel design and a combination parallel/serpentine gas flow design, both shown in Figure 1. The white portions of the figures are channels of 0.32 cm (1/8 inch) wide and 0.24 cm (3/32 inch) deep, machined out

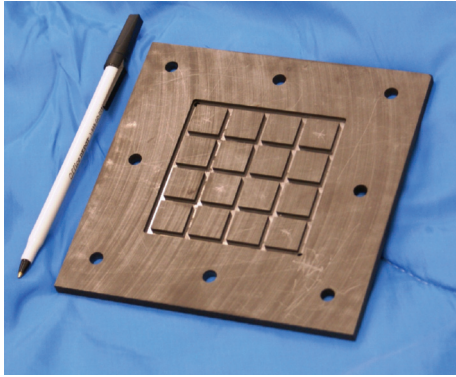


FIGURE 2: Double parallel design graphite plate.

of graphite plates. The black portions are the untouched graphite surface, which made direct contact with the MEA after the fuel cell was assembled. The two dots on each design are the gas fuel inlet and outlet. During our experimental tests, it was discovered that there was no difference between those two different gas channel designs in terms of PEM fuel cell performance under the same conditions.

The single PEM fuel cells consisted of a commercial MEA with GDL (Nafion base), two monoplular plates of graphite, two thin nickel metallic sheets as the electrodes, and two polycarbonate supporting plates. The machined double parallel design of Figure 2 and the exploded view of the PEM fuel cell assembly of Figures 3(a) and 3(b) are shown hereinafter.

With the development of single PEM fuel cells, an environmental chamber test station was built to control the single fuel cell operating temperature with a pair of cryostat baths. This test station enables the research on the PEM single fuel cells performance in a temperature range of -20°C through 80°C . K-type thermocouples were placed within the graphite channels to record the temperature variance inside the gas channels and at the entrances and exits. Additional thermocouples were placed within the un-machined square portions of the graphite plates which were in direct contact with the MEA. Holes were drilled through the graphite plates and the thermocouples were positioned in holes slightly above the surface of the graphite plates which allowed the thermocouples to come in contact with the MEA without damaging its delicate surface.

In the experiments, hydrogen and mixed gas (air, 21% oxygen) were forced through the groove on the graphite plate with flow valves. The gas humidification was controlled with conventional bubble humidifiers. The current and voltage were controlled with various electronic resistance loads. All data were collected through a data logger (a 40-channel thermocouple amplifier HP 34970A data acquisition system at a DAQ rate of 100 fps).

The experimental procedure is the following: first, the in-house made single cell PEM fuel cell was tested at room temperature, 25°C . The power output, current, and voltage were tested against various hydrogen flow rates and electric resistance loads. Then, the single cell PEM fuel cell was put into the environmental chamber for an ambient temperature change from room temperature, 25°C , to subfreezing temperature, -5°C . The currents and powers of the PEM

fuel cell performance have been recorded. Next, the ambient temperature was kept at -5°C , and the currents and powers of cold start and performance have been recorded. Lastly, the ambient temperature inside the environmental chamber has been further reduced to -10°C . The single cell PEM Fuel cell currents and powers of cold start and performance have been investigated.

3. Results of the Initial Single Fuel Cell Experiments at Room Temperature

The results from the initial ambient room temperature tests are shown in Figure 4. In these tests, experiments were conducted by varying flow rates of hydrogen while monitoring the voltage and the current changes, due to the different hydrogen flow rates to find out the effects of hydrogen flow rate on the in-house built single PEM fuel cell performance. A $3\ \Omega$ resistance load was applied as the load in the tests. The fuel cell was oriented vertically. The air flow rate was approximate $36\ \text{cc}/\text{min}$. It was shown in Figure 4 that the hydrogen flow rate changing from $10\ \text{cc}/\text{min}$ to $30\ \text{cc}/\text{min}$ had no influence on the current, while the potential did experience a rise at the flow rate between $10\ \text{cc}/\text{min}$ and $20\ \text{cc}/\text{min}$. Based on those test results, it was decided to use the hydrogen flow rate around $10\text{--}20\ \text{cc}/\text{min}$ as the optimal flow rate, because the results seemed to indicate that the fuel cell could get the best performance at that flow rate range.

In order to ensure the conclusion that there was no influence of hydrogen flow rate on the performance of single PEM fuel cells, it has been tried in experiments with higher flow rates. Figure 5 shows the performance of the fuel cell over time using flow rates of hydrogen between 114 and $260\ \text{cc}/\text{min}$. A flow rate of air at $360\ \text{cc}/\text{min}$ was used for these tests. The two gas fuels were connected in a count-flow orientation and a $3\ \Omega$ load was used, as well.

As shown in Figure 5, there was no change in the performance of the fuel cell even though the hydrogen flow rate had been dramatically increased from the previous highest rate of $32\ \text{cc}/\text{min}$ to $260\ \text{cc}/\text{min}$. Thus, the flow rates of hydrogen flowing around $10\text{--}20\ \text{cc}/\text{min}$ have been adopted for the remaining tests.

Additional tests have been carried out to find the best performance of the single PEM fuel cells by changing the load to the fuel cells, as shown in Figure 6. The tests were conducted at ambient room temperature. Still, the two gas fuels were connected in a count-flow orientation. The flow rate of hydrogen was $20\ \text{cc}/\text{min}$ and the flow rate of air was $260\ \text{cc}/\text{min}$. It was found that with increases of the potential, the current would decrease and the power output would decrease in spite of the increase of potential. The results demonstrated that a high current would be desirable in the future cold start tests at subfreezing temperatures to get the maximal heating effect.

4. Experimental Results of the Single Fuel Cell in an Environmental Chamber above -5°C

After the ambient temperature tests were finished, subfreezing temperature tests were carried out in the environmental

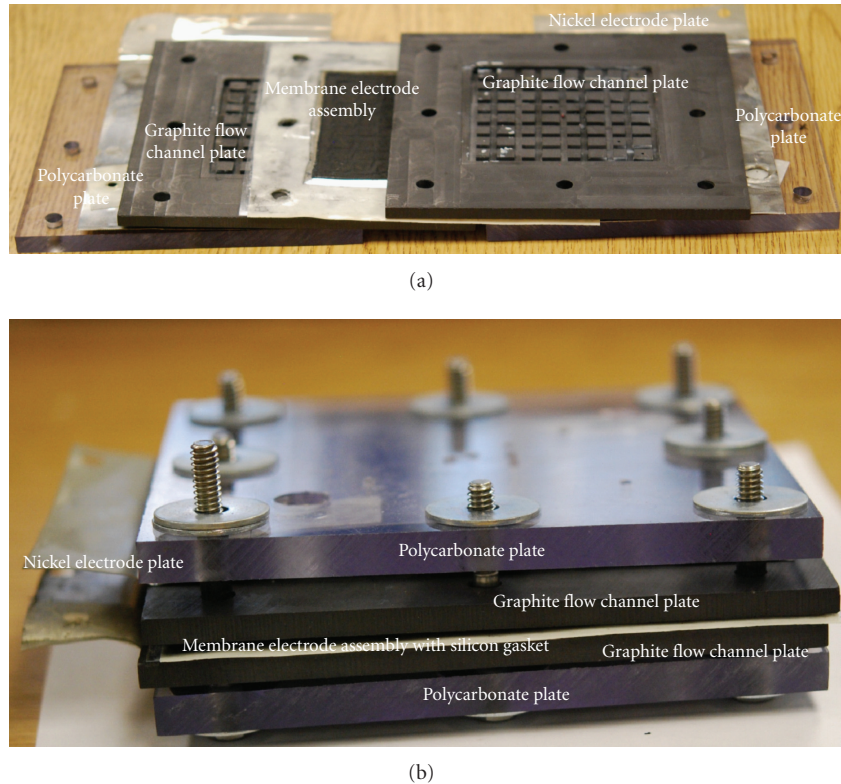


FIGURE 3: Exploded view of the PEM fuel cell assembly of both gas channel designs.

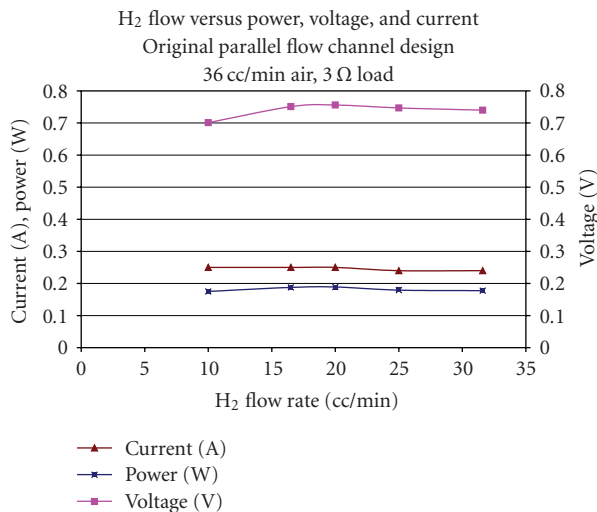


FIGURE 4: The performance of fuel cell (Voltage, current, and power) versus hydrogen flow rate.

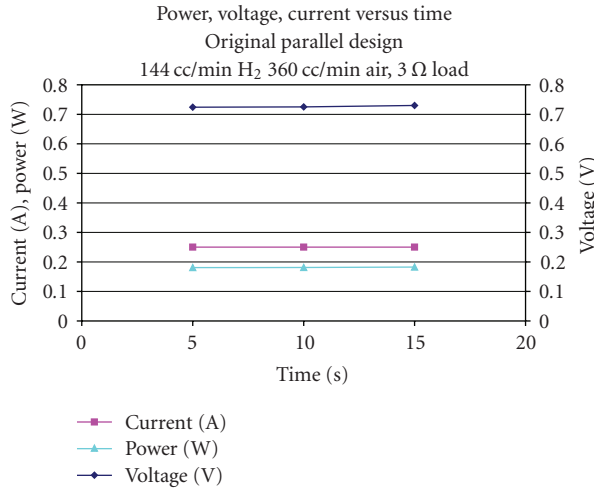
chamber. The first test focused on the ambient temperature above 0°C. A hydrogen flow rate of 20 cc/min and an air flow rate of approximately 260 cc/min were employed. A 46 Ω resistance was used as a load. The results of the test are shown in Figures 7 and 8.

It was found that when the ambient temperature was set to be 0°C, the temperature of the MEA in the single PEM fuel cell would decrease from 22°C to 12°C in a time period

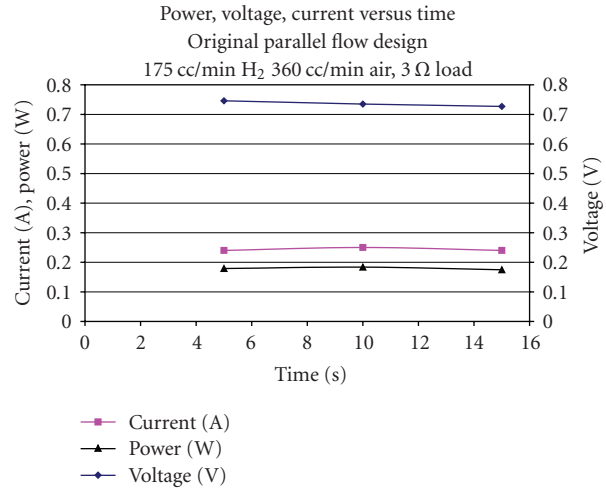
of 6000 seconds. However, even with a load of 46 Ohms to generate a small desired power output, the single PEM fuel cell still could successfully start up at this 0°C environment and was able to keep the power output at a stable value after the fuel cell started up. This result means that enough heat was generated by the fuel cell reaction to keep the water produced, from freezing in the gas channel and in the gas diffusion layer. The reaction and proton diffusion were not affected by the 0°C environmental temperature in the testing time period.

The current change after the cold start at 0°C was presented in Figure 8. It was clearly shown that the current quickly rose to the stable value and kept the value in the test time period. No deterioration of current value has been observed.

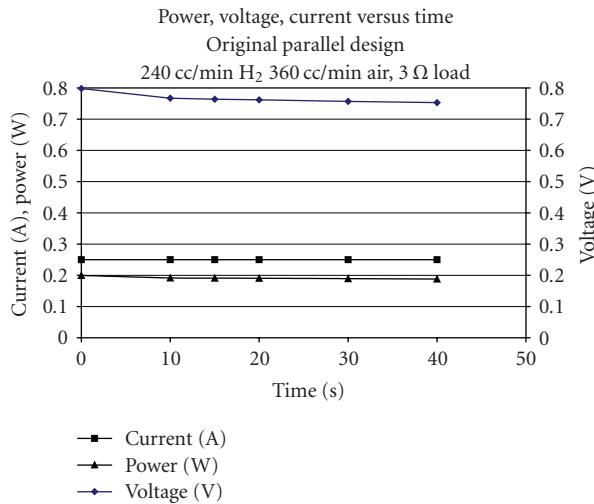
For the next subfreezing temperature test, the same fuel cell was tested again under the same conditions as before except that the ambient temperature was set to -5°C. The results are shown in Figure 9. It was illustrated that the single PEM fuel cell would start up at the -5°C ambient temperature without any difficulty. The current jumped to a value close to 18 mA and then decreased gradually to around 15 mA in a time period of 8000 seconds. The high start value was due to the residual liquid water left from the previous 0°C ambient temperature test, which brought to a good protonic conduction of MEA. After more water was produced by the chemical reaction, the membrane protonic conductivity had experienced a small decrease. This might be caused by too much water residing in the membrane



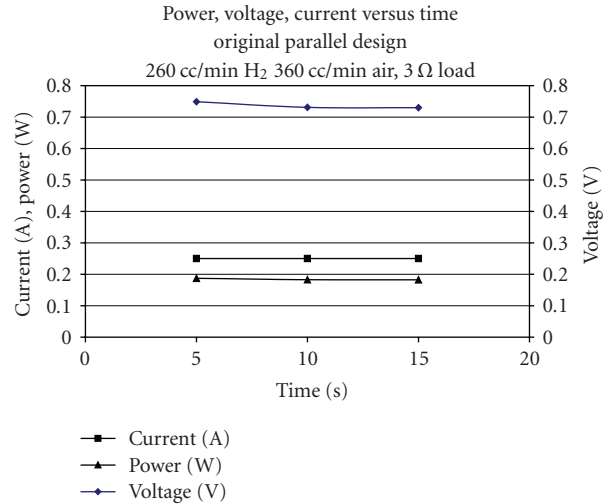
(a) The performance of fuel cell versus the time at hydrogen flow rate of 144 cc/min



(b) The performance of fuel cell versus the time at hydrogen flow rate of 175 cc/min



(c) The performance of fuel cell versus the time at hydrogen flow rate of 240 cc/min.



(d) The performance of fuel cell versus the time at hydrogen flow rate of 260 cc/min

FIGURE 5: The high hydrogen flow rate tests.

and there was a gentle flooding inside the single PEM fuel cell.

As a result, the experimental tests on the single PEM fuel cell demonstrated that the performance and startup of single PEM fuel cell had not been affected by the ambient temperature above -5°C . Even with a large load and a small current, that is, a small heat production, the single PEM fuel cell still could be able to work appropriately when the heat generated was enough to keep the residual water in the MEA from thoroughly frozen.

5. The Cold Start and Performance of a Single PEM Fuel Cell at -10°C

The evolution of the current and power output of the single PEM fuel cell at a load of 46 Ohms is presented in Figures

10 and 11. Once the electric circuit was connected, both the single PEM fuel cell current and power output quickly rose to their maximums of 7 mA and 11 mW first and stayed at the neighborhoods for a few minutes. Then both the current and power output quickly dropped to the values of 1 mA and 1 mW. Finally, both slowly decayed to zero in the last 10000 seconds. Due to fact that the membrane was dry before the test, water produced would be absorbed by the membrane, which enabled further chemical reaction. After a few minutes, too much water had been generated, while there was not enough heat to maintain the water in the liquid phase at the temperature of -10°C . As a result, water started to freeze inside the gas diffusion layer and the catalyst layer.

The reasons for the failure of startup would be first; once the single PEM fuel cell started, water and heat would be the by-product along with the electrical current and power

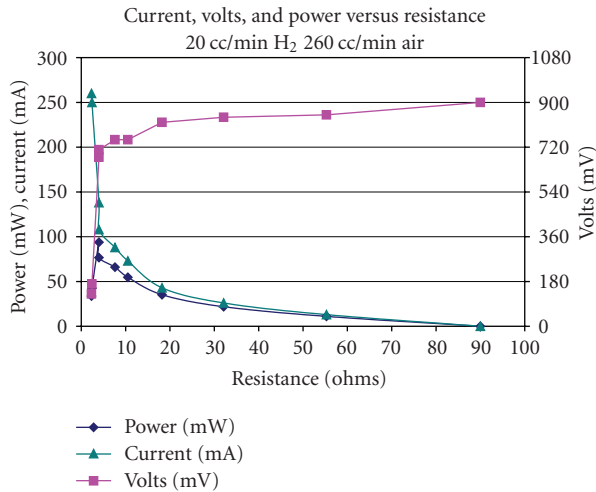


FIGURE 6: The performance of fuel cell versus the load at hydrogen flow rate of 20 cc/min.

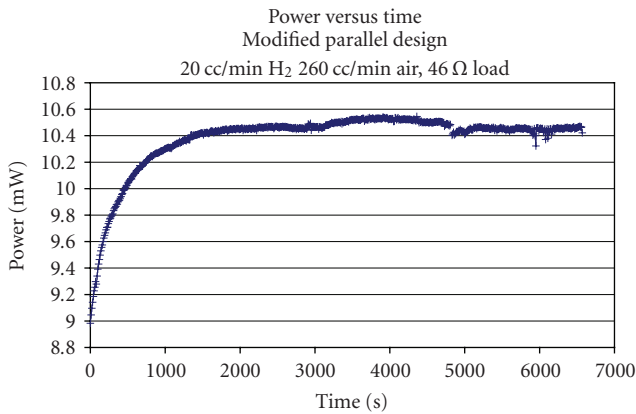


FIGURE 7: The power of fuel cell vs. time at the fuel cell temperature decreasing from 25°C to 10°C.

output, and the heat generated during the first several-minute chemical reaction was not enough to stop the water produced from freezing in the gas diffusion layer and on the catalyst layer. Once the ice started to cover the reactive area of the membrane and blocked the absorption and diffusion of gas molecules, the current and power output dropped and then decayed to zero. The reason that the current and power output kept at their maximums for a few minutes was due to the fact that at a low current, only a small amount of water was produced, and it needed a relatively long time period to accumulate enough water to cover the cathode catalyst active area; once the enough water had been produced and frozen to ice, the single PEM fuel cell started to fail.

Next, a small load of 3 Ohms was employed to study the cold start of a single PEM fuel cell at a relatively large initial power output. As shown in Figures 12 and 13, the current increased to a maximum of 8 mA quickly, as did the power output. Then, instead of staying in the region of their maximum of their maximum value for a few minutes, both started to drop immediately. This decrease took a

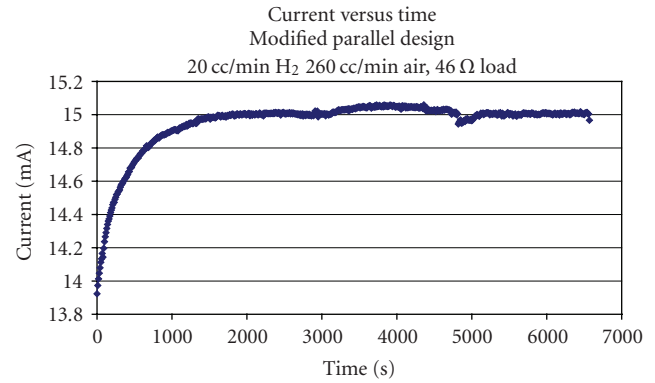


FIGURE 8: The current of fuel cell vs. time at fuel cell temperature decreasing from 25°C to 10°C.

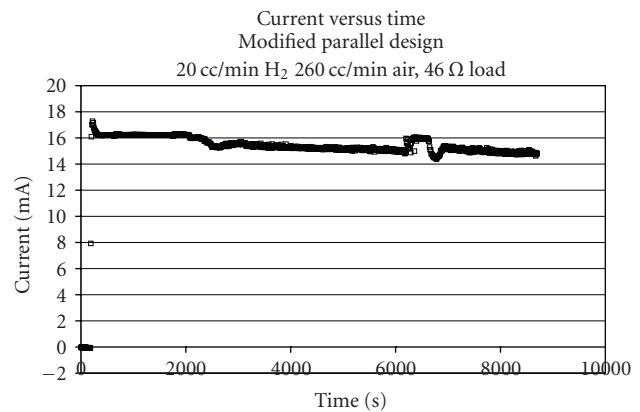


FIGURE 9: The current versus time at temperature of -5°C.

relatively long time period for both current and power output compared to the first -10°C test. After reaching the bottom of close to zero, both showed a slow increasing trend to reach a secondary maximum (3 mA and 9 mW, resp.) at a time of approximate 5000 seconds after the primary maximum. Afterward, both decayed to around zero in the rest of 10000 seconds.

The difference between the previous cold start at -10°C and the latter one is that, first, once the current and power output reached their maximums, the current and power output of the latter test did not stay around at the neighborhoods of the maximums. Rather, both decreased immediately. Second, the decrease of both current and power output in the latter test was rather gradual compared to the drop of both in the previous test. Finally, there were secondary maximums in the latter test for both current and power output.

The reasons for the differences are, first, even though care has been taken to keep the membrane equally dry for both tests, there was still plenty of residual water in the membrane in the second test. This is illustrated by the fact that the current and power output did not stay around at the maximums. Second, along with the higher power output, the single PEM fuel cell was able to produce much more heat in the second test than that in the first test. The icing process

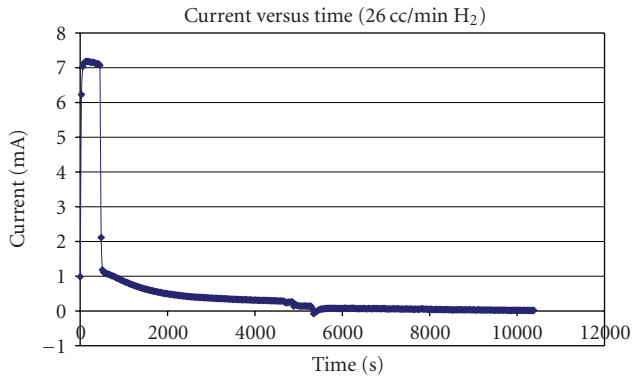


FIGURE 10: The evolution of current versus time at the temperature of -10°C .

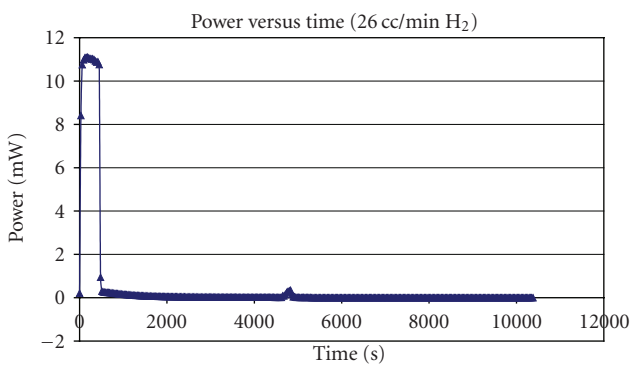


FIGURE 11: The evolution of power output versus time at the temperature of -10°C .

of residual water in the second test was much slower than that in the first test, as evidenced by a gradual decrease of both current and power output. Third, the fuel cell would try to restart if the icing was reduced. Since the air flow was not stopped after the cold start failure, the air would blow the water molecules with it out of the single PEM fuel cell. Once the protonic conductivity re-established, the single PEM fuel cell would have a secondary maximum on both current and power output, which was the sign of fuel cell restart. However, due the same reason that water produced in the chemical reaction would freeze soon at the temperature of -10°C , the single PEM fuel cell was not able to generate enough heat and to keep the water from freezing into ice. As a result, the restart would fail once the ice covered the active reaction area and blocked the protonic conduction.

6. Model Description and Assumptions

In order to understand the inner working mechanism of PEM Fuel cells, numerical computational simulation efforts have been devoted to gain insight of the heat/mass transfer, gas/liquid flow, electrochemical kinetics, and power density [11–14]. Ferng et al. [11] employed a two-phase multi-component flow model and a simplified electrochemical reaction equation to study PEMFC performance under the influence of operating temperature and pressure and low

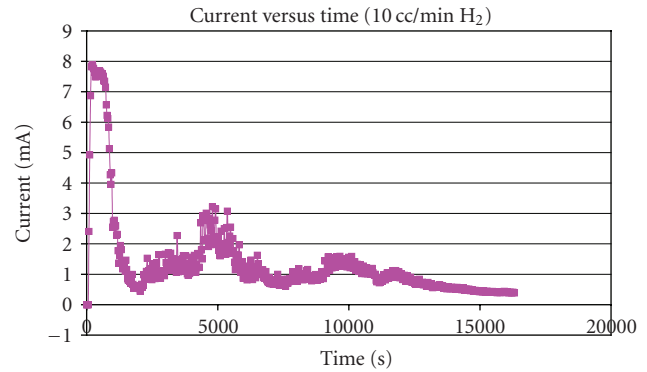


FIGURE 12: The current versus time of the cold start of a single PEM Fuel cell at -10°C .

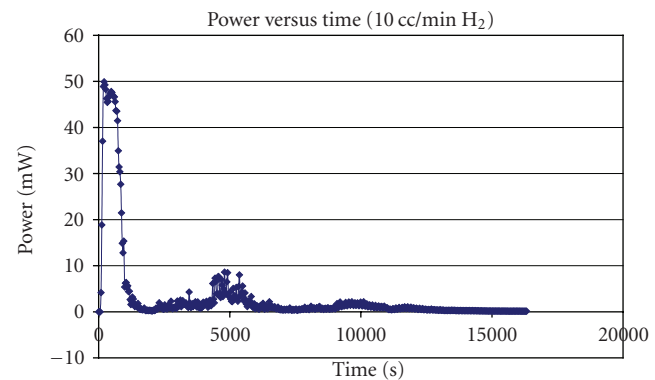


FIGURE 13: The power output versus time of the cold start of a single PEM Fuel cell at -10°C .

characteristics within the cell. The simulation results have been compared with experimental data, which illustrated the increase in cell performance at elevated temperature. Siegel et al. [12] adopted a two-dimensional model, which includes the transport of liquid water within the porous electrodes as well as the transport of gaseous species, protons, energy, and water dissolved in the ion conducting polymer. Electrochemical kinetics are modeled with standard rate equations adapted to an agglomerate catalyst layer structure. Some of the physical properties used in constructing the model are determined experimentally. Zhang et al. [13] applied the Powell algorithm to find the optimum values of multiple parameters while optimizing the potential of the electrolyte phase at the membrane/cathode interface at a typical value of the cell voltage.

The current simulation domain consisted of two gas diffusion layers and one sandwiched active catalyst layer, as shown in Figure 14. The active catalyst layer was 100 microns thick and 2000 microns long, while the gas diffusion layers were 250 microns thick and 2000 microns long with a center deformation of 100 microns deep and 500 microns long due to the pressure of graphite plate gas channel assembling. The hydrogen moved from the bottom entrance up to the top exit, while the air entered through the top opening and exited at the bottom opening. The protons were generated at anode side and migrated to the cathode side. Water was generated

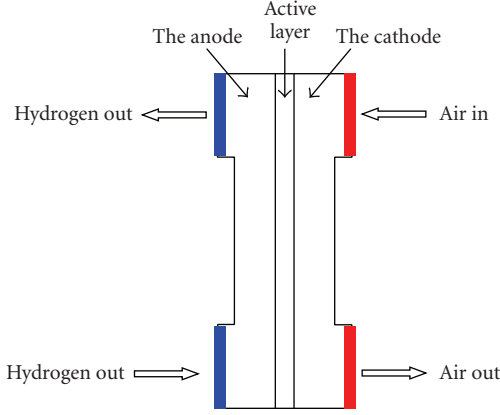


FIGURE 14: The sketch of the PEM fuel cell domain.

due to the chemical reaction on the cathode side. Water was experiencing a migration with proton from the anode side to the cathode side and a concentration-osmotic diffusion from cathode to the anode. The gas fuels and water transportation inside the porous layers were treated as continuous phases in homogeneous porous media with uniform morphological properties. The pressure and flows inside the porous media were controlled by Darcy's law and Maxwell-Stefan mass transport model [14]. The current density in the active layer was calculated by solving the diffusion equation and the Butler-Volmer electrode kinetic equation under constant electric and ionic potentials. The simulation was conducted with Comsol 3.4 package [15].

A conductive media DC application mode describes the potential distributions in the three subdomains using the following equations:

$$\begin{aligned} \nabla \cdot (-k_{s,\text{eff}} \nabla \phi_s) &= 0 \quad \text{in } \Omega_a, \\ \nabla \cdot (-k_{m,\text{eff}} \nabla \phi_m) &= 0 \quad \text{in } \Omega_m, \\ \nabla \cdot (-k_{s,\text{eff}} \nabla \phi_s) &= 0 \quad \text{in } \Omega_c. \end{aligned} \quad (2)$$

Here $k_{s,\text{eff}}$ is the solid-phase effective electronic conductivity (S/m) and $k_{m,\text{eff}}$ is the membrane ionic conductivity (S/m). The potential (V) in the electrode phases is denoted by ϕ_s and that in the membrane by ϕ_m .

The charge-transfer current density expression is described using the Butler-Volmer electrochemical kinetic expression, as a boundary condition. For the electrolyte potential equation, this results in a condition where the inward normal ionic current densities at the anode and cathode boundaries, i_a and i_c , are specified according to the equation:

$$i_e = L_{\text{act}}(1 - \varepsilon_{\text{mac}})j_{\text{agg},e}, \quad (3)$$

where the index e stands for "a" (anode) or "c" (cathode). Further, L_{act} is the active layer's thickness (m), its porosity ε_{mac} (the macroscopic porosity), and $j_{\text{agg},a}$ and $j_{\text{agg},c}$ are the current densities given by the agglomerate model.

The agglomerate model describes the current density in an active layer consisting of agglomerates of ionic

conductor material and electrically conducting particles covered partially with catalyst. The local current density can be expressed analytically by solving a combination of the diffusion equation and the Butler-Volmer electrode kinetic equation for an agglomerate with constant electric and ionic potentials. The resulting equations for the current density in the anode and cathode are

$$j_{\text{agg},e} = -6n_e F \left(\frac{D_{\text{agg}}}{R_{\text{agg}}^2} \right) (1 - \lambda_e \coth \lambda_e) \beta_e, \quad (4)$$

where, again, the index e stands for "a" (anode) or "c" (cathode), and

$$\begin{aligned} \lambda_a &= \sqrt{\frac{i_{0a} S R_{\text{agg}}^2}{2F c_{\text{H}_2, \text{ref}} D_{\text{agg}}}}, \\ \lambda_c &= \sqrt{\frac{i_{0c} S R_{\text{agg}}^2}{4F c_{\text{O}_2, \text{ref}} D_{\text{agg}}}} \exp\left(-\frac{F}{2RT} \eta_c\right), \end{aligned} \quad (5)$$

$$\beta_a = \left[c_{\text{H}_2, \text{ref}} - c_{\text{H}_2, \text{ref}} \exp\left(\frac{-2F}{RT} \eta_a\right) \right], \quad \beta_c = c_{\text{O}_2, \text{ref}}.$$

In these equations, D_{agg} is the agglomerate gas diffusivity (m²/s), R_{agg} is the agglomerate radius (m), η_e is a "charge transfer" number ("a" for the anode and "c" for the cathode), S is the specific area of the catalyst inside the agglomerate (1/m), and F is Faraday's constant (C/mol). Furthermore, $c_{i, \text{ref}}$ are the reference concentrations of the species (mol/m³), $c_{i, \text{agg}}$ are the corresponding concentrations in the agglomerate surface (mol/m³), i_{0a} and i_{0c} are the exchange current densities (A/m²), R is the gas constant, T is the temperature (K), and the over voltages at the anode and the cathode are given by

$$\eta_a = \phi_0 - \phi_m - E_{\text{eq},a}, \quad \eta_c = \phi_0 - \phi_m - E_{\text{eq},c}, \quad (6)$$

where E_{eq} (V) denotes the equilibrium voltage.

The anodic and cathodic reference states were equal to the molar fractions at the inlet channels of the anode and cathode, respectively, at 1 atm. The dissolved hydrogen and oxygen concentrations at the surface of the agglomerates are related to the molar fractions of the respective species in the gas phase through Henry's law:

$$c_{\text{agg},\text{H}_2} = \frac{p_{\text{H}_2} x_{\text{H}_2}}{K_{\text{H}}}, \quad c_{\text{agg},\text{O}_2} = \frac{p_{\text{O}_2} x_{\text{O}_2}}{K_{\text{O}}}, \quad (7)$$

where K is Henry's constant (Pa · m³/mol).

For the electric potential, the electrode boundary conditions are identical, setting the boundary normal current density but using the opposite sign. In addition, the potential difference between the cathode and anode current collectors corresponds to the total cell voltage. Choose the potential at the anode current collector as the reference level by setting it to zero. Then the total cell voltage serves as the boundary condition at the cathode current collector:

$$\begin{aligned} \phi_o &= 0 \quad \text{at } \partial\Omega_{a,cc} \\ \phi_o &= V_{\text{cell}} \quad \text{at } \partial\Omega_{c,cc}. \end{aligned} \quad (8)$$

To model the gas flows in the gas backings, the Darcy's Law application mode has been used. The gas velocity is given by the continuity equation according to

$$\nabla \cdot (\rho u) = 0 \quad \text{in } \Omega_a \text{ and } \Omega_c, \quad (9)$$

where ρ is the mixture density of the gas phase (kg/m^3) and u denotes the gas velocity (m/s). The flow velocity in porous media is determined by the gradient of pressure, the viscosity of the fluid, and the structure of the porous media according to Darcy's law:

$$u = -\frac{k_p}{\eta} \nabla p. \quad (10)$$

Here k_p denotes the electrode's permeability (m^2), η represents the gas viscosity ($\text{Pa} \cdot \text{s}$), and p is the pressure (Pa). The ideal gas law gives the gas phase's mixture density, ρ :

$$\rho = \frac{p}{RT} \sum_i M_i x_i. \quad (11)$$

In this equation, R denotes the gas constant ($\text{J}/(\text{mol} \cdot \text{K})$), T is the temperature (K), M is the molar mass (kg/mol), and x is the mole fraction.

At the electrode boundary for the anode and cathode, the gas velocity is calculated from the total mass flow given by the electrochemical reaction rate according to

$$\begin{aligned} -n \cdot u|_{\text{anode}} &= \frac{j_{\text{anode}}}{\rho F} \left(\frac{M_{\text{H}_2}}{2} + \lambda_{\text{H}_2\text{O}} M_{\text{H}_2\text{O}} \right) \\ -n \cdot u|_{\text{cathode}} &= \frac{j_{\text{cathode}}}{\rho F} \left(\frac{M_{\text{O}_2}}{4} + \left(\frac{1}{2} + \lambda_{\text{H}_2\text{O}} \right) M_{\text{H}_2\text{O}} \right). \end{aligned} \quad (12)$$

Combined with these boundary conditions, Darcy's law determines the gas flow velocity and preserves the total mass conservation in the anode and cathode gas backing.

For the mass transport in the porous layer, the Maxwell-Stefan Mass Transport model takes into account two species in the anode— H_2 and H_2O —and three at the cathode— O_2 , H_2O , and N_2 . The model uses one instance of the Maxwell-Stefan Diffusion and Convection application mode for each electrode. Maxwell-Stefan multicomponent diffusion is governed by the equations

$$\begin{aligned} \frac{\partial}{\partial t} \rho w_i + \nabla \cdot \left[-\rho w_i \sum_{j=1}^N D_{ij} \left\{ \frac{M}{M_j} \left(\nabla w_j + w_j \frac{\nabla M}{M} \right) \right. \right. \\ \left. \left. + (x_j - w_j) \frac{\nabla p}{p} \right\} + w_i \rho u + D_i^T \frac{\nabla T}{T} \right] = R_i \end{aligned} \quad (13)$$

which the software solves for the mass fractions, w_i . This particular PEM fuel cell model assumes that the temperature-driven diffusion is insignificant and sets the source term, R , to zero. For the cathode gas, with three species (oxygen = 1, water = 2, nitrogen = 3), the mass transport is described

by the following three equations together with Darcy's law, describing the flow rate:

$$\begin{aligned} \nabla \cdot \left\{ -\rho w_1 \sum_j \left[D_{1j} \left(\nabla x_j + (x_j - w_j) \left(\frac{\nabla p}{p} \right) \right) \right] \right\} \\ = -(\rho u \cdot \nabla w_1) \\ \nabla \cdot \left\{ -\rho w_2 \sum_j \left[D_{2j} \left(\nabla x_j + (x_j - w_j) \left(\frac{\nabla p}{p} \right) \right) \right] \right\} \\ = -(\rho u \cdot \nabla w_2) \\ w_3 = 1 - w_1 - w_2. \end{aligned} \quad (14)$$

Here p is the pressure (Pa), T is the temperature (K), and u is the velocity (m/s). The Maxwell-Stefan diffusivity matrix, D_{ij} (m^2/s), is calculated from the binary diffusivities specified in the application mode.

Finally, the feed-gas mass fractions are specified at the inlets. At the outlets, convective flux boundary conditions are applied, meaning that the flux is convection dominated. At the electrode-membrane boundary, the mass fluxes of hydrogen in the cathode, and of oxygen and water in the cathode, are determined by the electrochemical reaction rate:

$$\begin{aligned} -n \cdot N_{\text{H}_2, \text{anode}} &= \frac{j_{\text{anode}}}{2F} M_{\text{H}_2} \\ -n \cdot N_{\text{O}_2, \text{cathode}} &= \frac{j_{\text{cathode}}}{4F} M_{\text{O}_2} \\ -n \cdot N_{\text{H}_2\text{O}, \text{cathode}} &= \frac{j_{\text{cathode}}}{F} \left(\frac{1}{2} + \lambda_{\text{H}_2\text{O}} \right) M_{\text{H}_2\text{O}}. \end{aligned} \quad (15)$$

7. Simulation Results on the Single PEM Fuel Cells at the Temperature above and below -5°C

For the simulation of cold startup at the temperature of -5°C , the results indicated that the current density was lowest at the bottom and highest at the top inside of the active layer (Figure 15). The reason was that hydrogen gas flow would pick up more water vapor at the bottom than that at the top. More liquid water would appear at the top, which would assist the electro-chemical reaction. Henceforth, the current density was high at the top and low at the bottom. Similarly, it was illustrated in Figure 16 that the current density was high at the top corners of the electrode graphite plane gas channels, where the MEA might burn out at low humidity under the high concentration of the current density. This cold startup could generate enough water and heat to sustain the chemical reaction and maintain the power output of the single PEM fuel cell.

The simulation results at the temperature of -10°C were shown in Figures 17 and 18. It was demonstrated that the current density was high at the bottom while low at the top of the active layer (Figure 17). This is caused by the freezing -10°C temperature that water freezing happened at the top of the fuel cell. As a result, the current density at the top was

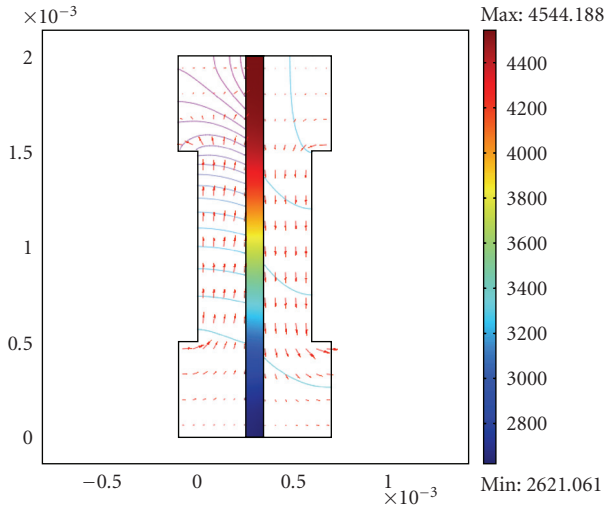


FIGURE 15: The current density on the active layer. The arrows are the flow velocity of each gas fuel (hydrogen and Oxygen) at -5°C . (surface: total current density, norm $[\text{A}/\text{m}^2]$, Contour: water, Arrow: velocity field).

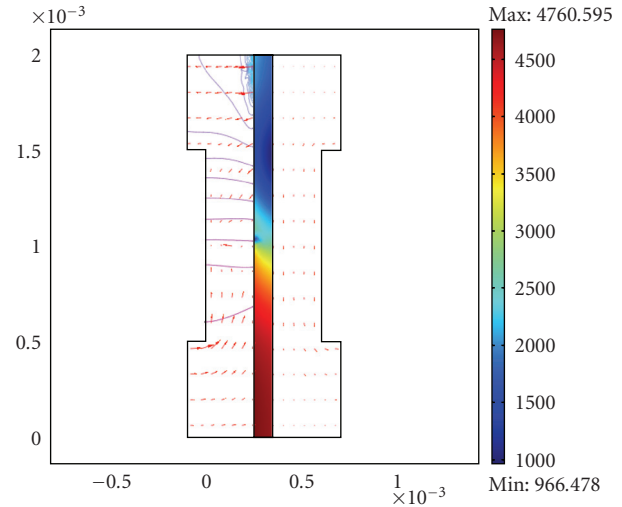


FIGURE 17: The current density on the active layer. The arrows are the flow velocity of each gas fuel (hydrogen and Oxygen) at -10°C . (surface: total current density, norm $[\text{A}/\text{m}^2]$, Contour: water, Arrow: velocity field).

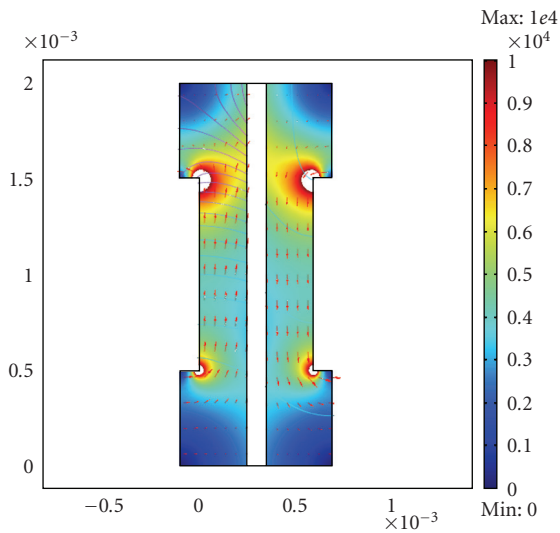


FIGURE 16: The current density in the anode and cathode layers. The arrows are the flow velocity of each gas fuel (hydrogen and Oxygen) at -5°C . (surface: total current density, norm $[\text{A}/\text{m}^2]$, Contour: water, Arrow: velocity field).

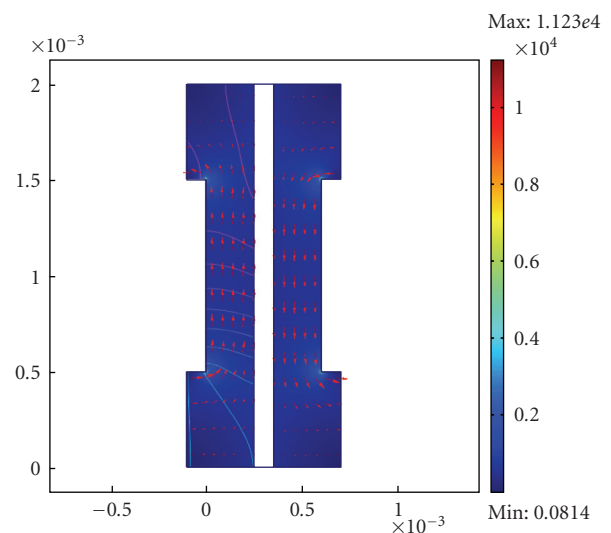


FIGURE 18: The current density in the anode and cathode layers. The arrows are the flow velocity of each gas fuel (hydrogen and Oxygen) at -10°C . (surface: total current density, norm $[\text{A}/\text{m}^2]$, Contour: water, Arrow: velocity field).

low. The current density in both anode and cathode were very low, which meant that the startup would fail and not sustainable power output would exist of the single PEM fuel cell (Figure 18).

The simulation results echoed the experimental conclusion that, at the temperature above -5°C , no extra heating was needed to start the single PEM fuel cell. While at the temperature of -10°C , the single PEM fuel cell could not start up successfully on its own, extra heating would be demanded to warm the fuel cell up above freezing temperature before the single PEM fuel cell could successfully maintain its power output.

8. Conclusions

A series of experiments on the cold start behavior of single PEM fuel cells has been conducted, and the results of current and power output against time and temperature have been presented. From the basic investigation of single PEM fuel cells under different hydrogen flow rate and different load, cold starts of single PEM fuel cells at temperatures above and below -5°C have been conducted. It was found that above temperature of -5°C , the single PEM fuel cell would generate enough heat to keep the water from freezing, and the liquid residual water would be easily brought out of the fuel cell

with the air flow on the cathode side. When the temperature dropped below -5°C , ice/frost would form inside the single PEM fuel cell, which led to the failure of cold start. If the air flow was not stopped, the single PEM fuel cell would have a restart once the protonic conduction and active reaction area have been reestablished. However, the secondary restart would be not able to start the single PEM fuel cell successfully unless external heating would be supplied to operate the single PEM fuel cell at a temperature below -5°C . The following simulation work confirmed the conclusion of the experiments and supplied the information of current density to demonstrate the current density changes at the temperature of -5°C and of -10°C .

Acknowledgment

The authors would like to acknowledge the financial support from The University of Toledo through the startup funding and the 2008 fall senior design group.

References

- [1] "Fuel cells for transportation, energy efficiency and renewable energy," U.S Department of Energy, <http://www1.eere.energy.gov/hydrogenandfuelcells/fuelcells/transportation.html>.
- [2] K. Bullis, "GM's new fuel-cell car," *Technology Review*, April 2007.
- [3] "Honda begins leasing FCX clarity fuel cell vehicle in Japan," *Automobile*, November 2008.
- [4] "Nissan starts vehicle testing of new fuel-cell technology," Nissan, February 2009.
- [5] Y. Hishinuma, T. Chikahisa, F. Kagami, and T. Ogawa, "The design and performance of a PEFC at a temperature below freezing," *JSME International Journal Series B*, vol. 47, no. 2, pp. 235–241, 2004.
- [6] M. Oszcipok, M. Zedda, D. Riemann, and D. Geckeler, "Low temperature operation and influence parameters on the cold start ability of portable PEMFCs," *Journal of Power Sources*, vol. 154, no. 2, pp. 404–411, 2006.
- [7] S. Um and C. Y. Wang, "Computational study of water transport in proton exchange membrane fuel cells," *Journal of Power Sources*, vol. 156, pp. 211–223, 2006.
- [8] C. Bao, M. Ouyang, and B. Yi, "Analysis of the water and thermal management in proton exchange membrane fuel cell systems," *International Journal of Hydrogen Energy*, vol. 31, no. 8, pp. 1040–1057, 2006.
- [9] J. Hou, B. Yi, H. Yu, et al., "Investigation of resided water effects on PEM fuel cell after cold start," *International Journal of Hydrogen Energy*, vol. 32, no. 17, pp. 4503–4509, 2007.
- [10] E. Pinton, Y. Fourneron, S. Rosini, and L. Antoni, "Experimental and theoretical investigations on a proton exchange membrane fuel cell starting up at subzero temperatures," *Journal of Power Sources*, vol. 186, no. 1, pp. 80–88, 2009.
- [11] Y. M. Ferng, Y. C. Tzang, B. S. Pei, C. C. Sun, and A. Su, "Analytical and experimental investigations of a proton exchange membrane fuel cell," *International Journal of Hydrogen Energy*, vol. 29, no. 4, pp. 381–391, 2004.
- [12] N. P. Siegel, M. W. Ellis, D. J. Nelson, and M. R. von Spakovsky, "A two-dimensional computational model of a PEMFC with liquid water transport," *Journal of Power Sources*, vol. 128, no. 2, pp. 173–184, 2004.
- [13] Z. Zhang, X. Wang, X. Zhang, and L. Jia, "Optimizing the performance of a single PEM fuel cell," *Journal of Fuel Cell Science and Technology*, vol. 5, no. 3, Article ID 031007, 9 pages, 2008.
- [14] R. Krishna and J. A. Wesselingh, "The Maxwell-Stefan approach to mass transfer," *Chemical Engineering Science*, vol. 52, no. 6, pp. 861–911, 1997.
- [15] Comsol, *3.4 User Guide*, Comsol AB Inc., 2007.

Research Article

Mesoscopic Modeling of Multiphysicochemical Transport Phenomena in Porous Media

Qinjun Kang, Moran Wang, Partha P. Mukherjee, and Peter C. Lichtner

*Computational Earth Science Group, Earth and Environmental Sciences Division,
Los Alamos National Laboratory, Los Alamos, NM 87545, USA*

Correspondence should be addressed to Moran Wang, mwang@lanl.gov

Received 6 October 2009; Accepted 11 December 2009

Academic Editor: Chen Li

Copyright © 2010 Qinjun Kang et al. This is an open access article distributed under the Creative Commons Attribution License, which permits unrestricted use, distribution, and reproduction in any medium, provided the original work is properly cited.

We present our recent progress on mesoscopic modeling of multiphysicochemical transport phenomena in porous media based on the lattice Boltzmann method. Simulation examples include injection of CO₂-saturated brine into a limestone rock, two-phase behavior and flooding phenomena in polymer electrolyte fuel cells, and electroosmosis in homogeneously charged porous media. It is shown that the lattice Boltzmann method can account for multiple, coupled physicochemical processes in these systems and can shed some light on the underlying physics occurring at the fundamental scale. Therefore, it can be a potential powerful numerical tool to analyze multiphysicochemical processes in various energy, earth, and environmental systems.

1. Introduction

Multiphysicochemical transport phenomena in porous media are ubiquitous, particularly in various energy, earth, and environment systems. One example is the disposal of supercritical CO₂ in geologic formations, the most promising near-term solution to the problem of reducing carbon emissions into the atmosphere [1]. Experimental analyses of the long-term fate of CO₂ after injection into the geologic formations are not possible with relatively short-term laboratory experiments. Therefore it is necessary to employ comprehensive numerical models that incorporate multiple physicochemical processes involving interactions between the injected CO₂, the brine in the pore spaces, and the minerals lining the pores. Supercritical CO₂, as a buoyant and slightly miscible fluid, once injected, displaces brine from the pore space in a complex pattern. At the interface with brine, CO₂ dissolves into the brine to form carbonic acid that can react with and dissolve minerals eventually leading to mineral precipitation further along the flow path. Clearly, there are multiple physics processes involved, including hydrodynamics, thermodynamics, chemical dynamics, and electrostatics (because the surface of most natural media is charged). All these processes are ultimately governed

by pore-scale interfacial phenomena, which occur at scales of microns. However, because of the wide disparity in scales ranging from pore to field, a continuum formulation based on spatial averages taken over length scales much larger than typical pore and mineral grain sizes is often utilized, implying the existence of a representative elemental volume (REV) [2]. As a result, spatial heterogeneities at smaller scales are unresolved and the aggregate effects of the pore-scale (mesoscopic scale) processes are taken into account through various effective constitutive parameters. One of the goals of performing pore-scale simulations is to obtain values for these constitutive parameters through upscaling the pore-scale results. Other goals are to identify key parameters and physicochemical processes that control macroscopic phenomena, and to validate continuum descriptions.

Another example is fuel cells, and in particular polymer electrolyte fuel cells (PEFCs). In PEFCs, the catalyst layer (CL) is the host to several competing transport mechanisms involving charge (proton and electron), species (oxygen, nitrogen, and water vapor), and liquid water transport. The multi-faceted functionality of a gas diffusion layer (GDL) includes reactant distribution, liquid water transport, electron transport, heat conduction, and mechanical support to the membrane-electrode-assembly. Despite tremendous

recent progress in enhancing the overall cell performance, a pivotal performance limitation in PEFCs is manifested in terms of mass transport loss originating from suboptimal liquid water transport and resulting flooding in the constituent components [3]. In recent years, several macroscopic computational models for multiple-physicochemical transport processes in PEFCs [4–10] have been developed. These macroscopic models again are based on the theory of volume averaging and treat the catalyst layer and gas diffusion layer as macrohomogeneous porous layers. Due to their macroscopic nature, the current models fail to resolve the influence of the structural morphology of the CL and GDL on the underlying physics. Mesoscopic modeling is critical to understanding of the overall structure-wettability-transport interactions as well as the underlying multiphysicochemical processes in the CL and GDL, and hence is a useful tool for design and optimization of microstructures of electrodes for better performance and durability.

In this paper, we review our recent work on mesoscopic modeling of multiphysicochemical processes in porous media, based on the lattice Boltzmann method (LBM), a relatively new numerical method for simulating fluid flows and modeling physics in fluids [11]. Originating from the classical statistical physics, LBM is a mesoscopic method based on simplified kinetic equations. In the LBM, the fluid is modeled as a collection of fictitious particles propagating and colliding over a discrete lattice domain. Mesoscopic continuity and momentum equations can be obtained from this propagation-collision dynamics through a rigorous mathematical analysis. The particulate nature and local dynamics provide advantages for complex boundaries and parallel computation. In addition, the kinetic nature of the LBM makes it easy to account for new physics in the LBM framework, which is especially useful for modeling multiphysicochemical phenomena. In Section 2, the partial differential equations governing fluid flow, transport of reactive species and electric potential, as well as mineral reactions in porous media will be given. In Section 3, the implementation of the LBM to solve these governing equations will be presented. Some simulation examples will be given in Section 4 and concluding remarks in Section 5.

2. Governing Equations

Consider the electrolyte fluid flowing through solid porous media. Although the pore scale in this study may be at micrometer scale, the fluid can still be treated as a continuum Newtonian fluid since the characteristic size is much larger than the molecular diameters [12–14].

2.1. Continuity and Momentum Equations. For isothermal incompressible fluid flow, the continuity and momentum equations can be written as [15]

$$\begin{aligned} \nabla \cdot \mathbf{u} &= 0, \\ \rho \frac{\partial \mathbf{u}}{\partial t} + \rho \mathbf{u} \cdot \nabla \mathbf{u} &= -\nabla p + \rho \nu \nabla^2 \mathbf{u} + \mathbf{F}, \end{aligned} \quad (1)$$

where ρ represents the density of the fluid, t the time, \mathbf{u} the velocity vector, p the pressure, ν the kinetic viscosity, and \mathbf{F} the body force density which may include all the effective body forces.

For the hydrodynamic boundary condition, we use the nonslip model at the solid surfaces. The slip boundary conditions have been adopted in some recent studies [16, 17]; however, a careful molecular study showed that the hydrodynamic boundary condition, slip or not, depended on the molecular interactions between fluid and solid and on the channel size [18, 19]. For the flow in porous media considered in this work, the nonslip boundary condition is still valid.

2.2. Transport Equations for Aqueous Species and Electrical Potential. For the i th ion species in the solute, the mass conservation equation describing transport and reaction can be written in the general form [20]

$$\frac{\partial C_i}{\partial t} + \nabla \cdot \mathbf{J}_i + \lambda_i C_i = R_i, \quad (2)$$

where C_i denotes the ionic concentration, \mathbf{J}_i the species flux, λ_i a radioactive decay constant, and R_i the rate at which the i th species is produced or consumed by chemical reactions. The flux \mathbf{J}_i , consisting of contributions from advection, diffusion, and electrochemical migration terms has the form [20]

$$\mathbf{J}_i = -\frac{e z_i D_i}{kT} C_i \nabla \Psi - D_i (\nabla C_i + C_i \nabla \ln \gamma_i) + C_i \mathbf{u}, \quad (3)$$

where the first term on the right refers to electrochemical migration, the second term to aqueous diffusion, and the last term to advective transport. Here z_i , D_i , and γ_i denote the ion algebraic valence, the diffusivity, and the activity coefficient of the i th species, respectively; and e , k , and T denote the absolute charge of electron, the Boltzmann constant, and the absolute temperature, respectively. The quantity Ψ represents the local electrical potential caused by the ionic distribution which is governed by the Poisson equation

$$\nabla \cdot (\epsilon_r \epsilon_0 \nabla \Psi) = -\rho_e = -\sum_i e z_i C_i, \quad (4)$$

where ϵ_r is the local dimensionless fluid dielectric constant, ϵ_0 the permittivity of a vacuum, and ρ_e the net charge density. Assuming no radiation and constant activity coefficient and substituting (4) into (2), we have

$$\frac{\partial C_i}{\partial t} + \mathbf{u} \cdot \nabla C_i = D_i \nabla^2 C_i + \frac{e z_i D_i}{kT} \nabla \cdot (C_i \nabla \Psi). \quad (5)$$

This is the Nernst-Planck equation [21], where \mathbf{F} can be any kind of effective body force. In this contribution we only consider the static electrical force from an external electric field. The general form of electrical force in electrokinetic fluids can be expressed as

$$\mathbf{F}_E = -\rho_e \nabla \Psi_{\text{ext}}, \quad (6)$$

where Ψ_{ext} is the external electrical potential field.

When the ionic convection is negligible and the electric potential is continuously derivable, (5) has a simple steady-state solution for dilute electrolyte solutions:

$$C_i = C_{i,\infty} e^{-e z_i \Psi / kT}. \quad (7)$$

Substituting (7) into (4) yields the nonlinear PB equation [22]

$$\nabla^2 \Psi = -\frac{1}{\epsilon_r \epsilon_0} \sum_i e z_i C_{i,\infty} \exp\left(-\frac{e z_i}{kT} \Psi\right). \quad (8)$$

2.3. Equations for Mineral Reaction Rates. Heterogeneous reactions between aqueous species and minerals at the pore-mineral interface are given by [23]

$$AD \frac{\partial \Psi_j}{\partial n} \Big|_s = \sum_s \nu_{js} A_s \hat{I}_s(s), \quad (9)$$

where n denotes the unit normal perpendicular to the fluid-mineral interface pointing toward the fluid phase, D denotes the aqueous diffusion coefficient assumed to be the same for all species for simplicity, and $\hat{I}_s(s)$ denotes the reaction flux of the s th mineral at its surface, taken as positive for precipitation and negative for dissolution. The total surface area A across which diffusion takes place equal to the sum of individual mineral surface areas A_s is given as

$$A = \sum_s A_s. \quad (10)$$

3. Lattice Boltzmann Model Implementation

3.1. Incompressible Lattice Boltzmann Model for Single-Phase Flow. In order to eliminate compressible effects in the conventional LBM, here we use an incompressible LB model constructed by Guo et al. [24]. The pore-scale flow of a single aqueous fluid phase is simulated by the following evolution equation:

$$f_\alpha(\mathbf{x} + \mathbf{e}_\alpha \delta_t, t + \delta_t) = f_\alpha(\mathbf{x}, t) - \frac{f_\alpha(\mathbf{x}, t) - f_\alpha^{\text{eq}}(\mathbf{x}, t)}{\tau}. \quad (11)$$

In the above equation, δ_t is the time increment, f_α the distribution function along the α direction in velocity space, f_α^{eq} the corresponding equilibrium distribution function, and τ the dimensionless relaxation time. For the commonly used two-dimensional, nine-speed LB model (D2Q9), the discrete velocities \mathbf{e}_α have the following form:

$$\mathbf{e}_\alpha = \begin{cases} (0, 0), & \alpha = 0, \\ (\cos \theta_\alpha, \sin \theta_\alpha)c, & \theta_\alpha = \frac{(\alpha - 1)\pi}{2}, \alpha = 1 - 4, \\ \sqrt{2}(\cos \theta_\alpha, \sin \theta_\alpha)c, & \theta_\alpha = \frac{(\alpha - 5)\pi}{2} + \frac{\pi}{4}, \alpha = 5 - 8. \end{cases} \quad (12)$$

For the incompressible LB model, the equilibrium distribution is defined by Guo et al. [24]:

$$f_\alpha^{\text{eq}} = \begin{cases} -4\sigma \frac{p}{\rho c^2} + s_\alpha(\mathbf{u}), & \alpha = 0, \\ \lambda \frac{p}{\rho c^2} + s_\alpha(\mathbf{u}), & \alpha = 1 - 4, \\ \gamma \frac{p}{\rho c^2} + s_\alpha(\mathbf{u}), & \alpha = 5 - 8, \end{cases} \quad (13)$$

where σ , λ , and γ are the parameters satisfying

$$\begin{aligned} \lambda + \gamma &= \sigma, \\ \lambda + 2\gamma &= \frac{1}{2}, \end{aligned} \quad (14)$$

$$s_\alpha(\mathbf{u}) = \omega_\alpha \left[3 \frac{\mathbf{e}_\alpha \cdot \mathbf{u}}{c^2} + 9 \frac{(\mathbf{e}_\alpha \cdot \mathbf{u})^2}{2c^4} - \frac{3\mathbf{u}^2}{2c^2} \right].$$

In these equations, $c = \delta x / \delta t$, where δx is the space increment, and p and \mathbf{u} are the pressure and velocity of the fluid, respectively. The corresponding weight coefficients are

$$\omega_\alpha = \begin{cases} \frac{4}{9}, & \alpha = 0, \\ \frac{1}{9}, & \alpha = 1 - 4, \\ \frac{1}{36}, & \alpha = 5 - 8. \end{cases} \quad (15)$$

Equation (11) has been shown to recover (1) [24], with the velocity and pressure given by

$$\mathbf{u} = \sum_{\alpha=1}^8 \mathbf{e}_\alpha f_\alpha \quad (16)$$

$$\frac{p}{\rho} = \frac{c^2}{4\sigma} \left[\sum_{\alpha=1}^8 f_\alpha + s_0(\mathbf{u}) \right], \quad (17)$$

respectively.

3.2. Lattice Boltzmann Model for Two-Phase Flow. The interaction-potential model, originally proposed by Shan and Chen [25], and henceforth referred to as the S-C model, introduces k distribution functions for a fluid mixture comprising of k components. Each distribution function represents a fluid component and satisfies the evolution equation. The nonlocal interaction between particles at neighboring lattice sites is included in the kinetics through a set of potentials. The LB equation for the k th component can be written as

$$f_i^k(\mathbf{x} + \mathbf{e}_i \delta_t, t + \delta_t) - f_i^k(\mathbf{x}, t) = -\frac{f_i^k(\mathbf{x}, t) - f_i^{k(\text{eq})}(\mathbf{x}, t)}{\tau_k}, \quad (18)$$

where $f_i^k(\mathbf{x}, t)$ is the number-density distribution function for the k th component in the i th velocity direction at

position \mathbf{x} and time t , and δ_t is the time increment. In the term on the right-hand side, τ_k is the relaxation time of the k th component in lattice unit, and $f_i^{k(\text{eq})}(\mathbf{x}, t)$ is the corresponding equilibrium distribution function.

The phase separation between different fluid phases, the wettability of a particular fluid phase to the solid, and the body force are taken into account by modifying the velocity used to calculate the equilibrium distribution function. An extra component-specific velocity due to interparticle interaction is added on top of a common velocity for each component. Interparticle interaction is realized through the total force, \mathbf{F}_k , acting on the k th component, including fluid/fluid interaction, fluid/solid interaction, and external force. More details can be found in [26, 27].

The continuity and momentum equations can be obtained for the fluid mixture as a single fluid using Chapman-Enskog expansion procedure in the nearly incompressible limit:

$$\begin{aligned} \frac{\partial \rho}{\partial t} + \nabla \cdot (\rho \mathbf{u}) &= 0, \\ \rho \left[\frac{\partial \mathbf{u}}{\partial t} + (\mathbf{u} \cdot \nabla) \mathbf{u} \right] &= -\nabla p + \nabla \cdot [\rho \nu (\nabla \mathbf{u} + \mathbf{u} \nabla)] + \rho \mathbf{g}, \end{aligned} \quad (19)$$

where the total density and velocity of the fluid mixture are given, respectively, by

$$\begin{aligned} \rho &= \sum_k \rho_k, \\ \rho \mathbf{u} &= \sum_k \rho_k \mathbf{u}_k + \frac{1}{2} \sum_k \mathbf{F}_k \end{aligned} \quad (20)$$

with a nonideal gas equation of state given by [28].

3.3. Lattice Boltzmann Model for Transport of Reactive Solutes. In a previous article, Kang et al. [29] have derived the following LB equation for the total primary species concentrations for chemical systems with reactions written in canonical form:

$$\begin{aligned} G_{\alpha j}(\mathbf{x} + \mathbf{e}_\alpha \delta_t, t + \delta_t) &= G_{\alpha j}(\mathbf{x}, t) - \frac{G_{\alpha j}(\mathbf{x}, t) - G_{\alpha j}^{\text{eq}}(\Psi_j, \mathbf{u})}{\tau_{\text{aq}}}, \\ &(j = 1, \dots, N_C), \end{aligned} \quad (21)$$

where N_C is the number of primary species, Ψ_j is the total concentration of the j th primary species, $G_{\alpha j}$ is its distribution function along the α direction, $G_{\alpha j}^{\text{eq}}$ is the corresponding equilibrium distribution function, \mathbf{e}_α are velocity vectors, δ_t is the time increment, and τ_{aq} is the dimensionless relaxation time.

It has been shown that the above equation can recover the following pore-scale advection-diffusion equation for Ψ_j [30]:

$$\frac{\partial \Psi_j}{\partial t} + (\mathbf{u} \cdot \nabla) \Psi_j = \nabla \cdot (D \nabla \Psi_j). \quad (22)$$

This equation is the same as (5) except that here the electrochemical migration is neglected. Assuming that the homogeneous reactions are in instantaneous equilibrium, we have the following mass action equation [31, 32]:

$$C_i = (\gamma_i)^{-1} K_i \prod_{j=1}^{N_c} (\gamma_j C_j)^{\nu_{ji}}, \quad (23)$$

where ν_{ji} are the stoichiometric coefficients, K_i is the equilibrium constant of the i th homogeneous reaction, γ_i is the activity coefficient of the i th secondary species, and C_j and C_i are solute concentrations for primary and secondary species, respectively. They are related by

$$\Psi_j = C_j + \sum_{i=1}^{N_R} \nu_{ji} C_i, \quad (24)$$

where N_R is the number of independent homogeneous reactions, or, equivalently, secondary species.

More details on the heterogeneous reactions between aqueous species and minerals at the pore-mineral interface described by (9), and on the update of solid phase, can be found in [29, 33].

3.4. Lattice Poisson Method. To solve the Poisson equation with strong nonlinearity, (8), we adopt the lattice Poisson method (LPM) developed previously [34, 35], which tracks the electrical potential distribution transporting on the discrete lattices. By expanding (8) into the time-dependent form

$$\frac{\partial \psi}{\partial t} = \nabla^2 \psi + g_{\text{rhs}}(\mathbf{r}, \psi, t) \quad (25)$$

with $g_{\text{rhs}} = (1/\epsilon \epsilon_0) \sum_i z_i e n_{i,\infty} \exp(-z_i e/k_b T) \psi$ representing the *negative* right-hand side (RHS) term of the original (8), we get the discrete evolution equation for the electrical potential distribution

$$\begin{aligned} g_\alpha(\mathbf{r} + \Delta \mathbf{r}, t + \delta_{t,g}) - g_\alpha(\mathbf{r}, t) &= -\frac{1}{\tau_g} [g_\alpha(\mathbf{r}, t) - g_\alpha^{\text{eq}}(\mathbf{r}, t)] + \left(1 - \frac{0.5}{\tau_g}\right) \delta_{t,g} \omega_\alpha g_{\text{rhs}}, \end{aligned} \quad (26)$$

where g_α^{eq} is the equilibrium distribution of the electric potential evolution variable. The time step for the electrical potential evolution is

$$\delta_{t,g} = \frac{\delta_x}{c'}, \quad (27)$$

where c' is a *pseudo*-sound speed in the potential field. After evolving on the discrete lattices, the mesoscopic electrical potential can be calculated using

$$\psi = \sum_\alpha (g_\alpha + 0.5 \delta_{t,g} g_{\text{rhs}} \omega_\alpha). \quad (28)$$

Although the electrical potential evolution equations are in an unsteady form, only the steady state result is

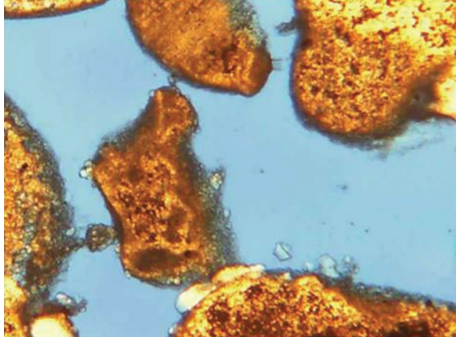


FIGURE 1: Photographic image of a limestone rock thin section (640 × 480 pixels).

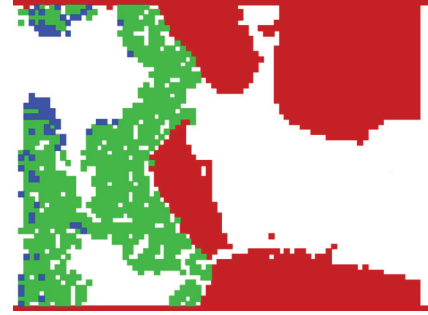


FIGURE 2: Digitized image with reduced resolution.

realistic, because the electromagnetic susceptibility has not been considered. Although the lattice evolution method for nonlinear Poisson equation is not as efficient as the multi-grid solutions due to its long wavelength limit, it has the advantages of suitability for geometrical complexity and parallel computing.

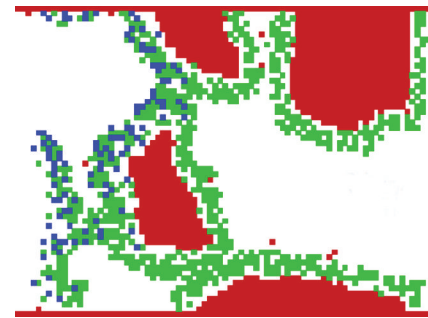
4. Simulation Examples

4.1. Injection of CO₂ into a Limestone Rock. We first present some modeling results on the injection of a fluid saturated with 170 bars CO₂(g) into a limestone rock at the pore scale. The pore structure was derived from a digitized image of a limestone rock thin section with 640 × 480 pixels (Figure 1). We reduced the original resolution to save computational time (Figure 2). The chemical system of Na⁺-Ca²⁺-Mg²⁺-H⁺-SO₄²⁻-Cl⁻-CO₂ with the reaction of calcite to form dolomite and gypsum is considered. Secondary species included in the simulation are OH⁻, HSO₄⁻, H₂SO₄(aq), CO₃²⁻, HCO₃⁻, CaCO₃(aq), CaHCO₃⁺, CaOH⁺, CaSO₄(aq), MgCO₃(aq), MgHCO₃⁺, MgSO₄(aq), MgOH⁺, NaCl(aq), NaHCO₃(aq), and NaOH(aq). Initial fluid composition is pH 7.75 and 2.69 m NaCl brine, equilibrium with minerals calcite, dolomite and gypsum at 25°C. Initial rock composition is calcite. Secondary minerals include dolomite and gypsum. For boundary conditions, a constant pressure gradient is



- Calcite
- Dolomite
- Gypsum

(a)



- Calcite
- Dolomite
- Gypsum

(b)

FIGURE 3: Resulting geometries at time = 15625 seconds for two different mineral reaction rate constants: (a) large reaction rate constants; (b) small reaction rate constants.

imposed across the domain for flow. When flow reaches steady state, a fluid with a pH of 3.87 and in equilibrium with 179 bars CO₂(g) and minerals dolomite and gypsum is introduced at the inlet. Zero gradient boundary conditions are imposed at the outlet. Two different cases are considered with different mineral reaction rates to show their effects on solution concentration, mineral deposition, and change in geometry.

Resulting geometries at time = 15625 seconds for two different mineral reaction rate constants are plotted in Figure 3. Damkohler is 7.375 for calcite and gypsum, 0.7375 for dolomite for the faster mineral reactions, 7.375×10^{-2} for calcite and gypsum, and 7.375×10^{-3} for dolomite for slower reactions. Concentration distribution of total Ca²⁺, Mg²⁺, and SO₄²⁻, pH, and reaction rates for calcite, dolomite, and gypsum for the slower reactions are plotted in Figure 4. As can be seen from the figures, as the reaction rate constants decrease, the deposition of dolomite becomes more uniform surrounding the dissolving calcite grains. Only a small amount of gypsum forms on top of dolomite. At some point in the simulation, the major pores for flow become

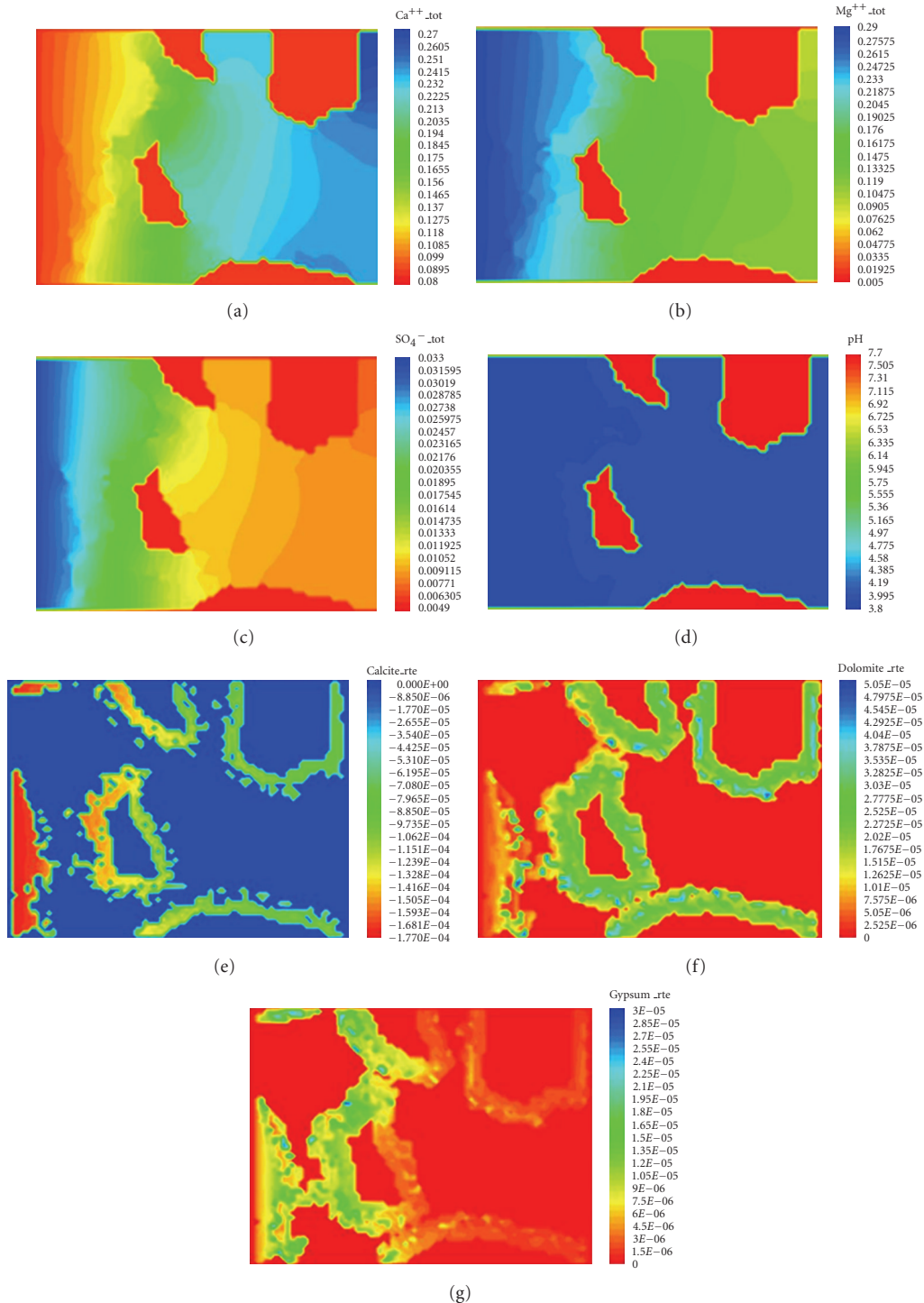


FIGURE 4: Distribution of solute concentrations, pH value, and reaction rates at time = 15625 seconds for small reaction rate constants.

blocked halting further fluid flow through the medium. The pH is uniform over the entire pore space. All reaction rates have finite values at the mineral surface in the whole domain, outlining the solid geometry. The reaction rate is negative for calcite and positive for dolomite and gypsum, confirming that calcite is dissolving while dolomite and gypsum are precipitating.

4.2. Two-Phase Behavior and Flooding Phenomena in Polymer Electrolyte Fuel Cells. In this Section, we present some results for two-phase flow through the porous CL and the fibrous GDL in a PEFC. Details can be found in [36]. Figure 5 displays the steady state invading liquid water fronts corresponding to increasing capillary pressures from the primary drainage simulation in the reconstructed CL microstructure

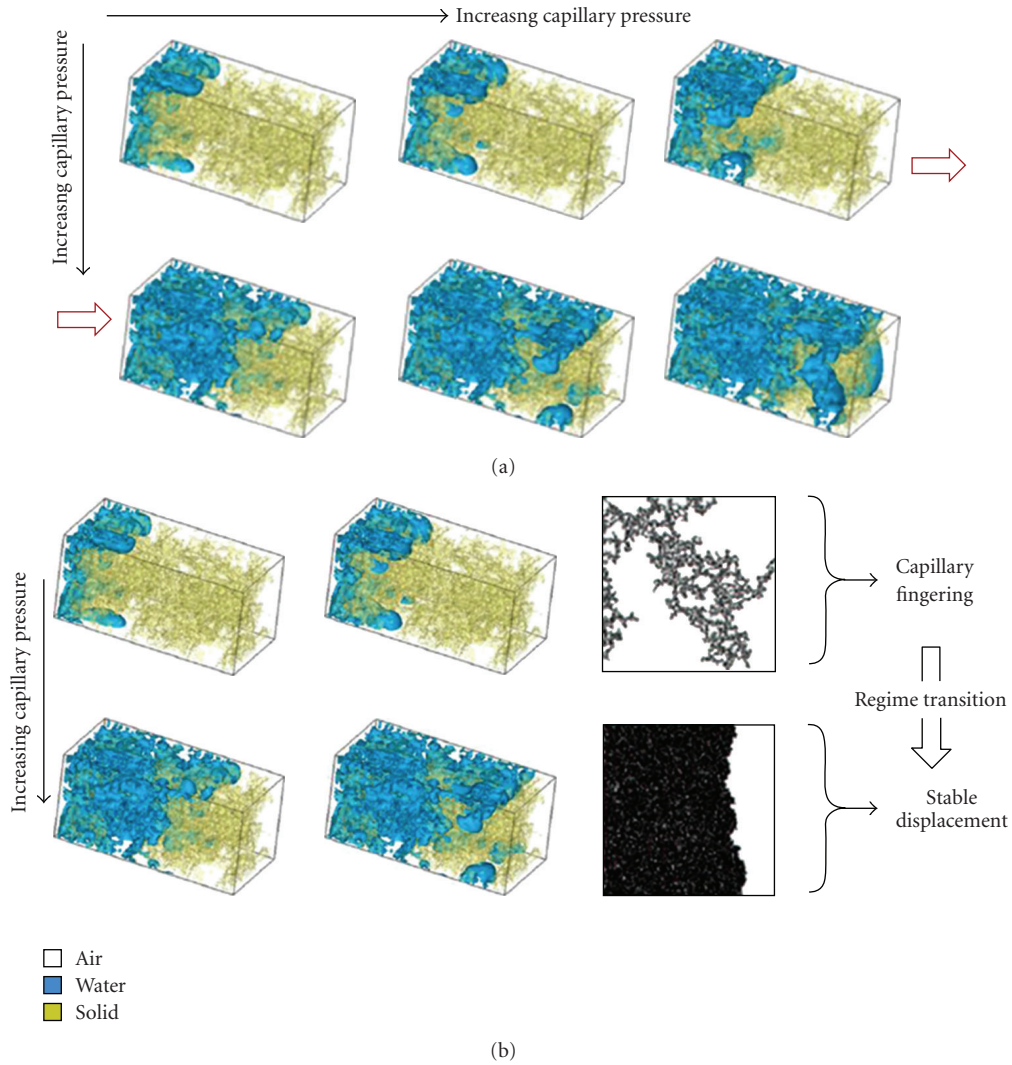


FIGURE 5: Advancing liquid water front with increasing capillary pressure through the initially air-saturated reconstructed CL microstructure from the primary drainage simulation.

characterized by slightly hydrophobic wetting characteristics with a static contact angle of 100° . At lower capillary pressures, the liquid water saturation front exhibits finger like pattern, similar to the displacement pattern observed typically in the capillary fingering regime. The displacing liquid water phase penetrates into the body of the resident wetting phase (i.e., air) in the shape of fingers owing to the surface tension driven capillary force. However, at high saturation levels, the invading nonwetting phase tends to exhibit a somewhat flat advancing front. This observation, as highlighted in Figure 5(b), indicates that with increasing capillary pressure, even at very low capillary number (Ca), several penetrating saturation fronts tend to merge and form a stable front. The invasion pattern transitions from the capillary fingering regime to the stable displacement regime and potentially lies in the transition zone in between. In an operating fuel cell, the resulting liquid water displacement pattern pertaining to the underlying pore-morphology and

wetting characteristics would play a vital role in the transport of the liquid water and hence the overall flooding behavior.

Figure 6 shows the liquid water distribution as well as the invasion pattern from the primary drainage simulation with increasing capillary pressure in the initially air-saturated reconstructed carbon paper GDL characterized by hydrophobic wetting characteristics with a static contact angle of 140° . The reconstructed GDL structure used in the two-phase simulation consists of $100 \times 100 \times 100$ lattice points in order to manage the computational overhead to a reasonable level. Physically, this scenario corresponds to the transport of liquid water generated from the electrochemical reaction in a hydrophobic CL into the otherwise air-occupied GDL in an operating fuel cell. At the initially very low capillary pressure, the invading front overcomes the barrier pressure only at some preferential locations depending upon the pore size along with the emergence of droplets owing to strong hydrophobicity. As the capillary pressure increases,

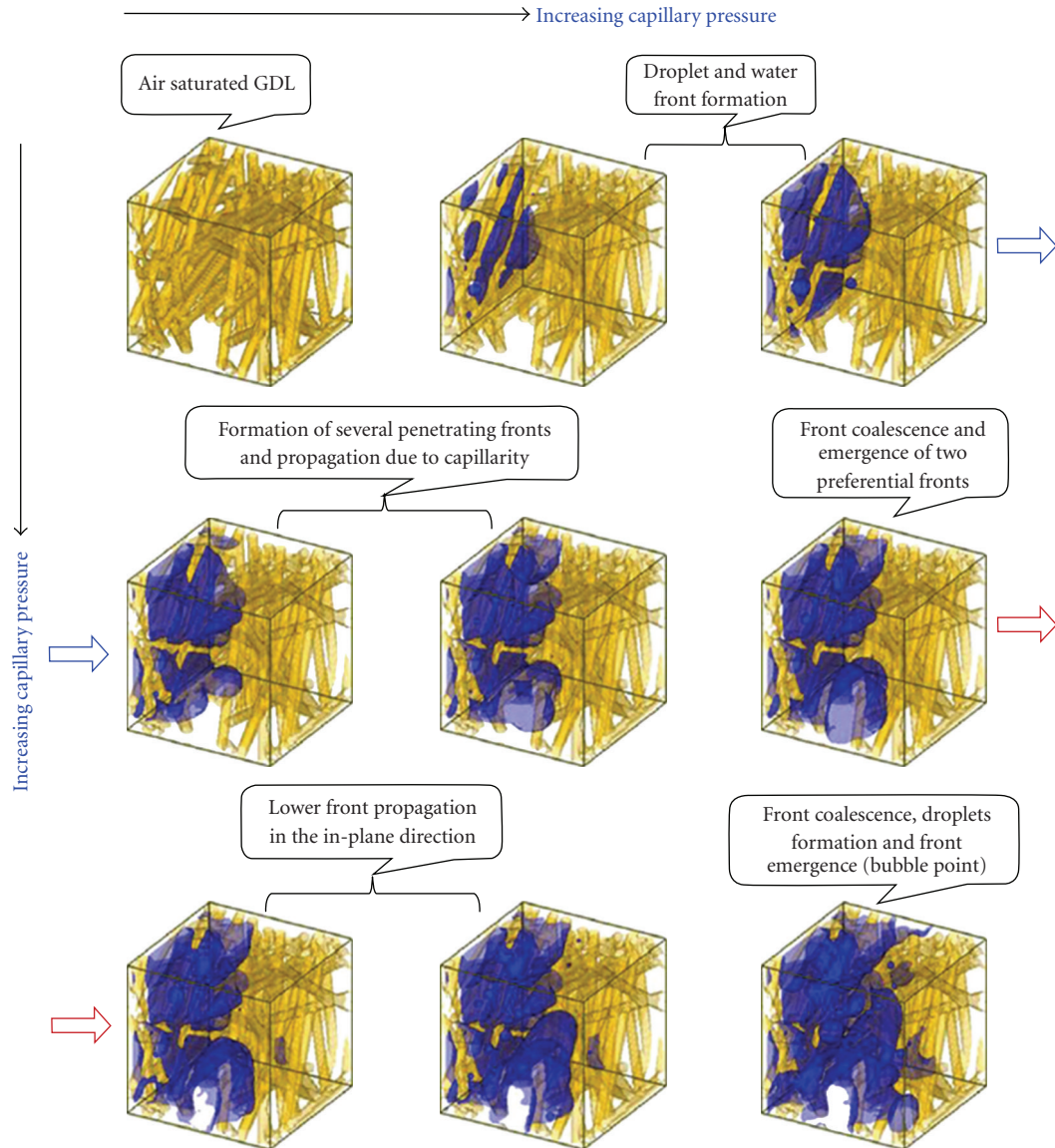


FIGURE 6: Advancing liquid water front with increasing capillary pressure through the initially air-saturated reconstructed GDL micro-structure from the primary drainage simulation.

several liquid water fronts start to penetrate into the air occupied domain. Further increase in capillary pressure exhibits growth of droplets at two invasion fronts, followed by the coalescence of the drops and collapsing into a single front. This newly formed front then invades into the less tortuous in-plane direction. Additionally, emergence of tiny droplets and subsequent growth can be observed in the constricted pores in the vicinity of the inlet region primarily due to strong wall adhesion forces from interactions with highly hydrophobic fibers with the increasing capillary pressure. One of the several invading fronts finally reaches the air reservoir, physically the GDL/channel interface, at a preferential location corresponding to the capillary pressure and is also referred to as the bubble point. It is important to note that the mesoscopic LB simulations provide fundamental insight into the pore-scale liquid water

transport through different GDL structures and would likely enable novel GDL design with better water removal and flooding mitigation.

4.3. Electroosmosis in Homogeneously Charged Micro- and Nanoscale Porous Media. In this section, we briefly present some simulation results on electroosmotic flows (EOFs) in charged micro porous media using the lattice Poisson-Boltzmann method (LPBM), with geometry effects, solution and surface charge effects considered. More details can be found in [35]. We focus on a cubic system of which each side is 1 micron long. A $60 \times 60 \times 60$ uniform grid is used. We change microstructure geometries of porous media by varying the porosity ϵ from 0.1 to 0.9. The average characteristic length of particles varies from 20 to 150 nm. Figure 7 shows Schematics of the generated porous structures for porosity

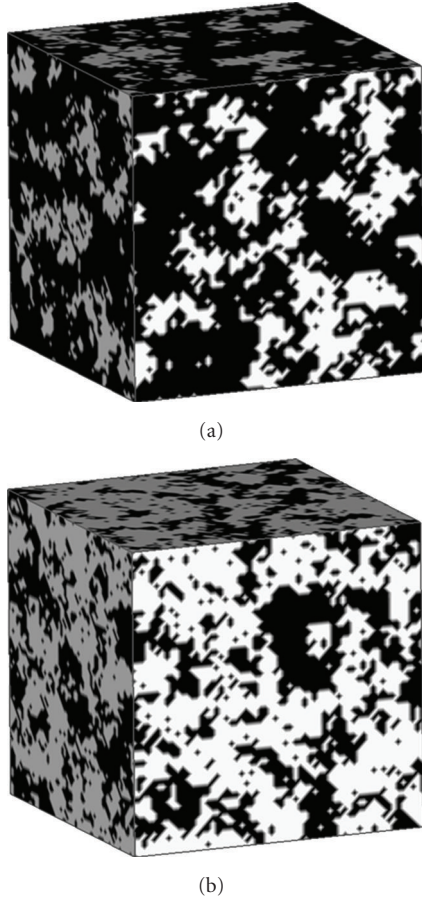


FIGURE 7: Schematics of the generated porous structures on $60 \times 60 \times 60$ grid systems. The white is solid particles and the dark is fluid: (a) porosity = 0.6, (b) porosity = 0.3.

0.3 and 0.6. The bulk ionic concentration n_∞ varies from 10^{-6} to 10^{-3} M and the surface zeta potential from 0 to -100 mV. The other properties and parameters used in this work are the fluid density $\rho = 999.9$ kg/m³, the dielectric constant $\epsilon_r \epsilon_0 = 6.95 \times 10^{-10}$ C²/Jm, the dynamic viscosity $\mu = 0.889$ mPas, the temperature $T = 273$ K and the external electrical field strength $E = 1 \times 10^4$ V/m.

First, the geometry effects on the electroosmotic permeability in micro porous media are investigated by changing volume fraction and particle size (or number density) of the solid phase. We define the electroosmotic permeability, κ_e , as

$$\kappa_e = \frac{\bar{u}}{E}, \quad (29)$$

where \bar{u} is the averaged velocity of EOF along the direction of the driving electrical field \mathbf{E} . The coefficients of electroosmotic permeability (κ_e) for different porosities (ϵ) of porous media are shown in Figure 8. The bulk molar concentration $c_\infty = 10^{-4}$ M, and $\zeta = -50$ mV. The electroosmotic permeability increases with the porosity monotonically. The increasing rate rises with the porosity as well which is very low when the porosity is smaller than 0.5 and becomes sharply high when the porosity is larger

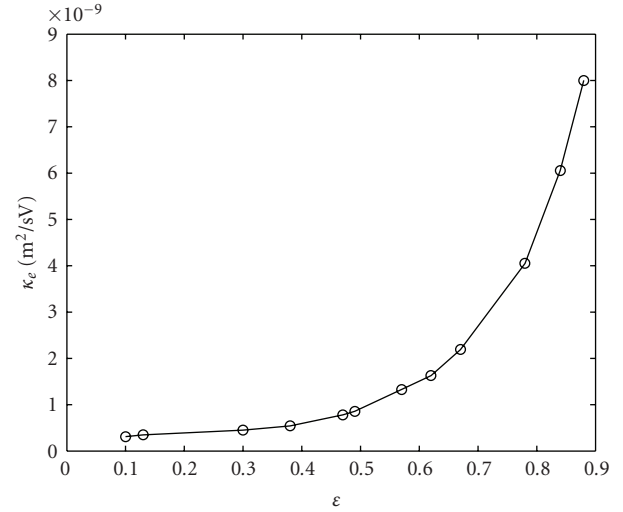


FIGURE 8: Predicted electroosmotic permeabilities for various porosities of porous media at $c_\infty = 10^{-4}$ M, $\zeta = -50$ mV, $E = 1 \times 10^4$ V/m.

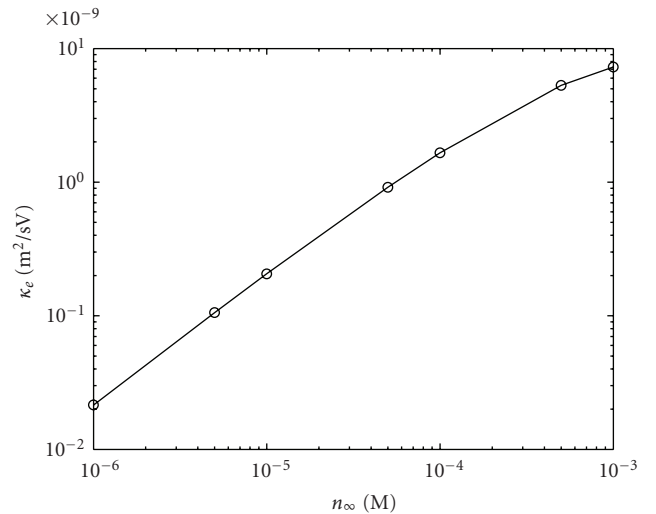


FIGURE 9: The electroosmotic permeability changing with the bulk ionic concentration for $\epsilon = 0.38$, $\zeta = -50$ mV, and $E = 1 \times 10^4$ V/m.

than 0.7. The predicted electroosmotic permeability is in the order of 10^{-9} m²/sV, which is consistent with the existing experimental measurements.

Figure 9 shows the predicted electroosmotic permeability versus the bulk ionic concentration of the electrolyte solution. We used $\epsilon = 0.38$. The electroosmotic permeability κ_e increase monotonically with the bulk ionic concentration c_∞ as c_∞ varies from 10^{-6} to 10^{-3} M. This result can be explained by the undeveloped electrical potential distributions in narrow channels, whose similar results can be found in [37, Figure 2] and [38, Figures 1 and 2]. When c_∞ is lower than 10^{-4} M, the electroosmotic permeability is nearly proportional to the bulk ionic concentration. When c_∞ is higher, the increasing rate becomes a little smaller.

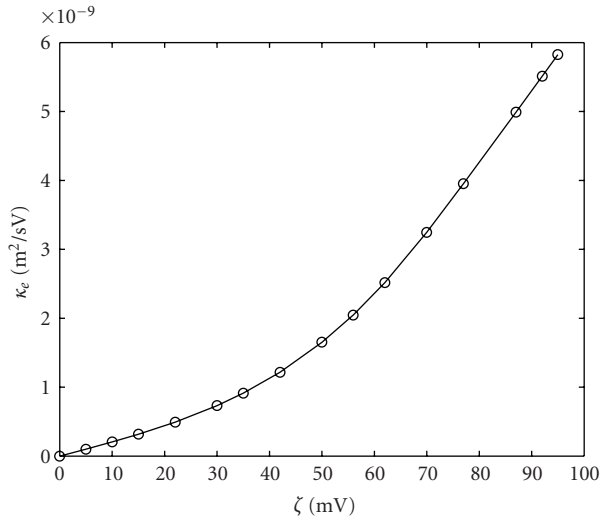


FIGURE 10: The electroosmotic permeability versus the zeta potential for $\epsilon = 0.38$, $c_\infty = 10^{-4}$ M, and $E = 1 \times 10^4$ V/m.

Zeta potential on solid surfaces of porous media affects EOF permeability directly. Simple proportional relationships have been obtained between the electroosmotic permeability and the zeta potential for electrical transports in soils and in polymer composites recently based on the boundary-layer theory. Here we analyze such effects using our numerical methods.

Figure 10 shows the calculated electroosmotic permeability versus the zeta potential on solid surfaces of porous media. All surfaces are homogeneously charged with a same value of ζ . The other parameters used are: $c_\infty = 10^{-4}$ M, $c_d = 0.1$ and $\epsilon = 0.38$. The zeta potential ζ changes from 0 to 90 mV. It shows that the proportionally linear relationship between electroosmotic permeability and zeta potential is accurate only when ζ is very small (<30 mV). The permeability increases much sharper when the zeta potential ζ is larger than 40 mV.

5. Conclusions

We have presented our recent work on mesoscopic modeling of multiphysicochemical processes in porous media, based on the LBM. For the problem of injecting CO_2 saturated brine into a limestone rock, it is shown that the LBM is able to provide detailed information on fluid velocity, solute concentration, mineral composition, and reaction rates, as well as the evolution of the porous media geometry, and therefore can shed some light on the fundamental physics occurring at the pore scale for reactive transport involved in geologic CO_2 sequestration. For two-phase behavior and flooding phenomena in PEFCs, the LBM is a powerful tool to study the influence of the pore structure and surface wettability on liquid water transport and interfacial dynamics in the PEFC catalyst layer and gas diffusion layer. Particularly, the two-phase regime transition phenomenon in the capillary dominated transport in the CL and the influence of the mixed wetting characteristics on the flooding

dynamics in the GDL are demonstrated. For electroosmotic flows in charged porous media, the strongly nonlinear governing equations of electroosmosis in three-dimensional porous media are solved using the LPBM. The effects of pore structure, bulk ionic concentration, and the surface charge on electroosmotic permeability are carefully investigated. It is concluded that the LBM is a powerful numerical tool to simulate multiphysicochemical processes in porous media at the pore-scale.

Acknowledgment

This article is based on research project supported by the National Science Foundation under Grant no. CHE-0431328 and the U.S. Department of Energy, Biological and Environmental Research (BER), and by LDRD projects 20070760PRD4 and 20080727PRD2 sponsored by Los Alamos National Laboratory.

References

- [1] S. Pacala and R. Socolow, "Stabilization wedges: solving the climate problem for the next 50 years with current technologies," *Science*, vol. 305, no. 5686, pp. 968–972, 2004.
- [2] J. Bear, *Dynamics of Fluids in Porous Media*, Elsevier, New York, NY, USA, 1972.
- [3] C.-Y. Wang, "Fundamental models for fuel cell engineering," *Chemical Reviews*, vol. 104, no. 10, pp. 4727–4766, 2004.
- [4] J. J. Baschuk and X. Li, "Modelling of polymer electrolyte membrane fuel cells with variable degrees of water flooding," *Journal of Power Sources*, vol. 86, no. 1, pp. 181–196, 2000.
- [5] L. You and H. Liu, "A two-phase flow and transport model for the cathode of PEM fuel cells," *International Journal of Heat and Mass Transfer*, vol. 45, no. 11, pp. 2277–2287, 2002.
- [6] W. He, J. S. Yi, and T. Van Nguyen, "Two-phase flow model of the cathode of PEM fuel cells using interdigitated flow fields," *AIChE Journal*, vol. 46, no. 10, pp. 2053–2064, 2000.
- [7] J. H. Nam and M. Kaviany, "Effective diffusivity and water-saturation distribution in single- and two-layer PEMFC diffusion medium," *International Journal of Heat and Mass Transfer*, vol. 46, no. 24, pp. 4595–4611, 2003.
- [8] S. Dutta, S. Shimpalee, and J. W. Van Zee, "Numerical prediction of mass-exchange between cathode and anode channels in a PEM fuel cell," *International Journal of Heat and Mass Transfer*, vol. 44, no. 11, pp. 2029–2042, 2001.
- [9] M. Noponen, E. Birgersson, J. Itonen, M. Vynnycky, A. Lundblad, and G. Lindbergh, "A two-phase non-isothermal PEFC model: theory and validation," *Fuel Cells*, vol. 4, no. 4, pp. 365–377, 2004.
- [10] Z. Wang, X. Wu, R. Ni, and Y. Wang, "Binocular fusion in Panum's limiting case of stereopsis obeys the uniqueness constraint," *Science in China, Series C*, vol. 44, no. 1, pp. 40–48, 2001.
- [11] S. Chen and G. D. Doolen, "Lattice boltzmann method for fluid flows," *Annual Review of Fluid Mechanics*, vol. 30, pp. 329–364, 1998.
- [12] M. Wang and S. Chen, "On applicability of Poisson-Boltzmann equation for micro- and nanoscale electroosmotic flows," *Communications in Computational Physics*, vol. 3, no. 5, pp. 1087–1099, 2008.
- [13] M. Wang, J. Liu, and S. Chen, "Similarity of electroosmotic flows in nanochannels," *Molecular Simulation*, vol. 33, no. 3, pp. 239–244, 2007.

- [14] M. Wang, J. Liu, and S. Chen, "Electric potential distribution in nanoscale electroosmosis: from molecules to continuum," *Molecular Simulation*, vol. 33, no. 15, pp. 1273–1277, 2007.
- [15] L. D. Landau and E. M. Lifshitz, *Fluid Mechanics*, Elsevier, New York, NY, USA, 1959.
- [16] C. Davidson and X. Xuan, "Electrokinetic energy conversion in slip nanochannels," *Journal of Power Sources*, vol. 179, no. 1, pp. 297–300, 2008.
- [17] Y. Ren and D. Stein, "Slip-enhanced electrokinetic energy conversion in nanofluidic channels," *Nanotechnology*, vol. 19, no. 19, Article ID 195707, 2008.
- [18] J.-F. Duf r che, V. Marry, N. Mal kova, and P. Turq, "Molecular hydrodynamics for electro-osmosis in clays: from Kubo to Smoluchowski," *Journal of Molecular Liquids*, vol. 118, no. 1–3, pp. 145–153, 2005.
- [19] L. Joly, C. Ybert, E. Trizac, and L. Bocquet, "Hydrodynamics within the electric double layer on slipping surfaces," *Physical Review Letters*, vol. 93, no. 25, Article ID 257805, 4 pages, 2004.
- [20] P. C. Lichtner, "Principles and practice of reactive transport modeling," *Materials Research Society Symposium Proceedings*, vol. 353, no. 1, pp. 117–130, 1995.
- [21] V. G. Levich, *Physico-Chemical Hydrodynamics*, Prentice-Hall, New York, NY, USA, 1962.
- [22] B. Honig and A. Nicholls, "Classical electrostatics in biology and chemistry," *Science*, vol. 268, no. 5214, pp. 1144–1149, 1995.
- [23] P. C. Lichtner and Q. Kang, "Upscaling pore-scale reactive transport equations using a multiscale continuum formulation," *Water Resources Research*, vol. 43, no. 12, Article ID W12S15, 2007.
- [24] Z. Guo, B. Shi, and N. Wang, "Lattice BGK model for incompressible Navier-Stokes equation," *Journal of Computational Physics*, vol. 165, no. 1, pp. 288–306, 2000.
- [25] X. Shan and H. Chen, "Lattice Boltzmann model for simulating flows with multiple phases and components," *Physical Review E*, vol. 47, no. 3, pp. 1815–1819, 1993.
- [26] Q. Kang, D. Zhang, and S. Chen, "Displacement of a two-dimensional immiscible droplet in a channel," *Physics of Fluids*, vol. 14, no. 9, pp. 3203–3214, 2002.
- [27] Q. Kang, D. Zhang, and S. Chen, "Displacement of a three-dimensional immiscible droplet in a duct," *Journal of Fluid Mechanics*, vol. 545, pp. 41–66, 2005.
- [28] X. Shan and G. Doolen, "Diffusion in a multicomponent lattice Boltzmann equation model," *Physical Review E*, vol. 54, no. 4, pp. 3614–3620, 1996.
- [29] Q. Kang, P. C. Lichtner, and D. Zhang, "Lattice Boltzmann pore-scale model for multicomponent reactive transport in porous media," *Journal of Geophysical Research B*, vol. 111, no. 5, Article ID B05203, 2006.
- [30] S. P. Dawson, S. Chen, and G. D. Doolen, "Lattice Boltzmann computations for reaction-diffusion equations," *The Journal of Chemical Physics*, vol. 98, no. 2, pp. 1514–1523, 1993.
- [31] P. C. Lichtner, C. I. Steefel, and E. H. Oelkers, Eds., *Reactive Transport in Porous Media*, vol. 34 of *Reviews in Mineralogy, P. H. Ribbe*, Mineralogical Society of America, Washington, DC, USA, 1996.
- [32] P. C. Lichtner, "Continuum model for simultaneous chemical reactions and mass transport in hydrothermal systems," *Geochimica et Cosmochimica Acta*, vol. 49, no. 3, pp. 779–800, 1985.
- [33] Q. Kang, P. C. Lichtner, and D. Zhang, "An improved lattice Boltzmann model for multicomponent reactive transport in porous media at the pore scale," *Water Resources Research*, vol. 43, no. 12, Article ID W12S14, 2007.
- [34] J. Wang, M. Wang, and Z. Li, "Lattice Poisson-Boltzmann simulations of electro-osmotic flows in microchannels," *Journal of Colloid and Interface Science*, vol. 296, no. 2, pp. 729–736, 2006.
- [35] M. Wang and S. Chen, "Electroosmosis in homogeneously charged micro- and nanoscale random porous media," *Journal of Colloid and Interface Science*, vol. 314, no. 1, pp. 264–273, 2007.
- [36] P. P. Mukherjee, C.-Y. Wang, and Q. Kang, "Mesoscopic modeling of two-phase behavior and flooding phenomena in polymer electrolyte fuel cells," *Electrochimica Acta*, vol. 54, no. 27, pp. 6861–6875, 2009.
- [37] M. Wang, N. Pan, J. Wang, and S. Chen, "Lattice Poisson-Boltzmann simulations of electroosmotic flows in charged anisotropic porous media," *Communications in Computational Physics*, vol. 2, no. 6, pp. 1055–1070, 2007.
- [38] M. Wang, J. Wang, and S. Chen, "Roughness and cavitations effects on electro-osmotic flows in rough microchannels using the lattice Poisson-Boltzmann methods," *Journal of Computational Physics*, vol. 226, no. 1, pp. 836–851, 2007.

Research Article

Experimental Investigations on the Effects of Cerium Oxide Nanoparticle Fuel Additives on Biodiesel

V. Sajith,¹ C. B. Sobhan,¹ and G. P. Peterson²

¹ School of Nano Science and Technology, National Institute of Technology, Calicut 673 601, India

² The George W. Woodruff School of Mechanical Engineering, Georgia Institute of Technology, Atlanta, GA 30332-0325, USA

Correspondence should be addressed to V. Sajith, sajith@nitc.ac.in

Received 5 June 2009; Accepted 6 October 2009

Academic Editor: Moran Wang

Copyright © 2010 V. Sajith et al. This is an open access article distributed under the Creative Commons Attribution License, which permits unrestricted use, distribution, and reproduction in any medium, provided the original work is properly cited.

This paper reports the results of experimental investigations on the influence of the addition of cerium oxide in the nanoparticle form on the major physicochemical properties and the performance of biodiesel. The physicochemical properties of the base fuel and the modified fuel formed by dispersing the catalyst nanoparticles by ultrasonic agitation are measured using ASTM standard test methods. The effects of the additive nanoparticles on the individual fuel properties, the engine performance, and emissions are studied, and the dosing level of the additive is optimized. Comparisons of the performance of the fuel with and without the additive are also presented. The flash point and the viscosity of biodiesel were found to increase with the inclusion of the cerium oxide nanoparticles. The emission levels of hydrocarbon and NO_x are appreciably reduced with the addition of cerium oxide nanoparticles.

1. Introduction and Background

Although diesel engines are generally more efficient than spark ignition engines, emissions from the diesel engine are typically higher. This has resulted in a somewhat negative impact on its wide acceptance and use, especially in automotive applications. Recently, stringent emission legislation has been imposed worldwide on the oxides of nitrogen (NO_x), and smoke and particulate matter emitted from automotive diesel engines. Neeft et al. [1] have reviewed the background of the emission of particulate matters and have suggested several measures for reducing particulate and NO_x emissions, such as optimizing the fuel composition, engine modifications, after-treatment techniques like selective catalytic reduction of NO_x with hydrocarbons and use of particulate traps. The major problem associated with particulate traps is the plugging which calls for periodic regeneration [2, 3].

The various fuel properties which affect particulate emissions such as the volatility, density, and the sulfur content in the fuel can be altered by the use of fuel additives. The fuel injection and mixture preparation processes are strongly

influenced by properties such as the density, volatility, and viscosity, which are often interdependent. The volatility of diesel is represented by the ASTM distillation curve. The viscosity of diesel oil affects the atomization as well as its lubrication characteristics, while the flash and fire points suggest the temperature below which the fuel can be safely handled. The low temperature characteristics of diesel have more significance in relation to fuel handling than its combustion behavior. Therefore, acceptable levels must be found for appropriate physicochemical properties in order to optimize the process of combustion as well as to ensure safe handling of the fuel.

A number of experimental investigations have been reported with a wide variety of metal additives to improve the fuel properties and the engine performance, as well as to reduce emissions. The effect of calcium, barium, iron, and nickel naphthenates have been studied, concluding that calcium and barium most efficiently reduce soot, by both suppressing soot formation and enhancing soot oxidation [4]. Based on experimental investigations, Gürü et al. [5] concluded that manganese, as a fuel additive, has a greater effect in the reduction of the freezing point of the fuel,

than copper, magnesium, or calcium. Emission measurements with manganese as a fuel additive demonstrated that O_2 and CO could be decreased by 0.2% and 14.3%, respectively, SO_2 emission could be reduced, and the overall impact of all these effects was found to lead to an increase of 0.8% in the net operating efficiency.

Valentine et al. [6] experimentally observed that bimetallic platinum and cerium diesel fuel borne catalyst reduces the engine emissions and improves the performance of the diesel particulate filter. Shi et al. [7] reported that the particulate matter emission decreases with increasing oxygenate content in the fuels, but nitrogen oxides emissions increase. De et al. [8] experimentally observed that the presence of ethanol and ethyl ter-butyl ether (ETBE) significantly alters the characteristics of volatility and reduces the Cetane number, impairing the fuel's performance in engine tests. The effect of methanol-containing additive (MCA) on the emission of carbonyl compounds generated from the diesel engine was studied by Chao et al. [9] and it was observed that the emission factors for some of the carbonyl compounds with the use of MCA are higher than the values for those without the use of MCA.

Metal oxides such as those of copper, iron, cerium, and cobalt have been extensively used as fuel additives. The effect of cerium on the size distribution and composition of diesel particulate matter has been studied by Skillas et al. [10], indicating a reduction in the accumulation mode, but an increase in ultrafines. Lahaye et al. [11] studied the effect of cerium oxide on soot formation and postoxidation and observed that the soot yield is not affected significantly by the presence of cerium oxide in the fuel for given oxygen content. Based on experiments, Jung et al. [12] observed that the addition of cerium to diesel fuel causes significant changes in the number concentration of particles in the accumulation mode, light off temperature, and the kinetics of oxidation. Even though the oxidation rate increased significantly with the addition of cerium to the fuel, the dosing level was found not to have much influence [12, 13].

With fossil fuels getting depleted, a number of investigations are being undertaken on alternate fuels like bio diesels derived from various natural sources such as vegetable oils. Use of biodiesel and its modifications has been reported extensively in the literature. It has been reported that single fuel operation with neat *Jatropha* oil in diesel engine resulted in a slightly reduced thermal efficiency, higher HC and CO emissions as compared to diesel [14, 15]. Using a *Jatropha* oil-methanol blend as in place of neat *Jatropha* oil resulted in a slight increase in the brake thermal efficiency, a significant reduction in the exhaust gas temperature and a reduction of HC and CO emissions [16]. Experimental investigations have been reported to evaluate the effect of anticorrosion additive in palm oil-based biodiesel on the engine performance, emissions, and wear characteristics [17].

The present experimental study is aimed at investigating the effect of the use of a fuel additive in the form of cerium oxide nanoparticles on the physicochemical properties of bio diesel, and its influence on the engine performance and emissions. Cerium oxide has the ability to act as oxygen buffer causing simultaneous oxidation of hydrocarbons as

well as the reduction of oxides of nitrogen, thus reducing emissions, especially in the stoichiometric conditions. Metal-doped cerium oxide used in the nanoparticle form is proven to give much better results in efficiency enhancement compared to larger dimension powders. This technique has been evaluated in diesel fuels [18], though extensive parametric studies have not been reported. One of the major reasons for the efficiency improvement is inferred to be the high surface-to-volume ratio of nanoparticles compared to conventional powder form, as catalysis is essentially a surface phenomenon.

As important as the efficiency enhancement are the influences of additives on the emission behavior and the physicochemical properties of the fuel. Cerium oxide nanoparticles could possibly exhibit high catalytic activity because of their large surface area per unit volume, leading to improvement in the fuel efficiency and reduction in the emissions. With this background, extensive investigations on the performance as well as emissions and physicochemical properties of bio diesel with the inclusion of pure cerium oxide in the nanopowder form suspended in the fuel by an ultrasonic shaking process constitute the theme of the present research work. The fuel properties tested in the study include flash and fire points, viscosity, cloud point, and pour point. In order to obtain the performance and emission characteristics, and thus relate between the engine performance and environmental impact to the dosing level of the fuel additive, performance tests were carried out on a single cylinder water-cooled direct injection diesel engine. The performance and emission characteristics of biodiesel, in the pure form and in the presence of various dosing levels of the nanoparticle additives are presented.

2. Experimental Study

The experimental investigations were carried out in two phases. In the first phase, the various physicochemical properties of modified bio diesel were determined and compared with those of the base fuels. The properties studied were the flash and fire points, cloud and pour points and viscosity. Standard ASTM test procedures were used in the experiments. In the second phase, extensive performance tests were conducted on a single cylinder compression ignition engine using the modified and base fuels, in order to evaluate the engine performance as well as the emission characteristics using an exhaust gas emission analyzer. The method of preparation of the fuels with the additive nanoparticles along with the experimental methods for obtaining the fuel properties and the details of the performance test facility are all presented below.

2.1. Preparation of Modified Fuels. The fuel used for the current investigation is a bio diesel product, derived from *Jatropha*. The viscosity, density, and Calorific value of the bio diesel were measured using standard equipment and are 52 cSt at 32°C, 906 kg/m³ and 34.5 MJ/Kg, respectively. The fuel additive used in this investigation is cerium oxide, in the form of commercially available nanoparticles of size 10 to 20

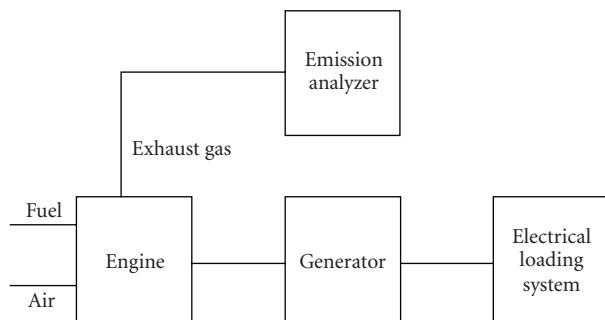


FIGURE 1: Schematic of the experimental set up.

TABLE 1: Engine specifications.

Type	Naturally aspirated, four stroke, single cylinder, water-cooled compression ignition
Stroke	110 mm
Bore	88 mm
Rated output	5.5 kW
Rated speed	1500 RPM
Loading devise	Electrical generator

nanometers and density of 7.13 g/mL. The dosing level of the cerium oxide nanoparticle samples (by weight) in the base fuel was varied from 20 to 80 ppm. The required quantity of the nanoparticle sample required for each dosing level was measured using a precision electronic balance and mixed with the fuel by means of an ultrasonic shaker, applying a constant agitation time of 30 minutes to produce a uniform suspension. The modified fuel was utilized immediately after preparation, in order to avoid any settling or for sedimentation to occur.

2.2. Determination of Fuel Properties. The viscosity, flash and fire points, and the pour and cloud points were measured using standard test methods. The viscosity was measured using the Redwood viscometer [19]. A Cleveland open cup flash and fire point apparatus [20] was used for measuring the flash point, and a standard cloud and pour point apparatus was used for measuring the cloud and pour points [21].

2.3. Description of the Test Engine. A four stroke, single cylinder, water-cooled compression ignition engine was used to conduct the performance and emission studies. Standard constant speed load tests were also performed on the engine. An electrical generator was used for loading the engine. Specifications of the engine used for the performance study are given in Table 1, and a schematic block diagram of the experimental test facility is illustrated in Figure 1.

3. Results and Discussion

The ASTM standard tests to determine various physico-chemical properties of the base fuels (Bio diesel) as well as

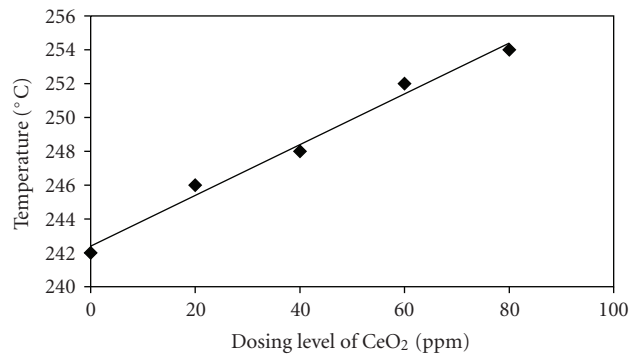


FIGURE 2: Variation of flash point with nanoparticle dosing level for biodiesel.

the modified fuels were carried out under identical laboratory condition so that the results could be compared. The primary objectives of this investigation were to determine the variations in the properties of the fuels, due to the addition of the cerium oxide nanoparticles and to estimate the effect of the level of inclusion of the additives (dosing level) on these variations. Performance tests were conducted on the diesel engine using the modified fuel samples and compared with those with the base fuels, to determine the engine performance enhancement and the reduction of emissions, due to the addition of the catalyst. Based on the experimental results, the variations in the physicochemical properties of the fuel, and the variations in the efficiency and emissions of the CI engine using the modified fuels were determined with various dosing levels as given below. Some indications on the existence of optimum additive nanoparticle dosing levels were also obtained as discussed in this section.

3.1. Fuel Properties. The flash point of the fuel gives an indication of the volatility of a fuel. The lower the volatility, the higher the flash and fire points. Figure 2 shows the variation of the flash point of the bio diesel as a function of the dosing level. As illustrated, the bio diesel shows an increasing trend for the flash point with the dosing level, which indicates a successive decrease in the volatility of the fuel with increases in the quantity of the fuel additive. As illustrated in Figure 2, this increase is nearly linear. Higher flash point temperatures are desirable for safe handling of the fuel. In this context, and because of its higher flash point temperature, the fuels modified with cerium oxide nanoparticles are inherently safer than the base fuels.

The influence of the dosing level of the additive and the temperature on the kinematic viscosity of bio diesel are illustrated in Figure 3, which indicates that the viscosity of the fuel decreases with an increase in the temperature for all dosing levels. Also, it is clear that the maximum percentage variation in the viscosity occurs at the highest temperature. In addition, it is apparent that the nanoparticles added to the fuel increase the fluid layer resistance and hence, increase the viscosity. The change in the viscosity of the fuel affects the engine performance as well as the hydrocarbon emissions. Lower fuel viscosities may not provide sufficient lubrication

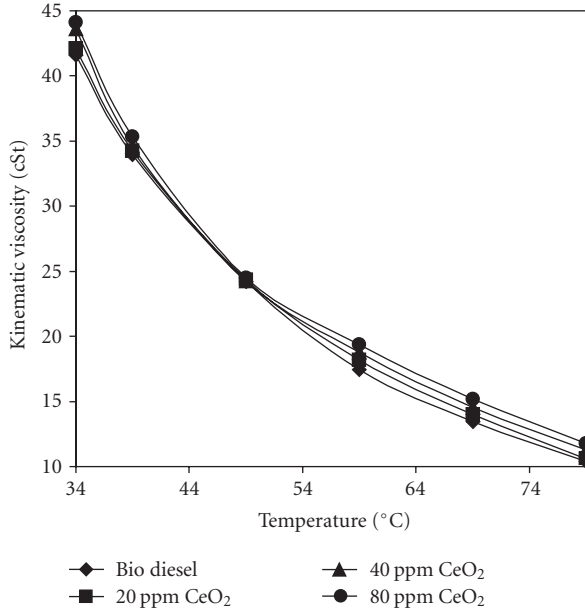


FIGURE 3: Variation of the kinematic viscosity of biodiesel with temperature at different dosing levels of the additive.

TABLE 2: Cloud and pour points of biodiesel.

	Cloud point	Pour point
Biodiesel	6°C	-1°C
Modified biodiesel (dosing level 40 ppm)	6°C	-1°C

of fuel injection pumps or injector plungers resulting in leakage or increased wear thus reducing the maximum fuel delivery. This imposes a limitation on the quantity of the fuel additive that can be used in enhancing the combustion performance of the fuel.

The fuel atomization is affected by the fuel viscosity, and the fuel with higher viscosity tends to form larger droplets on injection, which can cause poor combustion and increased exhaust smoke and emissions. Thus, the selection of the dosing level of the catalyst should be based on a compromise between these two mutually contradicting effects on the performance of the engine.

No significant differences were observed in the cloud and pour points due to the addition of catalyst nanoparticles in the bio diesel, as shown in Table 2 summarizing the measurement of these properties. This indicates that the addition of cerium oxide nanoparticles does not have any significant effect on the cold temperature properties of bio diesel, and no strategic difference is required in the cold handling of the modified fuels.

3.2. Engine Performance. Figure 4 illustrates the results of the performance tests conducted on the diesel engine with standard bio diesel oil and modified fuel. The results show that the brake thermal efficiency of the diesel engine is improved by the addition of cerium oxide in the fuel.

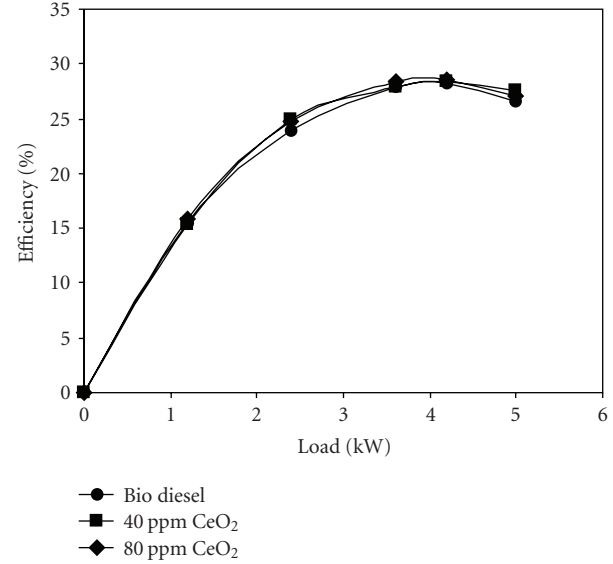
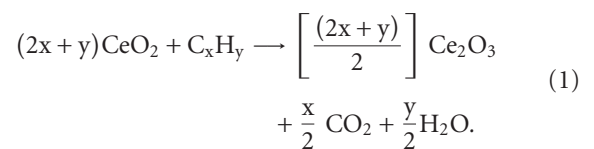


FIGURE 4: Variation of the brake thermal efficiency with load for bio diesel and modified bio diesel with different dosing levels of the additive.

The cerium oxide nanoparticles present in the fuel promote longer and more complete combustion, compared to the base fuel as cerium oxide acts as an oxygen buffer and thus increases the efficiency. It has also been observed that the improvement in the efficiency generally increases with the dosing level of nanoparticles. A maximum increase of 1.5% in the brake thermal efficiency was obtained when the dosing level was varied from 20 to 80 ppm, with a maximum improvement observed at a dosing level of 80 ppm. Cerium oxide oxidizes the carbon deposits from the engine leading to efficient operation and reduced fuel consumption. Corresponding to the efficiency characteristics, the specific fuel consumption decreases with an increase in the dosing level of nanoparticles.

3.3. Emissions. The hydrocarbon emissions have been measured for both the base fuel and the modified fuel using an emission analyzer. Figure 5 shows the variation of hydrocarbon emissions for different dosing levels of the fuel additive in bio diesel. Hydrocarbon emission is found to be significantly reduced on the addition of the additive. Cerium oxide has the ability to undergo a transformation from the stoichiometric CeO_2 (+4) valance state to the Ce_2O_3 (+3) state via a relatively low-energy reaction. Cerium oxide supplies the oxygen for the reduction of the hydrocarbon as well as the soot and gets converted to cerous oxide (Ce_2O_3) as follows [22].

Hydrocarbon combustion:



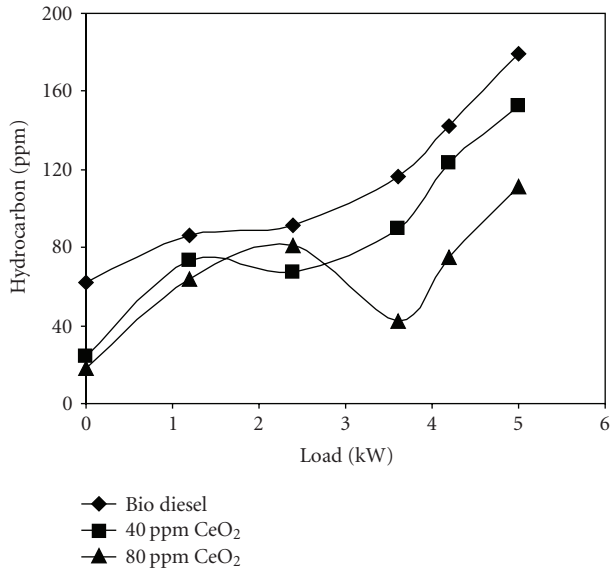


FIGURE 5: Variation of hydrocarbon emission with load for different dosing levels of fuel additive in bio diesel.

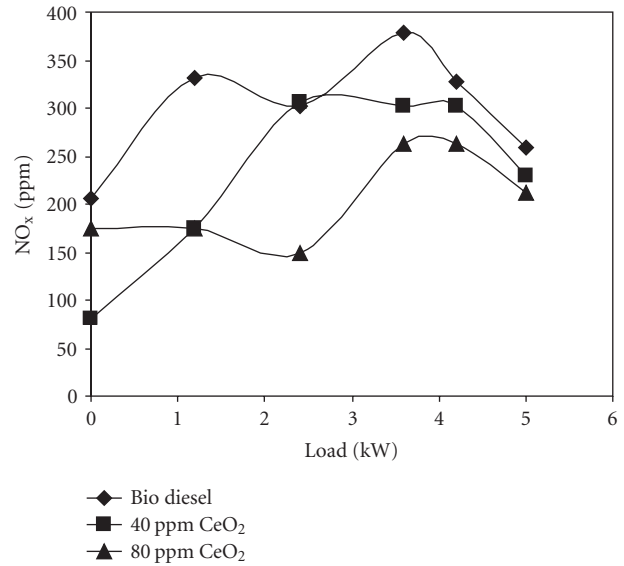
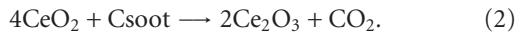


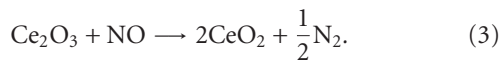
FIGURE 6: Variation of NO_x emissions with load for different additive dosing levels in bio diesel.

Soot burning:



Cerium oxide as an oxidation catalyst also lowers the carbon combustion activation temperature and thus enhances hydrocarbon oxidation, promoting complete combustion. An average reduction of 25% to 40% in the hydrocarbon emissions was obtained for additive dosing levels ranging from 40 to 80 ppm of the additive.

Observation has been made on the level of the NO_x emissions from bio diesel, in the pure form and in the modified form. Due to its high thermal stability, Ce₂O₃ formed from the oxidation of hydrocarbon and soot remains active after enhancing the initial combustion cycle and gets reoxidized to CeO₂ through the reduction of nitrogen oxide as per the following reaction:



It is found that the NO_x emission, as expected, is influenced by the addition of the cerium oxide nanoparticles in bio diesel as shown in Figure 6. The NO_x emission was found to be generally reduced on the addition of cerium oxide nanoparticles to bio diesel, as shown in Figure 6, where an average reduction of around 30% was found to occur with a dosing level of 80 ppm nanoparticles. In general, there is a reduction in NO_x emission due to the addition of cerium oxide. A detailed flame analysis could possibly lead to the exact reasons behind the observed phenomenon, as the behavior could be due to a complex interaction among factors such as the combustion temperature, reaction time, and the oxygen content.

Figure 7 shows the influence of a catalyst addition on carbon monoxide emissions. The reduction influence of

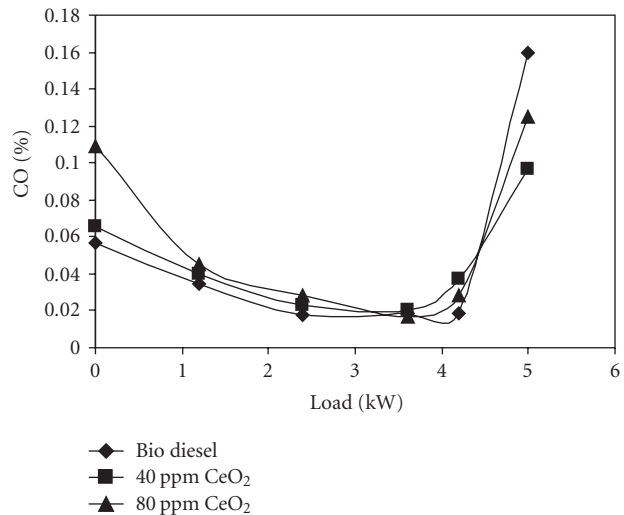


FIGURE 7: Variation of CO emissions with load for different additive dosing levels in bio diesel.

the fuel additive on carbon monoxide emissions is not as prominent as seen in Figure 7.

4. Conclusions

One of the methods to vary the physicochemical properties and combustion characteristics of a hydrocarbon fuel is the use of additives, which are found to be especially effective in nanoparticle form, due to the enhancement of the surface area to volume ratio. ASTM standard tests for the fuel property measurements and engine performance tests were reported in this paper for bio diesel modified by the addition of cerium oxide nanoparticles. Experiments were carried

out at different dosing levels of the nanoparticle additives, to investigate the influences on the physicochemical properties, engine performance, and emissions. The major observations and inferences are listed below.

The flash point of bio diesel, which is an indication of the volatility was found to increase with the inclusion of the additive. The viscosity of bio diesel was found to increase with the addition of cerium oxide nanoparticles. The viscosity and the volatility were found to hold direct relations with the dosing level of the nanoparticles, within the range analyzed (20–80 ppm).

The cold temperature properties of bio diesel do not show significant variation, due to the addition of cerium oxide nanoparticles. Engine tests with the modified bio diesel at different dosing levels (20–80 ppm) of the additive showed an improvement in the efficiency of the engine. Emission levels of hydrocarbon and NO_x are appreciably reduced with the addition of cerium oxide nanoparticles. It is understood that cerium oxide being thermally stable promotes the oxidation of hydrocarbon and reduction of nitrogen oxide, thus acting as an effective catalyst, when added in the nanoparticle form.

Experimental work is underway on the effect of parameters such as the preparation time and the nanoparticle size, apart from the dosing level, on the performance of the fuels modified with cerium oxide nanoparticles. Efforts are also being made to obtain the optimum combinations of these parameters for the best performance of the fuel. Analysis of the combustion and flame characteristics of the catalyst enhanced fuel using visualization techniques is also being undertaken as part of continuing research.

References

- [1] J. P. A. Neeft, M. Makkee, and J. A. Moulijn, "Diesel particulate emission control," *Fuel Processing Technology*, vol. 47, no. 1, pp. 1–69, 1996.
- [2] K. J. Baumgard and D. B. Kittelson, "The influence of a ceramic particle trap on the size distribution of diesel particles," SAE Technical Paper 850009, 1985.
- [3] G. Lepperhoff and G. Kroon, "Impact of particulate traps on the hydrocarbon fraction of diesel particles," SAE Technical Paper 850013, 1985.
- [4] N. Miyamoto, H. Zhixin, A. Harada, H. Ogawa, and T. Murayama, "Characteristics of diesel soot suppression with soluble fuel additives," SAE Technical Paper 871612, 1987.
- [5] M. Gürü, U. Karakaya, D. Altıparmak, and A. Alicilar, "Improvement of Diesel fuel properties by using additives," *Energy Conversion and Management*, vol. 43, no. 8, pp. 1021–1025, 2002.
- [6] J. M. Valentine, J. D. Peter-Hoblyn, and G. K. Acres, "Emissions reduction and improved fuel economy performance from a bimetallic platinum/cerium diesel fuel additive at ultra-low dose rates," SAE Technical Paper 2000-01-1934, 2000.
- [7] X. Shi, Y. Yu, H. He, S. Shuai, J. Wang, and R. Li, "Emission characteristics using methyl soyate—ethanol—diesel fuel blends on a diesel engine," *Fuel*, vol. 84, no. 12–13, pp. 1543–1549, 2005.
- [8] E. W. De Menezes, R. Da Silva, R. Cataluña, and R. J. C. Ortega, "Effect of ethers and ether/ethanol additives on the physicochemical properties of diesel fuel and on engine tests," *Fuel*, vol. 85, no. 5–6, pp. 815–822, 2006.
- [9] H.-R. Chao, T.-C. Lin, M.-R. Chao, F.-H. Chang, C.-I. Huang, and C.-B. Chen, "Effect of methanol-containing additive on the emission of carbonyl compounds from a heavy-duty diesel engine," *Journal of Hazardous Materials B*, vol. 73, no. 1, pp. 39–54, 2000.
- [10] G. Skillas, Z. Qian, U. Baltensperger, U. Matter, and H. Burtscher, "Influence of additives on the size distribution and composition of particles produced by diesel engines," *Combustion Science and Technology*, vol. 154, no. 1, pp. 259–273, 2000.
- [11] J. Lahaye, S. Boehm, P. H. Chambrion, and P. Ehrburger, "Influence of cerium oxide on the formation and oxidation of soot," *Combustion and Flame*, vol. 104, no. 1–2, pp. 199–207, 1996.
- [12] H. Jung, D. B. Kittelson, and M. R. Zachariah, "The influence of a cerium additive on ultrafine diesel particle emissions and kinetics of oxidation," *Combustion and Flame*, vol. 142, no. 3, pp. 276–288, 2005.
- [13] B. Stanmore, J. F. Brilhac, and P. Gilot, "The ignition and combustion of cerium doped diesel soot," SAE Technical Paper 01-0115, 1999.
- [14] K. Pramanik, "Properties and use of jatropha curcas oil and diesel fuel blends in compression ignition engine," *Renewable Energy*, vol. 28, no. 2, pp. 239–248, 2003.
- [15] F. K. Forson, E. K. Oduro, and E. Hammond-Donkoh, "Performance of jatropha oil blends in a diesel engine," *Renewable Energy*, vol. 29, no. 7, pp. 1135–1145, 2004.
- [16] A. Ramesh, B. Nagalingam, and M. Senthil Kumar, "An experimental comparison of methods to use methanol and Jatropha oil in a compression ignition engine," *Biomass and Bioenergy*, vol. 25, no. 3, pp. 309–318, 2003.
- [17] M. A. Kalam and H. H. Masjuki, "Biodiesel from palmoil—an analysis of its properties and potential," *Biomass and Bioenergy*, vol. 23, no. 6, pp. 471–479, 2002.
- [18] G. Wakefield, US patent no. 20050066571, March, 2005.
- [19] ASTM D 445, "Test method for kinematic viscosity of transparent and opaque liquids".
- [20] ASTM D92-05a, "Test method for flash and fire points by cleveland open cup tester".
- [21] ASTM 97-05a, "Test method for pour point of petroleum products".
- [22] T. S. Auckenthaler, *Modelling and control of three-way catalytic converters*, Ph.D. dissertation, Swiss Federal Institute of Technology, Zurich, Switzerland, 2005.

Research Article

Effect of Localized Heating on Three-Dimensional Flat-Plate Oscillating Heat Pipe

S. M. Thompson and H. B. Ma

Department of Mechanical and Aerospace Engineering, University of Missouri—Columbia, Columbia, MO 65211, USA

Correspondence should be addressed to H. B. Ma, mah@missouri.edu

Received 2 October 2009; Accepted 14 December 2009

Academic Editor: Chen Li

Copyright © 2010 S. M. Thompson and H. B. Ma. This is an open access article distributed under the Creative Commons Attribution License, which permits unrestricted use, distribution, and reproduction in any medium, provided the original work is properly cited.

An experimental investigation was conducted, both thermally and visually, on a three-dimensional flat-plate oscillating heat pipe (3D FP-OHP) to characterize its performance under localized heat fluxes while operating in the bottom heating mode and charged with acetone at a filling ratio of 0.73. The cooling area was held constant and three heating areas of 20.16 cm², 11.29 cm², and 1.00 cm² were investigated, respectively. It was found that as the heating area was reduced and higher heat fluxes were imposed, the thermal resistance increased and the amplitude of thermal oscillations in the evaporator increased and became more chaotic. Using neutron radiography, it was observed that fluid oscillations did not occur in outer channels located away from the region of local heating. Although the thermal resistance increased during localized heating, a maximum heat flux of 180 W/cm² was achieved with the average evaporator temperature not exceeding 90°C.

1. Introduction

Due to the ongoing miniaturization of electrical components and the general advancement of technology, the thermal management of high heat fluxes is becoming a pivotal requirement for product development and application. Although conventional, wicked heat pipes have provided adequate thermal solutions for many applications, their functionality at high heat fluxes is hindered by numerous limitations (i.e., form factor, operational limits, etc.). The oscillating heat pipe (OHP), as introduced by Akachi [1], provides a promising alternate solution for high heat flux thermal management. The OHP, a two-phase heat transfer device, typically has no wicking structure and exists either as a closed-loop, serpentine-arranged tube (T-OHP) or an engraved, serpentine-arranged channel on a flat-plate of metal that is sealed—also referred to as the flat-plate oscillating heat pipe (FP-OHP). The inner hydraulic diameter of the pipe (or channel) is made sufficiently small to allow a partially filled working fluid to disperse itself into liquid slugs and vapor plugs via capillary action during operation. The OHP operates when both ends of the tubing/plate thermally

interact with a heat source and a heat sink. The heat exchange occurring at both ends continually disturbs the phase of the internal saturated working fluid, resulting in vapor condensation or liquid evaporation. The continual phase change results in a pressure imbalance along the channels of the OHP, which allows for the quasichaotic displacements of the internal working fluid slugs/plugs.

A typical OHP allows for the working fluid to flow within a single plane. However, this traditional design limits the OHP channel density (channels/unit volume) and hence the thermal resistance of the heat pipe at higher heat fluxes. The effects of varying heating conditions, such as heating area, on an OHP have been previously investigated. Xu et al. [2] considered the effects of heating area while experimentally investigating the thermal performance of two aluminum FP-OHPs. Both FP-OHPs had a width of 5 cm and both were charged with either butane or HFC134a. Heating areas were varied by using square copper heat spreaders that had areas of 9 cm², 16 cm², and 25 cm². The heat pipes were dual cooled by submerging the condensing section in a water bath which created a baseline cooling length of 150 mm. It was found that when the evaporator area of the heat pipe was

reduced from 25 cm² to 9 cm² (64% reduction), the thermal resistance of the heat pipe increased over 340% while at a heat input of 80 W. However, it was found that the reduction in thermal resistance was minimal when the heating area was reduced from 50 × 50 mm to 40 × 40 mm. The maximum heat flux achieved during this investigation was on-the-order of 10 W/cm². Charoensawan and Terdtoon [3] investigated the effects of two heating lengths (150 mm and 50 mm) on horizontal, closed-loop oscillating heat pipes (HCLOHPs) charged with either distilled water or ethanol with a constant condenser length. The heat pipes were tubular, made from copper, and the internal diameter and the number of turns were varied. It was found that the thermal performance of one HCLOHP was enhanced by decreasing the heating length and increasing the average evaporator temperature. Furthermore, it was found that the optimal filling ratio increased as the heating length decreased. Meena et al. [4] explored the effects of varying the evaporator length on the operational limit of an OHP with check valves (CLOHP/CV) with various working fluids at a filling ratio of 50%. The CLOHP/CV was made from copper, had an internal diameter of 1.77 mm, and had a total of 10 turns. The evaporator lengths consisted of 15 cm, 10 cm, and 5 cm on where the condenser length was varied to have the same length as the evaporator. It was found that when the evaporator length increased, the critical heat flux decreased for all investigated working fluids. Wang and Shigefumi [5] investigated the effect of varying the heating and cooling lengths on the optimal performance of an OHP. It was suggested that the heating and cooling lengths should be equal at lower filling ratios, and that utilizing a heating length greater than the cooling length is optimal for higher filling ratios. Zhang and Faghri [6] analytically predicted that the reduction of heating section length on an open-loop, tubular OHP reduces the thermal performance of the heat pipe as a result of decreased fluid movement. Borgmeyer and Ma [7] measured the internal fluid oscillation frequencies and velocities for an operating FP-OHP sealed with an acrylic cover. It was found that the oscillation frequencies and amplitudes generally increased with higher heat fluxes. Yang et al. investigated the applicability of aluminum FP-OHPs filled with ethanol as heat spreaders [8]. They found that the FP-OHPs operated in multiple heating orientations and that the FP-OHP which utilized 2 × 2 mm² channels as opposed to 1 × 1 mm² performed better. It was also found that the average amplitude of thermal oscillations in the evaporator decreased with higher heat inputs.

Although the effect of heating length has been investigated for various OHPs under different experimental parameters, the heat flux levels were relatively low—less than 10 W/cm². Furthermore, no research has been performed to investigate the effect of highly-localized heating, on where not only the evaporator length but also the overall geometry vary. Hence, the current study will explore the functionality of the 3D FP-OHP under high heat fluxes that are applied in a localized manner. The thermal performance will be characterized using parameters such as thermal resistance, the average evaporator temperature, and the amplitude of thermal oscillations. Using the novel capabilities of neutron

radiography, the internal fluid dynamics and void fraction distribution were visualized, and these results will also be presented.

2. Prototype Development

The 3D FP-OHP was designed to manage higher heat fluxes by integrating two layers of channels—allowing more channels to exist per unit volume. In general, the FP-OHP design medium is more advantageous for high heat flux management due to its less-awkward form factor and its ability to spread heat across more OHP channels. The primary consideration for the 3D FP-OHP design, and for any OHP design, was to ensure that the hydraulic diameter of the looped, interior channel was small enough to induce capillary action for the current working fluid. As found by Akachi [1], this critical diameter for a given working fluid is found using

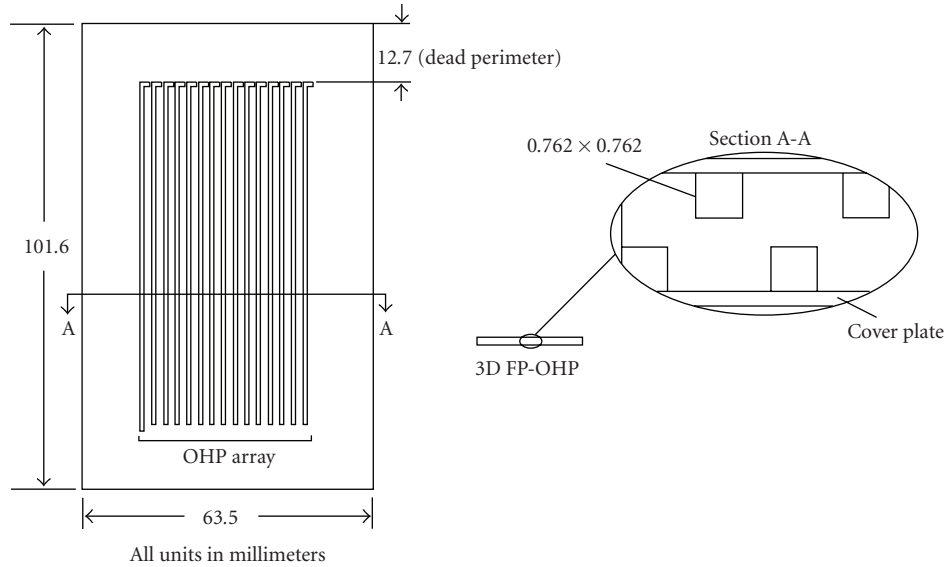
$$D_{\text{crit}} = 2 \sqrt{\frac{\gamma}{g(\rho_l - \rho_v)}} \quad (1)$$

In order to maximize the channel density and minimize the overall dimensions of the device, the hydraulic diameter of the internal channels and channel-to-channel wall thickness was minimized. The current design incorporates a closed-loop, square channel with a hydraulic diameter of 0.762 mm as shown in Figure 1. For the chosen manufacturing process, a “dead perimeter” was implemented which surrounded the internal OHP “channel array” and had a width of 12.70 mm.

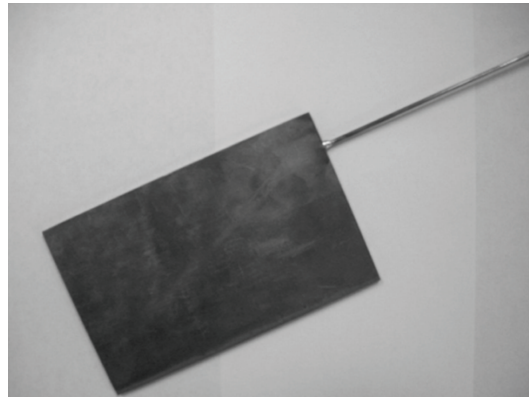
The 3D FP-OHP utilizes two layers of channels on where the OHP array on each layer has 15 turns [9]. The channels are interconnected to each other to form a single closed loop. The working fluid is allowed to flow perpendicularly at the end of each channel through a circular hole (\varnothing 0.762 mm) to begin flow within the second layer on the opposite side—creating an intertwining flow arrangement. The OHP array on each side of the device was designed to be offset from each other to enhance visibility of the working fluid during the visualization experiments that utilized neutron radiography. In accordance with a miniature form factor, the overall thickness of the 3D FP-OHP was minimized and the overall dimensions of the sealed 3D FP-OHP are 101.60 × 63.50 × 2.54 mm³. The 3D FP-OHP was sealed using a brazing process, and the charging tube was soldered on one end of the device. The heat pipe was charged with HPLC-grade acetone at a filling ratio of 73%.

3. Experimental Set-Up

The 3D FP-OHP was tested under various heating areas while holding the cooling area constant and operating in the bottom heating mode. For all experiments, heating and cooling was performed on the same side of the 3D FP-OHP and the charging tube was located in the condenser. The 3D FP-OHP was cooled by using an aluminum cooling block which had dimensions of 76.2 × 76.2 × 20.13 mm³ and allowed for in-series flow via four circular channels with diameters of 15.88 mm. The cooling block was held tightly



(a)



(b)

FIGURE 1: The 3D FP-OHP: (a) overall dimensions and (b) photograph.

against the surface of the 3D FP-OHP and Omegatherm “201” thermal paste was applied between both surfaces to reduce thermal contact resistance. The cooling length was 59 mm which created a cooling area of 37.75 cm². The cooling water temperature was held constant using a Julabo F34 water bath and a centrifugal pump was used to circulate water throughout the system. For the current investigation, two cooling temperatures were used: 20°C and 60°C.

Three heating conditions, that is, cover-plate-mating heating (CPM heating), OHP-array-mating heating (AM heating), and highly-localized, “spot” heating were investigated. CPM heating was accomplished using a copper, rectangular-shaped heating block that had the same width as the 3D FP-OHP and was positioned at the very edge of the heat pipe. During CPM heating, the heating block mated perfectly with the cover plate of the 3D FP-OHP and as a result supplied a heat flux to both the dead perimeter and OHP array sections. AM heating also utilized a copper, rectangular-shaped heating block, but the heating block had the same width as the internal OHP array and was positioned

at the very edge of the OHP array. Hence, the difference in widths between both the CPM and AM heating blocks is twice the length of the dead perimeter. The CPM heating block had dimensions of 63.5 × 31.75 × 19.05 mm³ and had four, 150 W cartridge heaters embedded along the width of it. The AM heating block had dimensions of 44.5 × 25.4 × 6.35 mm³ and had four, 60 W cartridge heaters embedded along the width of it. Thermal paste was applied to the circumferential gaps between the cartridge heaters and the heating block and the rectangular heating blocks were held tightly against the surface of the 3D FP-OHP using clamps. The highly localized spot heating condition was accomplished by band-heating a copper cylindrical rod—on where its ultrasmooth face was tightly clamped against the surface of the 3D FP-OHP using a C-clamp arrangement. The copper rod possessed two sections—each with a different diameter. The major portion of the copper rod had a diameter of 25.40 mm which allowed for a 200 W band heater to be perfectly positioned around it. The other portion of the rod had a diameter of approximately 11.28 mm which allowed for

a 1 cm² heating area. Thermal paste was applied between the copper rod and the 3D FP-OHP surface and Teflon insulation was inserted between the opposite side of the 3D FP-OHP and mouth of the C-clamp. Figure 2 provides an illustration of all three heating conditions investigated. Note that the center-of-heating length, Y_{CH} , is the distance between the edge near the evaporator section and the center of the heating block/rod. All heating blocks/rods were positioned to be centered along the heat pipe's line of symmetry (~ 31.75 mm). It should be noted that the spot heater covered approximately four OHP channels, located on either side of the 3D FP-OHP.

To help summarize the various heating conditions investigated—an area ratio is introduced. The area ratio relates the area of each heat pipe region with the overall heat pipe area, that is,

$$Z_i = \frac{A_{\text{region}}}{A_{\text{hp}}}. \quad (2)$$

Using (2), the area ratios for the evaporator, adiabatic section, and condenser can be found as the heating area ratio, Z_{evap} , the adiabatic area ratio, Z_{adia} , and the condenser area ratio, Z_{cond} , respectively. The heating-to-cooling ratio, $Z_{e/c}$, is defined as

$$Z_{e/c} = \frac{Z_{\text{evap}}}{Z_{\text{cond}}}. \quad (3)$$

All of these heating and cooling parameters for the current investigation are summarized in Table 1.

Thirteen Type-T thermocouples were placed on the opposite, insulated side of the 3D FP-OHP to allow for perfect heating and cooling contact. These thermocouple locations are shown in Figure 3. It should be noted that the thermocouples assigned to describe temperatures in the evaporator varied between spot-heating and rectangular-heating. Table 2 summarizes all of the evaporator and condenser thermocouple designations for each heating condition. Temperature measurements were collected at a sampling rate of 100 Hz using a National Instruments SCXI-1600 data acquisition (DAQ) system and data was imported into a computer utilizing data collection software. Heat input into the heating elements was controlled using a variable autotransformer and digital multimeter (DMM). In order to verify the actual heat input, the average current and voltage across the heating elements were measured using the DAQ system equipped with a shunt resistor set-up. Heat input was increased in a stepwise fashion in increments of 10 W or 20 W, and transient and steady state data collection periods were performed for each heat input. Sufficient time was allowed after each new heat input to allow the heat pipe to thermally respond and reach steady-state. The steady-state data collection periods typically had durations of 3–5 minutes. Experiments ceased when either the maximum evaporator temperature neared 120°C or the maximum capability of the heating element was obtained. Finally, the 3D FP-OHP, equipped with the heating block/rod, cooling block, clamping mechanisms, and thermocouples, was held firmly in position within an aluminum 80/20 holding frame.

Fiberglass insulation was liberally wrapped around the entire set-up to minimize thermal losses to the environment. Figure 4 provides a schematic of the test set-up.

Visual data was collected using real-time neutron imaging at the Center for Neutron Research at the National Institute of Standards and Technology (NIST) [10]. The set-up for visualizing the 3D FP-OHP during the spot-heating condition was similar to test set-ups previously reported [9, 11]. The thermal data collected during the neutron radiography experiments is not presented in the current study.

4. Experimental Results

The steady-state, average temperature difference across the 3D FP-OHP, ΔT_{avg} , for all three heating conditions was determined by subtracting the average condenser temperature from the average evaporator temperature:

$$\Delta T_{\text{avg}} = \left(\frac{1}{N_{\text{evap}}} \sum_{i=1}^{N_{\text{evap}}} T_{\text{avg},i} \right) - \left(\frac{1}{N_{\text{cond}}} \sum_{j=1}^{N_{\text{cond}}} T_{\text{avg},j} \right). \quad (4)$$

Then, for a given heat input, the thermal resistance of the 3D FP-OHP, Ψ_{OHP} , was calculated using

$$\Psi_{\text{OHP}} \cong \frac{\Delta T_{\text{avg},i}}{Q_i}. \quad (5)$$

Figures 5 and 6 show the thermal resistance of the 3D FP-OHP at the various heating conditions for both cooling temperatures and all heating areas. It may be seen that the thermal resistance generally decreases with heat input for all heating conditions and both cooling temperatures and that lower thermal resistances are achieved while using the higher cooling temperature of 60°C. The thermal resistance is higher during the spot heating condition indicating that the thermal performance of the 3D FP-OHP is hindered with the reduction in heating area. Nonetheless, the increase in thermal resistance was only about 40%—indicating that the 3D FP-OHP is very capable of managing these localized heat fluxes. The thermal resistances encountered during both rectangular heating conditions (CPM and AM heating) were nearly the same until, at higher heat fluxes, lower thermal resistances were achieved for AM heating for both cooling temperatures. This provides evidence that the optimal heating area should minimize the contact area with the dead perimeter of the FP-OHP, or that the maximum heating width should be equivalent to the width of the OHP array.

Figures 7 and 8 show the effect of heating area on the average evaporator temperature for the 3D FP-OHP. It was found that the average evaporator temperature increased almost linearly with heat input. At heat inputs over 60 W, the average evaporator temperature was consistently higher during spot heating. For rectangular-heating, the evaporator temperatures were about the same, until at higher heat inputs, AM heating provided lower evaporator temperatures. For a cooling temperature of 20°C, a heat flux of approximately 180 W/cm² was managed by the 3D FP-OHP with the average evaporator temperature not exceeding 90°C.

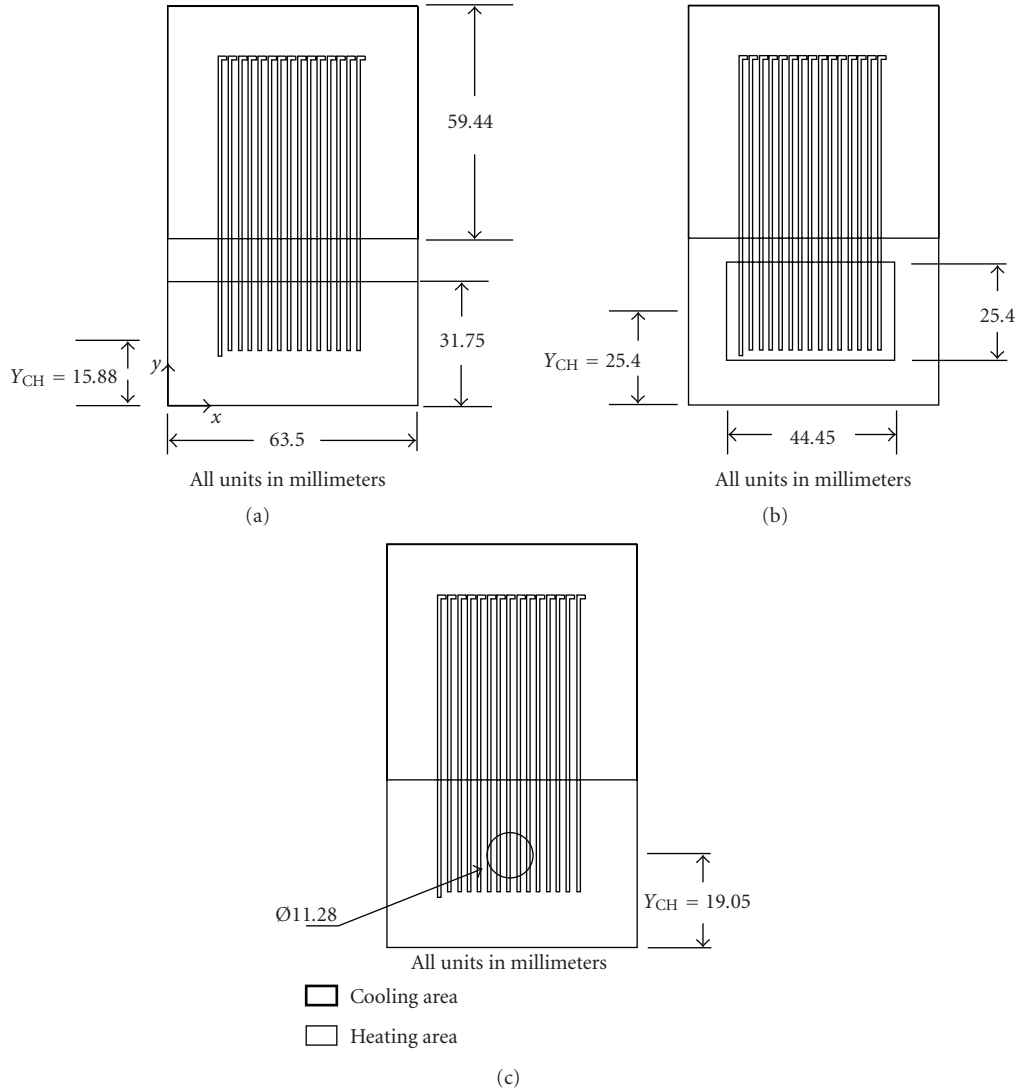


FIGURE 2: Three heating conditions investigated: (a) CPM heating, (b) AM heating, and (c) Spot heating.

TABLE 1: Parameters describing the heating and cooling conditions investigated.

Heating condition	A_{evap} (cm ²)	Y_{CH} (mm)	Z_{evap}	Z_{adia}	Z_{cond}	$Z_{e/c}$
CPM	20.16	15.88	0.313	0.103	0.580	0.539
AM	11.29	25.40	0.175	0.240	0.580	0.302
Spot	1.00	19.05	0.016	0.400	0.580	0.027

In order to understand the effect of heating area on the overall functionality of the 3D FP-OHP, the steady-state temperature, or thermal, oscillations that occurred in both the condenser and evaporator for all heating conditions were observed. Figures 9–11 provide the steady-state thermal oscillations at all thermocouple locations, for all three heating conditions, at a cooling temperature of 20°C, while operating at an average heat input of approximately 160 W. It may be seen from Figures 9 and 10 that during both

AM and CPM heating, thermal oscillations occurred in both the evaporator and condenser with similar amplitudes. In contrast, during spot heating, although temperature oscillations occurred in the condenser and evaporator, they did not occur at locations further away from the center-of-heating location (i.e., T_4 , T_5 , T_6 , and T_8). This is evidenced by observing Figure 11 and seeing that the only condenser temperatures to oscillate strongly were T_{10} and T_{11} —which were both located along the middle of the heat pipe. Knowing

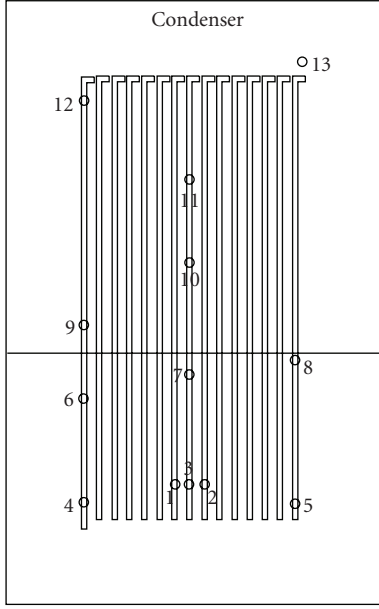


FIGURE 3: Thermocouple locations on one side of 3D FP-OHP.

TABLE 2: Designation of thermocouples for each 3D FP-OHP experiment.

Heating condition	Evaporator thermocouples	Condenser thermocouples
CPM	#1 #2, #3, #4, #5	#9, #10, #11, #12, #13
AM	#1 #2, #3, #4, #5	#9, #10, #11, #12, #13
Spot	#1, #2, #3	#9, #10, #11, #12, #13

that thermal oscillations provide evidence of internal fluid oscillations, it may be concluded that the fluid located in the outer regions of the 3D FP-OHP, away from the point of heating, remained stagnant. This was confirmed during the neutron radiography experiments. Figure 12 provides the standard deviation of a series of neutron images collected during the heat pipe's steady-state operation at 80 W with a cooling temperature of 60°C. This specific image is the result of taking the standard deviation of pixel values for 900 consecutive neutron images (~30 s). Higher standard deviations indicate internal fluid activity and appear as lighter regions, while lower standard deviations indicate constant pixel values and hence a stagnant liquid region.

It may be seen from Figure 12 that during localized heating of the 3D FP-OHP, internal fluid activity occurred within a "bottle-shaped" region that was centered around the heating region on where only a portion of the internal channels participated while the outermost channels remained stagnant. As heat input increased, the width of this bottle-shaped distribution increased slightly while its height decreased. Thermal evidence of the bottle-shaped distribution is evidenced by the weak thermal oscillations of T_4 and T_5 and the lack of thermal oscillations of T_6 and T_8 as shown in Figure 11. The fact that channels located away

from the evaporator were participating indicates the 3D FP-OHP's ability to distribute load of the heat flux and create an "effective" evaporator area.

In order to more accurately compare the thermal oscillations that occurred for each heating condition, the standard deviation of thermal oscillations about the average temperature for each thermocouple location was found by

$$\sigma_{T_i} = \left(\frac{1}{n-1} \sum_{i=1}^n (T_i - T_{\text{avg}})^2 \right)^{1/2} - \bar{\sigma}_{tc}, \quad (6)$$

where n is the number of data points collected for the steady-state collection period. It should be noted that the average standard deviation for a thermocouple in the absence of heat input, or thermocouple "noise" ($\bar{\sigma}_{tc}$), was subtracted from the standard deviation associated with each location. For the current investigation, the recorded thermocouple noise was approximately 0.033°C. Using (6), the average standard deviation of thermal oscillations occurring in both the condenser and evaporator may be found by

$$\bar{\sigma}_{\text{cond}} = \frac{1}{N_{\text{cond}}} \sum_{j=1}^{N_{\text{cond}}} \sigma_{T_j}, \quad (7)$$

$$\bar{\sigma}_{\text{evap}} = \frac{1}{N_{\text{evap}}} \sum_{i=1}^{N_{\text{evap}}} \sigma_{T_i},$$

respectively. The difference between the average standard deviations of thermal oscillations for the evaporator and condenser is then defined by

$$\sigma_{\Delta} = \bar{\sigma}_{\text{evap}} - \bar{\sigma}_{\text{cond}}. \quad (8)$$

Equations (6)–(8) may then be used to measure the "amplitudes" of the thermal oscillations. It was found that the overall amplitude of thermal oscillations increased as the heating area decreased. Furthermore, the regional difference in thermal oscillations, σ_{Δ} , increased with heat input and with the reduction in heating area. This indicates that the amplitude of thermal oscillations is almost always higher in the evaporator than in the condenser. Figure 13 provides the σ_{Δ} for all three heating conditions while at a cooling temperature of 20°C.

It may be seen from Figure 13 that the σ_{Δ} generally increased with heat input and varied with heating area. This indicates that the heating area has a direct effect on the thermal oscillations and hence internal fluid activity. When the heating area was reduced or the heat flux level was increased, the relative fluid activity between heat pipe regions "increased" as indicated by the higher σ_{Δ} values. This demonstrates the 3D FP-OHP's ability to compensate for smaller evaporator areas with stronger fluid motion. Since both the σ_{Δ} and thermal resistance increased when the heating area was reduced, the relationship between the amplitudes of thermal oscillations and the overall thermal performance of the heat pipe was investigated as shown in Figure 14. It was found that as the thermal resistance decreased, the amplitude of thermal oscillations in the

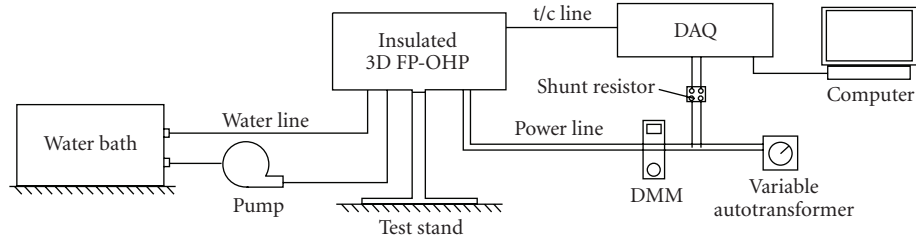


FIGURE 4: Schematic of experimental set-up.

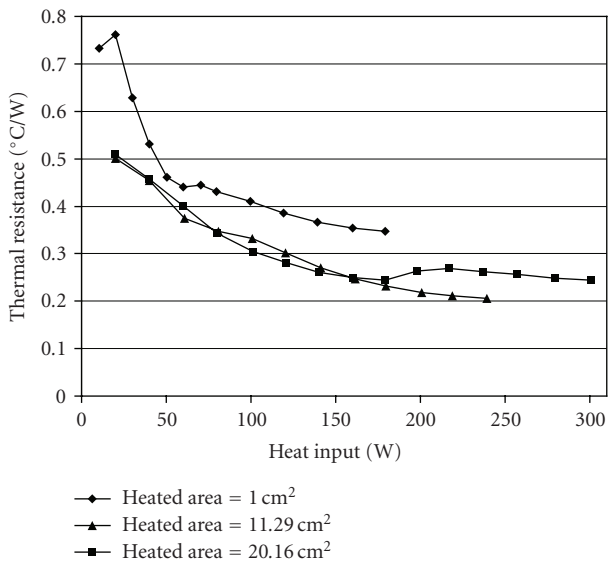


FIGURE 5: Thermal resistance versus heat input at a 20°C cooling temperature.

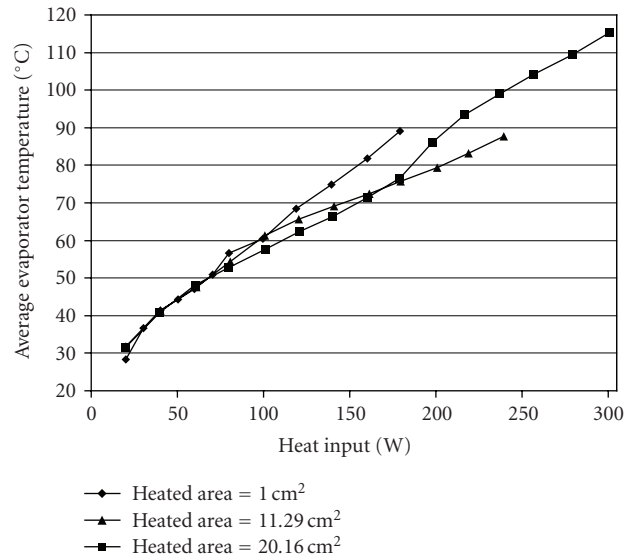


FIGURE 7: Average evaporator temperature versus heat input at a 20°C cooling temperature.

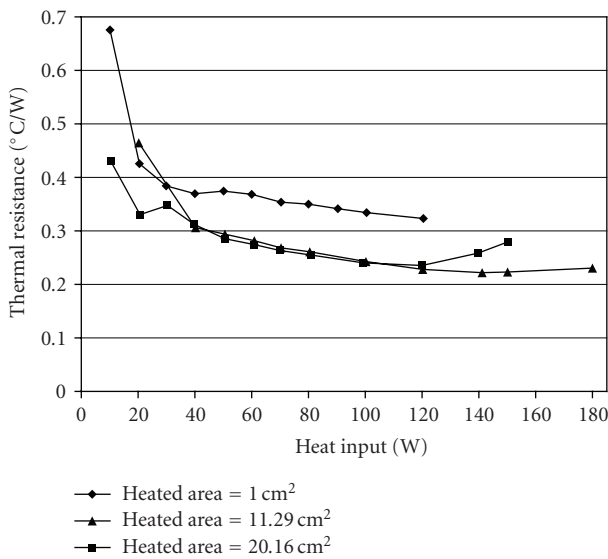


FIGURE 6: Thermal resistance versus heat input at a 60°C cooling temperature.

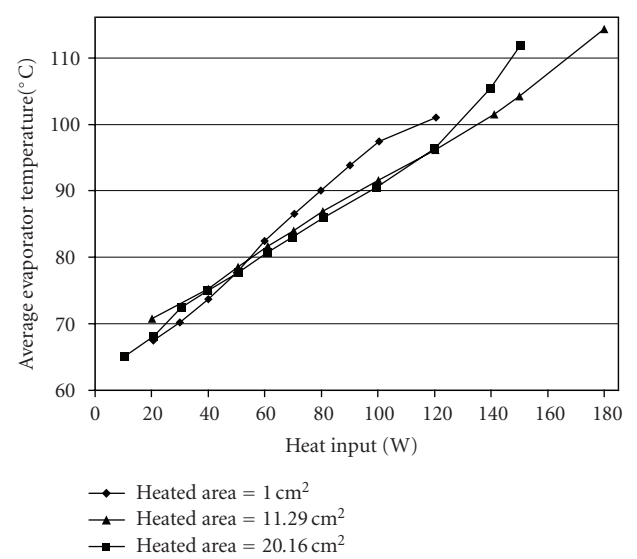


FIGURE 8: Average evaporator temperature versus heat input at a 60°C cooling temperature.

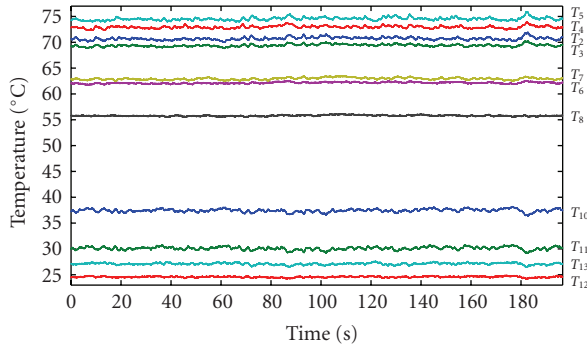


FIGURE 9: Steady-state temperature distribution versus time for CPM heating at 160.15 W at a 20°C cooling temperature.

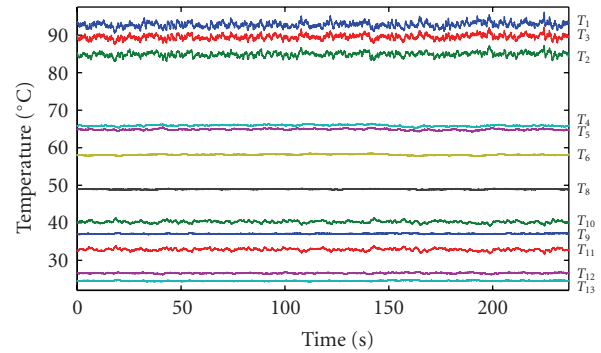


FIGURE 11: Steady-state temperature distribution versus time for spot heating at 160.18 W at a 20°C cooling temperature.

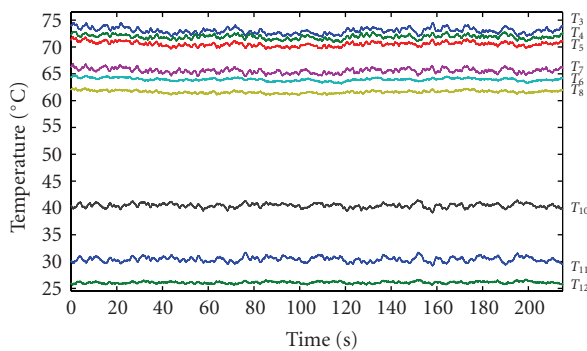


FIGURE 10: Steady-state temperature distribution versus time for AM heating at 161.58 W at a 20°C cooling temperature.

condenser increased. After activation of the 3D FP-OHP, this relationship appears to be linearly correlated. The thermal resistance/amplitude of thermal oscillations plane provides valuable information regarding the thermal-hydrodynamic coupling of the OHP.

5. Conclusions

The 3D FP-OHP performed favorably while being locally heated and was shown to manage heat fluxes over 100 W/cm^2 at cooling temperatures of 20°C and 60°C. At a heat flux of approximately 180 W/cm^2 , the average evaporator temperature did not exceed 90°C at a cooling temperature of 20°C. It was found that while holding the condenser area constant, the reduction in heating area increased the thermal resistance of the 3D FP-OHP. With an area reduction of approximately 90%, the thermal resistance increased approximately 40% for both cooling temperatures. While it was shown that the reduction of the heating area generally decreased the thermal performance of the 3D FP-OHP, the contrary was found at higher heat inputs when a heater that perfectly mated with the width of the internal channel array, as opposed to the overall width of the 3D FP-OHP, was implemented.

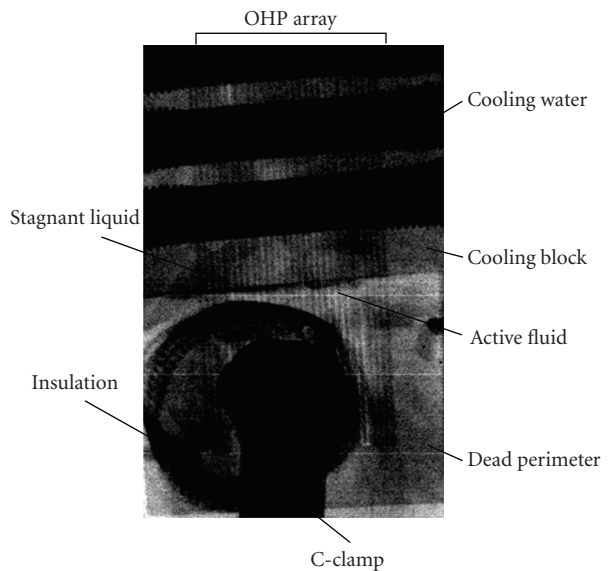


FIGURE 12: Standard deviation of neutron images for 3D FP-OHP at a heat input of 80 W and cooling temperature of 60°C.

Using the average standard deviation of temperature measurements about the respective, local mean temperature, it was found that the amplitude of steady-state thermal oscillations in the evaporator increased with heat input and reduced heating area. In addition, the difference between the amplitudes of thermal oscillations in the evaporator and condenser increased with heat input and reduction in heating area. It was also found that the thermal resistance had an inverse relationship with the amplitude of thermal oscillations in the condenser.

Using neutron radiography, it was found that nonoscillating, stagnant liquid columns existed within channels located on the outer edges of the heat pipe during spot-heating of the 3D FP-OHP and that a bottle-shaped distribution of active fluid was present. Hence, not all interior OHP

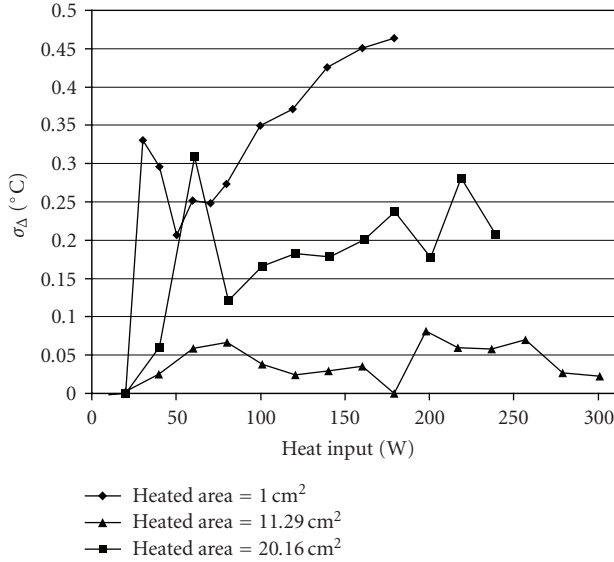


FIGURE 13: Difference in the average, regional standard deviations in thermal oscillations at a cooling temperature of 20°C.

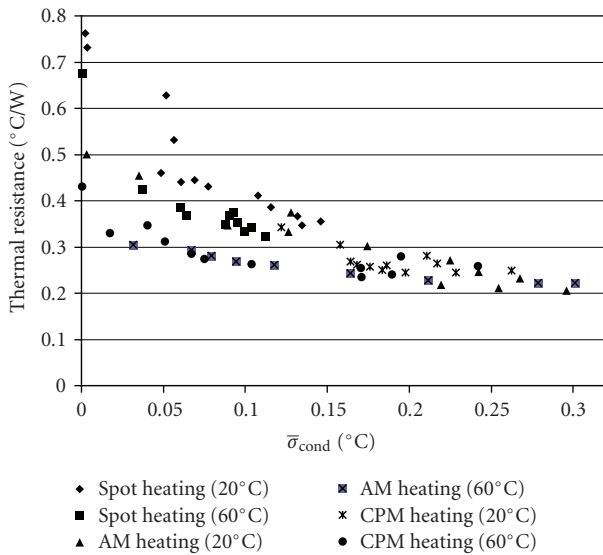


FIGURE 14: Thermal resistance versus average standard deviation for thermal oscillations in the condenser for all heating conditions and cooling temperatures.

channels participated during localized heating, and the 3D FP-OHP functioned on a partial-hydrodynamic basis which resulted in an increase in thermal resistance. Hence, for highly localized heating applications, the FP-OHP’s overall width should be minimized. There may also be a limiting heating area as a result of the number of channels in contact with the heating source. Hence, it is wise to minimize the wall thickness between channels to increase the channel density for high heat flux applications.

Nomenclature

- A: Area, m²
- D: Diameter, m
- g: Gravity, m/s²
- N: Number of thermocouples
- n: Number of steady-state data points collected
- Q: Heat input, W
- T: Temperature, °C
- Y_{CH}: Center-of-heating length, m
- Z: Area ratio.

Greek Symbols

- γ: Surface tension, N/m
- ρ: Density, kg/m³
- Ψ: Thermal resistance, °C/W
- σ̄: Average standard deviation, °C
- σ_Δ: Regional difference in average standard deviations of thermal oscillation, °C.

Subscripts

- adia: Adiabatic
- avg: Average
- cond: Condenser
- crit: Critical
- evap: Evaporator
- e/c: Heating-to-cooling
- hp: Heat pipe
- i: Thermocouple index
- l: Liquid
- OHP: Oscillating heat pipe
- v: Vapor.

Acknowledgments

The work presented in this article was supported by the Office of Naval Research Grant no. N00014-06-1-1119, under the direction of Dr. Mark Spector, and the DARPA TGP program under the direction of Dr. Tom Kenny. The authors acknowledge the support of the National Institute of Standards and Technology, U.S. Department of Commerce, in providing the neutron research facilities used in this work.

References

- [1] H. Akachi, “Structure of a Heat Pipe,” US patent no. 4,921,041, 1990.
- [2] G. Xu, S. Liang, M. Vogel, and T. Katoh, “Thermal characterization of pulsating heat pipes,” in *Proceedings of the 10th Intersociety Conference on Thermal and Thermomechanical Phenomena in Electronics Systems*, pp. 552–556, IEEE, San Diego, Calif, USA, 2006.
- [3] P. Charoensawan and P. Terdtoon, “Thermal performance of horizontal closed-loop oscillating heat pipes,” *Applied Thermal Engineering*, vol. 28, no. 5-6, pp. 460–466, 2008.
- [4] P. Meena, S. Rittidech, and P. Tammasaeng, “Effect of evaporator section lengths and working fluids on operational

- limit of closed loop oscillating heat pipes with check valves (CLOHP/CV),” *American Journal of Applied Sciences*, vol. 6, no. 1, pp. 133–136, 2009.
- [5] S.-F. Wang and N. Shigefumi, “Effect of length ratio of heating section to cooling section on properties of oscillating heat pipe,” *Journal of South China University of Technology*, vol. 35, no. 11, pp. 59–62, 2007.
- [6] Y. Zhang and A. Faghri, “Oscillatory flow in pulsating heat pipes with arbitrary numbers of turns,” *Journal of Thermophysics and Heat Transfer*, vol. 17, no. 3, pp. 340–347, 2003.
- [7] B. Borgmeyer and H. B. Ma, “Experimental investigation of oscillating motions in a flat plate pulsating heat pipe,” *Journal of Thermophysics and Heat Transfer*, vol. 21, no. 2, pp. 405–409, 2007.
- [8] H. Yang, S. Khandekar, and M. Groll, “Performance characteristics of pulsating heat pipes as integral thermal spreaders,” *International Journal of Thermal Sciences*, vol. 48, no. 4, pp. 815–824, 2009.
- [9] S. M. Thompson, H. B. Ma, R. A. Winholtz, and C. Wilson, “Experimental investigation of a miniature three-dimensional flat-plate oscillating heat pipe,” *Journal of Heat Transfer*, vol. 131, no. 4, Article ID 043210, 9 pages, 2009.
- [10] D. S. Hussey, D. L. Jacobson, M. Arif, P. R. Huffman, R. E. Williams, and J. C. Cook, “New neutron imaging facility at the NIST,” *Nuclear Instruments and Methods in Physics Research*, vol. 542, no. 1–3, pp. 9–15, 2005.
- [11] C. Wilson, B. Borgmeyer, R. A. Winholtz, et al., “Visual observation of oscillating heat pipes using neutron radiography,” *Journal of Thermophysics and Heat Transfer*, vol. 22, no. 3, pp. 366–372, 2008.

Research Article

Turbulent Heat Transfer Behavior of Nanofluid in a Circular Tube Heated under Constant Heat Flux

Shuichi Torii

Department of Mechanical System Engineering, Kumamoto University, 2-39-1 Kurokami, Kumamoto 860-8555, Japan

Correspondence should be addressed to Shuichi Torii, torii@mech.kumamoto-u.ac.jp

Received 26 May 2009; Revised 6 July 2009; Accepted 14 September 2009

Academic Editor: Moran Wang

Copyright © 2010 Shuichi Torii. This is an open access article distributed under the Creative Commons Attribution License, which permits unrestricted use, distribution, and reproduction in any medium, provided the original work is properly cited.

The aim of the present study is to disclose the forced convective heat transport phenomenon of nanofluids inside a horizontal circular tube subject to a constant and uniform heat flux at the wall. Consideration is given to the effect of the inclusion of nanoparticles on heat transfer enhancement, thermal conductivity, viscosity, and pressure loss in the turbulent flow region. It is found that (i) heat transfer enhancement is caused by suspending nanoparticles and becomes more pronounced with the increase of the particle volume fraction, (ii) its augmentation is affected by three different nanofluids employed here, and (iii) the presence of particles produces adverse effects on viscosity and pressure loss that also increases with the particle volume fraction.

1. Introduction

In general, the working fluid such as water, oil, and ethylene glycol is used for various industrial fields, namely, power generation and air conditioner. However, those fluids with low thermal conductivity suppress development of compact and higher-performance heat exchangers. Fluid including nanoparticles is referred to as nanofluid, which is a term proposed by Choi [1]. The term “nanofluid” refers to a two-phase mixture with its continuous phase being generally a liquid and the dispersed phase constituted of “nanoparticles,” that is, extremely fine metallic particles of size below 100 nm. In other words, the large surface-area-to-volume ratio also increases the stability of the suspensions. Thus, the nanofluid becomes a new promising heat transfer fluid in a variety of application cases. For example, the thermal properties of such a nanofluid appear to be well above those of the base-fluid and, particularly, the suspended nanoparticles remarkably increase the thermal conductivity of the mixture [2, 3] and improve its capability of energy exchange.

With the nanofluids as the coolant, Lee and Choi [4] proposed that the nanofluids dramatically enhance cooling rates of microchannel heat exchanger compared with the cases of conventional water and liquid-nitrogen coolant. Li and Xuan [5] studied experimentally convective heat transfer performances of nanofluids for laminar and turbulent flow

inside a tube. They disclosed that a remarkable increase in heat transfer performances of nanofluids causes for the same Reynolds numbers. Heat transfer enhancement using copper nanoparticles is also proposed by Xuan and Roetzel [6]. Xuan and Li [7] measured convective heat transfer coefficient of Cu/water nanofluids from 0.3 in volume fraction to 2.0% under constant heat flux condition and reported that the suspended nanoparticles remarkably enhance heat transfer process with smaller volume fraction of nanoparticles. Ding et al. [8] investigated the heat transfer performance of CNT nanofluids in a tube with 4.5 mm inner diameter. They found that the observed enhancement of heat transfer coefficient is much higher than the increase in the effective thermal conductivity.

Meanwhile, there are some inconsistent reports on nanofluid behavior in forced convection. For example, Pak and Cho [9] studied convective heat transfer performance in tube using nanofluids, that is, γ -Al₂O₃ and TiO₂ water and found that for fixed average fluid velocity, the convective heat transfer coefficient of the nanofluids is lower than that of pure water. They postulated that the suspensions have higher viscosity than that of pure water, especially at high particle volume fractions. Using nanofluid including the discshape nanoparticle, Yang et al. [10] measured much lower increase of convective heat transfer coefficient with respect to the effective thermal conductivity and concluded

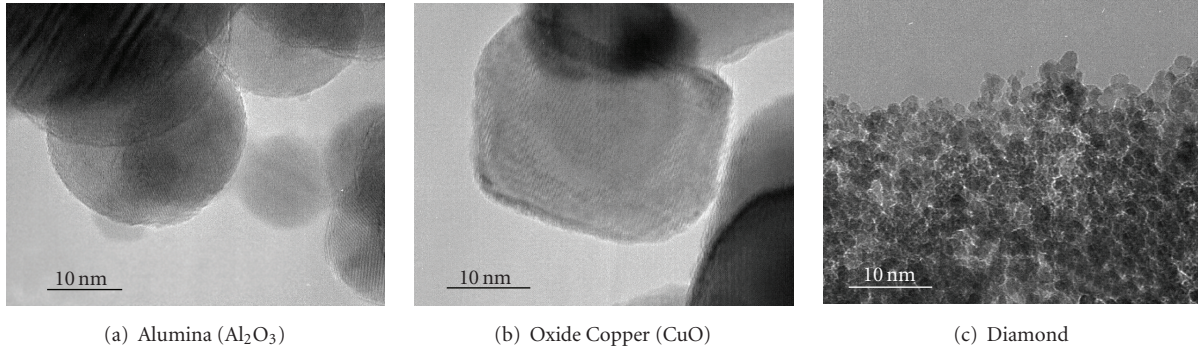


FIGURE 1: TEM images of three different nanoparticles.

TABLE 1: Physical property of nanoparticles.

Nanoparticle	Particle diameter (nm)	Thermal conductivity (W/mk)	Shape
Diamond	2 ~ 10	2000	Sphere
Al ₂ O ₃	33	36	Sphere
CuO	47	20	Polyhedron

that the particle shape or aspect ratio of the particle is a significant parameter to affect the thermal performance of nanofluids.

Throughout the existing reports, Wang and Mujumdar [11] described that (i) the application of nanofluids for heat transfer enhancement should not be decided only by their effective thermal conductivity, and (ii) many other factors such as particle size, shape and distribution, microconvection, pH value, and the particle-fluid interactions should have important influence on the heat transfer performance of the nanofluids.

The purpose of this study is to disclose the thermal fluid flow transport phenomenon of nanofluid in a circular tube by measuring thermal conductivity, effective viscosity, the pressure drop, and the convective heat transfer performance for various concentrations of three different nanofluids. Here aqueous-based nanofluids containing diamond, alumina, and copper oxide, that is, diamond/water, Al₂O₃/water, and CuO/water nanofluids are used as the working fluid and are tested under the constant heat flux boundary.

2. Experimental Apparatus and Measure Method

The nanoparticles used in this study are diamond, alumina (Al₂O₃), and copper oxide in which alumina and copper oxide are the most common and inexpensive nanoparticles used by many researchers in their experimental investigations. Figure 1 shows TEM image of three different nanoparticles and the corresponding physical properties are summarized in Table 1. The diamond nanoparticle has the highest thermal conductivity among three different particles used here, as is seen in Table 1. Deionized water is used as the base liquid. Figure 2 depicts pictures of 1 vol.% nanofluids after 60 days later. Here, 1 vol.% implies a nanofluid of 1% volume fraction of particles. The corresponding pH

for three nanofluids is 6.62, 6.66, and 6.35, respectively. Since no concentration gradient appears in three different nanofluids, the nanofluids employed here maintain stability for several weeks. Figure 3 depicts the relationship between the average particle size and the zeta potential in three different nanofluids measured with the use of ELSZ-2 zeta potential and particle size analyzer (Otsuka Electronics Co., Ltd. Japan). In general, the relationship between zeta potential and average particle size of nanoparticles in suspension implies the particle dispersion state in nanofluid and in other words a large zeta potential corresponds to homogeneous dispersion. Zeta potential of Al₂O₃ is the highest in three different nanofluids, as is seen in Figure 3. One observes that diamond- and CuO-nanofluids form large aggregation, and in particular CuO nanofluids include several micro-order particles in diameter. Small particle has large zeta potential, as expected.

The effective thermal conductivity of nanofluids is measured with the aid of a KD2 thermal property meter (Labcell Ltd, UK), which is based on the transient hot wire method. Here the thermal conductivities of the nanofluids and base liquid (water) are measured at 293 K. The KD2 meter is calibrated using distilled water before any set of measurements.

The viscosity of nanofluids is measured with the use of a rotary viscometer (BROOKFIELD Co. DV-II+ProCP). The measurement is carried out at 293 K for the nanofluids of different concentrations and containing particles of three different materials. At least the viscosity for each nanofluid is measured three times and the mean value is applied as an effective viscosity of the nanofluid.

Figure 4 illustrates the experimental apparatus for measuring the convective heat transfer coefficient which consists of a closed flow loop, a heating unit, a cooling part, and a measuring and control unit. A straight stainless tube with 1000 mm in length, 3.96 mm in inner diameter, and 0.17 mm

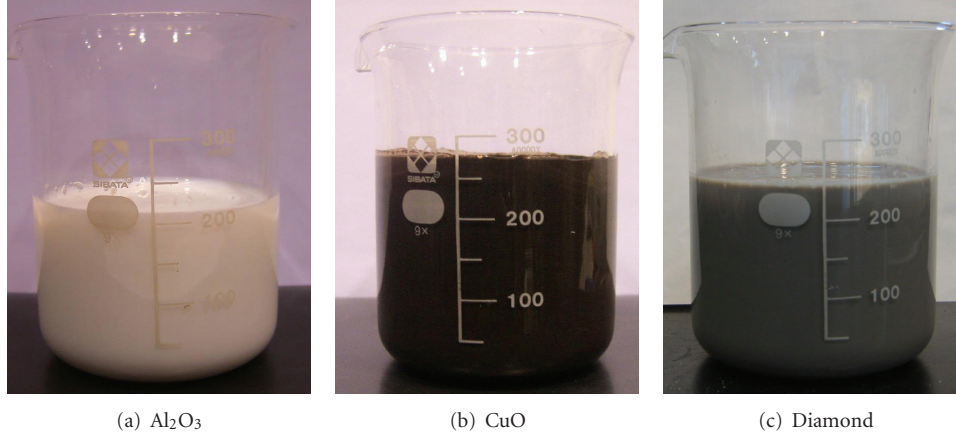


FIGURE 2: Nanofluids at 1 vol.% of particle volume fraction after 60 days.

in thickness is employed as the test section and electrodes for the direct electric current heating are connected at both ends. The DC power supply (TOKYO SEIDEN CVS1-5 K) is employed and its voltage is adjustable with the aid of the voltmeter (YOKOGAWA 2011). The test tube is surrounded by a thick thermal insulation material to suppress heat loss from the test section. The six thermocouples (100 μm in diameter), which are welded on the outer surface of the test tube, are used to measure the local wall temperature along the heated surface of the tube, and the other thermocouples are inserted into the flow at the inlet (T_{in}) and outlet (T_{out}) of the test section to measure the bulk temperature of a working fluid. Here, axial positions are 150 mm, 290 mm, 430 mm, 570 mm, 710 mm, and 850 mm from the inlet of the test section, whose locations are named as T_1 , T_2 , T_3 , T_4 , T_5 , and T_6 , respectively. The working fluid in the test loop is circulated by a magnet pump (IWAKI MD-100 RM). Here the maximum flow rate that the pump can deliver is 8 L/minute and is measured by an electromagnetic flowmeter (KYENCE FD-81SO). The pressure loss between the inlet of the test section and the outlet is measured with the aid of the differential pressure instrument (NAGANO-KEIKI NR-250). Notice that the test loop is cleaned up between runs even with the same nanofluid.

The measured local wall temperature and heat flux are used to calculate the local Nusselt number Nu_x defined by the following formula :

$$Nu_x = \frac{h_x D}{k}, \quad (1)$$

where D is the diameter of test tube, h_x is the local heat transfer coefficient, and k is the thermal conductivity of working fluid. Note that the thermal conductivity in (1) employs the value measured here. The local heat transfer coefficient is defined as

$$h_x = \frac{q}{(T_{wx} - T_{mx})}. \quad (2)$$

Here the subscript x represents axial distance from the entrance of the test section, q is the heat flux, T_{wx} is the

measured local wall temperature, and T_{mx} is the mixed mean temperature. The mixed mean temperature is determined by the following energy balance equation;

$$T_{mx} = T_{in} + \frac{qSx}{\rho CpAU}, \quad (3)$$

where T_{in} , ρ , and c_p are, respectively, the inlet temperature, the density, and the specific heat of fluid, S and A are, respectively, the outer surface area of test tube and the cross sectional area, and U is the averaged flow velocity.

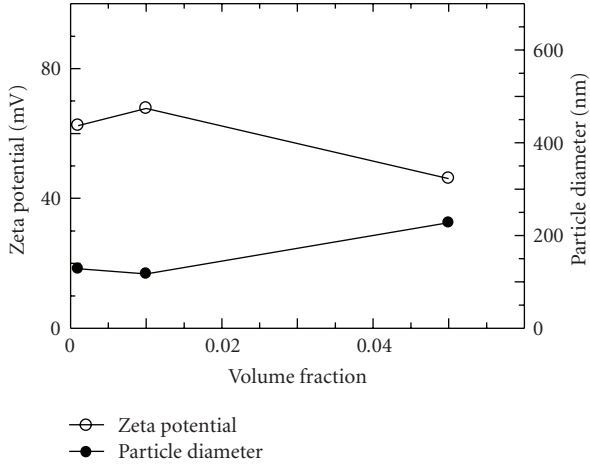
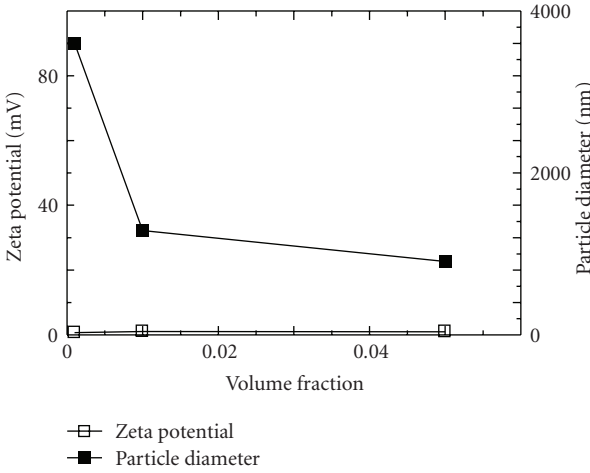
Three volumetric fractions of 0.1%, 1.0%, and 5.0% are tested for diamond/water, Al_2O_3 /water, and CuO/water nanofluids in the present study. The Reynolds number is ranged from 3000 to 10 000. An uncertainty analysis (Kline and McClintock [12]) yields the following results: the uncertainty in nanofluid flowrate is estimated to be $\pm 1.5\%$, the uncertainty in the physical properties is less than 1%, and the uncertainty in the temperature measurement is estimated to be $\pm 1.5\%$. The uncertainty of the measurements was within 3% under the conditions of this work.

3. Results and Discussions

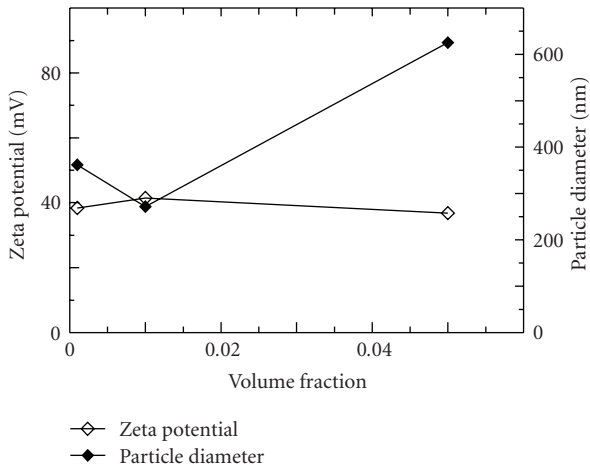
The measured effective thermal conductivity k_{nf} , for three different nanofluids, is illustrated in Figure 5 in the form of volume fraction versus dimensionless thermal conductivity where k_{nf} is divided by that of the base liquid (water), k_f . As a comparison, the prediction is superimposed in the figure as straight lines. Here the Hamilton and Crosser equation [13] (H-C equation) is employed. This equation is a classical formula to predict thermal conductivity of solid-liquid mixture;

$$k_{nf} = k_L \left[\frac{k_S + (n-1)k_L - (n-1)\phi(k_L - k_S)}{k_S + (n-1)k_L + \phi(k_L - k_S)} \right], \quad (4)$$

where ϕ shows volume fraction, and the subscript nf , S , and L indicate nanofluid, solid particles, and liquid, respectively, and n is sphere coefficient. Note that $n = 3$ is used in (4). The density ρ_{nf} and specific heat Cp_{nf} of nanofluid are estimated

(a) Al₂O₃

(b) CuO



(c) Diamond

FIGURE 3: Zeta potential and average particle diameter in nanofluids for various volume fractions.

from the physical properties of both nanoparticles and deionized water using the following correlations obtained

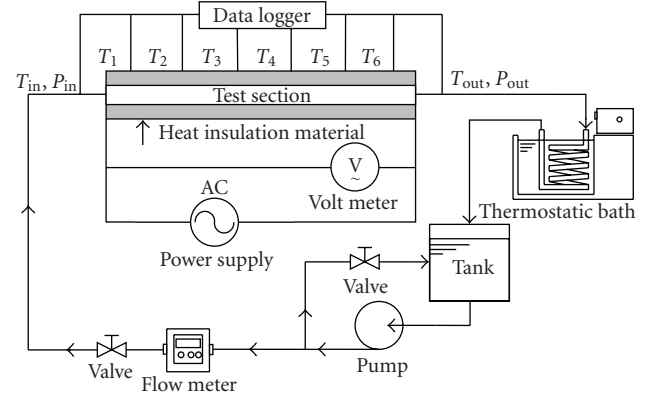


FIGURE 4: Experimental apparatus.

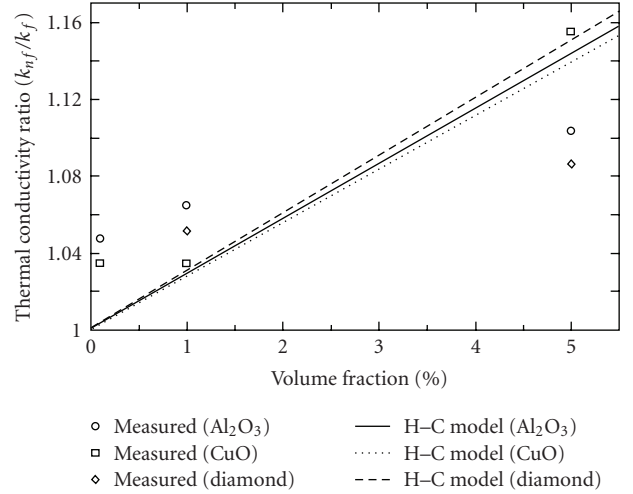


FIGURE 5: Measured thermal conductivity of nanofluids under different volume fractions.

at mean bulk temperature:

$$\rho_{nf} = \phi \rho_s + (1 - \phi) \rho_L, \quad (5)$$

$$Cp_{nf} = \frac{\phi (\rho_s Cp_{nf}) + (1 - \phi) (\rho_L Cp_{nf})}{\rho_{nf}}. \quad (6)$$

Note that the density and specific heat of the nanofluid in (3) are determined by (5) and (6), respectively. It is observed that the effective thermal conductivity increases with increasing the volume fraction and its trend is different for each nanofluid. In other words, the thermal conductivity of CuO-nanofluid is predicted by the correlation equation, while the corresponding values for diamond/water and CuO/water nanofluids become larger than that of the pure water in the low-volume fraction region and increases slightly in the higher volume fraction.

The viscosities for three different nanofluids, which are normalized by that of the pure water, are illustrated

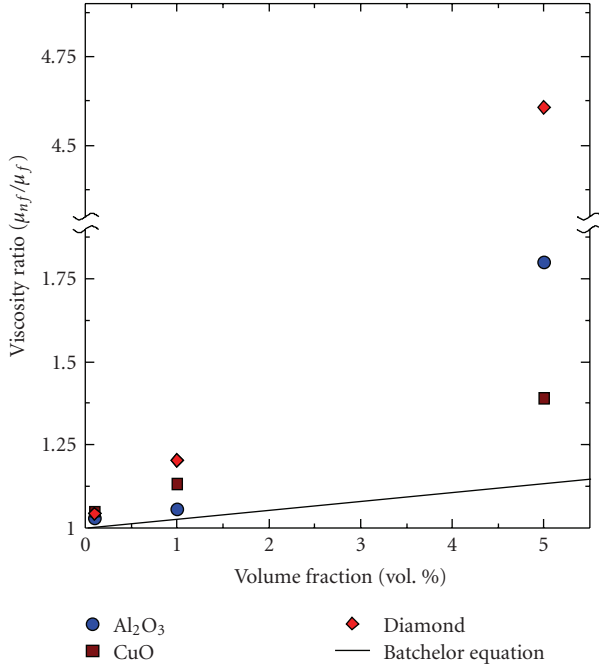


FIGURE 6: Relative viscosity for different nanofluids.

in Figure 6. For comparison, the prediction by Batchelor equation [14] is superimposed in Figure 6 as a solid line;

$$\frac{\mu_{nf}}{\mu_f} = 6.2\phi^2 + 2.5\phi + 1, \quad (7)$$

where μ_{nf} is viscosity of suspension and μ_f is that of a pure fluid. One observes that the measured viscosities of nanofluids are much higher than that of prediction, the viscosity of nanofluids increases with an increase in the particle concentration, and this trend is different for three nanoparticles. The effective particle volume fraction including cluster in a nanofluid becomes higher than that in the ideal suspension fluid in which each particle is independently and homogeneously dispersed in a fluid. In other words, the cluster including a fluid is considered as a particle, resulting in attenuation in the fluid volume fraction. Thus, the viscosity of diamond nanofluid is the highest, because diamond particles are strongly aggregated, as is seen in Figure 3(c), and cluster restricts a large amount of pure water. On the contrary, the viscosity of CuO nanofluid is relatively low because the CuO nanoparticles had already aggregated in the state of the powder.

The pressure loss between the test sections, for three different nanofluids, is illustrated in Figure 7 in the form of pressure drop versus flow rate at 5 vol% of volume fraction. The following equation for pure water is superimposed in the figure as lines for comparison;

$$\Delta p = \lambda \frac{l}{D} \frac{\rho U^2}{2}, \quad (8)$$

where l is the length of test tube and ρ is the density of nanofluid. The friction coefficient of the pipe λ is given by

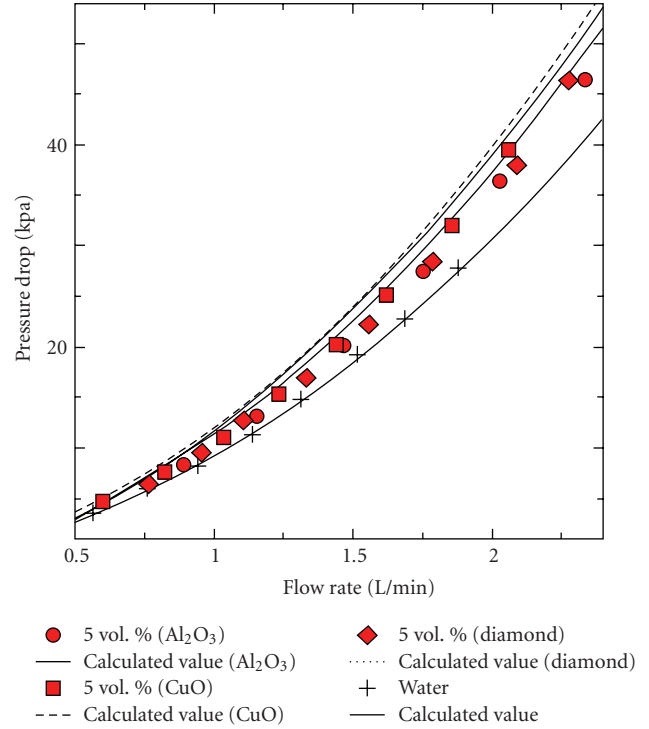


FIGURE 7: Pressure drop for different nanofluids at 5 vol%.

the Blasius equation, $\lambda = 0.3164Re^{-1/4}$. Here, the thermal properties in the Reynolds number (Re) are estimated using the density determined by (5) and the viscosity measured here. The pressure loss of the nanofluids is slightly increased compared with that of the pure water, because an increase in the friction loss is caused by suspension of nanoparticles in the pure fluid. Note that no substantial discrepancy for pressure loss appears in three different nanofluids and the pressure drop for each nanofluid is reasonably predicted by (8).

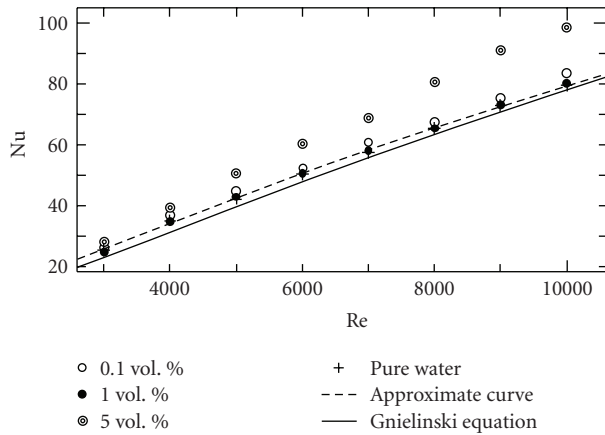
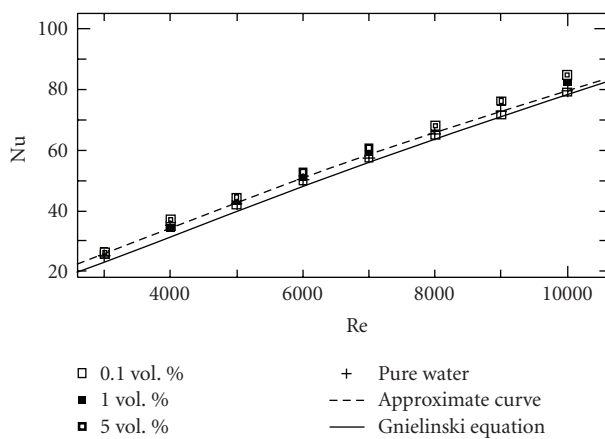
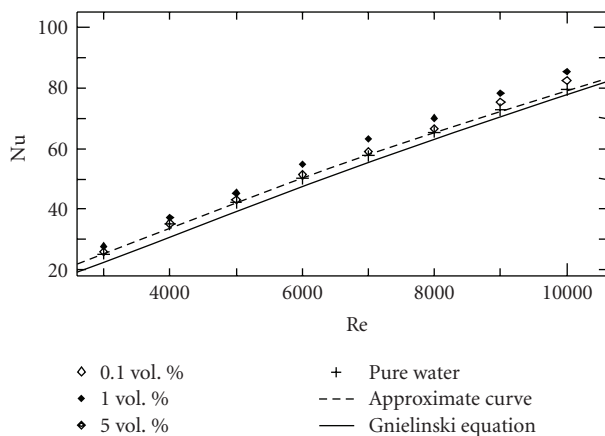
Next task is to consider the effect of suspension of nanoparticles on enhancement heat transfer. Figure 8 depicts the relationship between Nusselt number Nu and Reynolds number Re with different volume fractions, as a parameter. Figures 8(a), 8(b), and 8(c) correspond to the results for Al_2O_3 /water, CuO /water, and diamond/water nanofluids, respectively. Here the heat transfer coefficient in (1) is measured at $x/D = 200$, which corresponds to the hydrodynamically and thermally fully developed region based on the pre-experimental result. The following classical Gnielinski equation [15] in the turbulent flow is superimposed in Figure 8 as a solid line for reference;

$$Nu = \frac{(f/8)(Re - 1000)Pr}{1.07 + 12.7\sqrt{f/8}(Pr^{2/3} - 1)}. \quad (9)$$

Here, the friction coefficient f is calculated by

$$f = [1.82 \log_{10}(Re) - 1.64]^{-2}. \quad (10)$$

One observes that the Nusselt numbers for each nanofluid are higher than those for pure water. In other words, the

(a) Al_2O_3 (b) CuO 

(c) Diamond

FIGURE 8: Nusselt numbers for each nanofluid.

Nusselt numbers for 1 vol.% diamond, CuO , and Al_2O_3 nanofluids, at $\text{Re} = 6000 \pm 100$, show an enhancement of up to 9.8%, 6.6%, and 5.4%, respectively. In particular, heat transfer performance, for Al_2O_3 nanofluid, is intensified with an increase in the volume fraction of nanoparticles and this trend becomes larger in the higher Reynolds number

region. The heat transfer surface area of Al_2O_3 nanoparticles is the largest among three different nanoparticles because average diameter of the aggregated Al_2O_3 nanoparticles is the smallest, as is seen in Figure 3.

In other words, lower enhancement of heat transfer for diamond and CuO nanofluids is attributed to substantial aggregation of nanoparticles, which plays an important role in heat transfer performance. This is because average diameter of the aggregated diamond nanoparticles is increased with an increase in volume fraction, as is seen in Figure 3(c) so that the Nusselt number of 1.0 vol.% is almost the same as that of 5 vol.%, as is seen in Figure 8(c).

Throughout the experimental results, as the volume fraction of nanoparticles is increased, the viscosity of nanofluids with cluster and the pressure drop are amplified, but the latter is slightly affected by the different nanofluids. Heat transfer enhancement is caused by the suspension of particles and its trend is intensified with an increase in the volume fraction of particles and is attributed to average diameter of the aggregated nanoparticles. In order to suppress aggregation of nanoparticles, the absolute value of zeta potential for the particle in suspension has to be intensified.

4. Conclusions

Experimental study has been performed to investigate heat transfer performance of aqueous suspensions of nanoparticles, that is, Al_2O_3 , CuO , and diamond. The results are summarized as follows.

- The relative viscosity of nanofluids increases with an increase in concentration of nanoparticles, and the increase rate of the viscosity for nanofluid is different by the particle.
- The pressure loss of the nanofluids tends to increase slightly compared with that of pure water.
- Heat transfer performance in the circular tube flow is amplified by suspension of nanoparticles in comparison with that of pure water.
- Heat transfer enhancement is affected by the occurrence of particle aggregation, that is, zeta potential of nanoparticles in suspension.

Nomenclature

- A : Surface area of test section
 c_p : Specific heat
 D : Pipe diameter
 f : Friction factor, (10)
 h_x : Local heat transfer coefficient, (2)
 k : Thermal conductivity
 k_f : Thermal conductivity of the fluid
 k_s : Thermal conductivity of the discontinuous particle
 k_{nf} : Thermal conductivity of the nanofluid, (4)
 l : Length of test section
 n : Empirical shape factor

Nu: Nusselt number, (9)
 Pr: Prandtl number
 P: Pressure
 Q_x: Heating rate
 q: Heat flux
 Re: Reynolds number, UD/ν
 S: Cross section of test pipe
 T_{in}: Inlet fluid temperature
 T_{mx}: Mixed mean temperature, (3)
 T_{out}: Outlet fluid temperature
 V: Volume fraction of particle
 U: Mean velocity of fluid
 x: Coordinate
 α: Thermal diffusivity
 μ: Viscosity in (7)
 μ_{base}: Viscosity of a pure fluid
 ν: Kinematic viscosity
 φ: Volume fraction
 λ: Friction coefficient in (8)
 ρ: Density.

Subscripts

f: Fluid
 L: Liquid
 mx: Mean
 S: Solid or surface
 wx: Axial.

Acknowledgments

This study was supported by the Grants-in-Aid for Scientific Research (C) (no. 16560153) from Japan Society for the Promotion of Science (JSPS). The author would like to express his thanks to Mr. Satoh of Graduate School of Science and Technology, Kumamoto University, for the heat transfer experiment.

References

- [1] S. U. S. Choi, "Enhancing thermal conductivity of fluids with nanoparticles," in *Developments Applications of Non-Newtonian Flows*, D. A. Siginer and H. P. Wang, Eds., FED-vol. 231/MD-vol. 66, pp. 99–105, ASME, New York, NY, USA, 1995.
- [2] K. Khanafer, K. Vafai, and M. Lightstone, "Buoyancy-driven heat transfer enhancement in a two-dimensional enclosure utilizing nanofluids," *International Journal of Heat and Mass Transfer*, vol. 46, no. 19, pp. 3639–3653, 2003.
- [3] S. Lee, S. U. S. Choi, S. Li, and J. A. Eastman, "Measuring thermal conductivity of fluids containing oxide nanoparticles," *Journal of Heat Transfer*, vol. 121, no. 2, pp. 280–289, 1999.
- [4] S. P. Lee and U. S. Choi, "Application of metallic nanoparticles suspensions in advanced cooling system," in *Recent Advances in Solid/Structures and Application of Metallic Materials*, Y. Kwon, D. Davis, and H. Chung, Eds., PVP-Vol.342/MD-Vol.72, pp. 227–234, ASME, New York, NY, USA, 1996.
- [5] Q. Li and Y. Xuan, "Convective heat transfer performances of fluids with nano-particles," in *Proceedings of the 12th International Heat Transfer Conference*, pp. 483–488, 2002.
- [6] Y. Xuan and W. Roetzel, "Conceptions for heat transfer correlation of nanofluids," *International Journal of Heat and Mass Transfer*, vol. 43, no. 19, pp. 3701–3707, 2000.
- [7] Y. Xuan and Q. Li, "Investigation on convective heat transfer and flow features of nanofluids," *Journal of Heat Transfer*, vol. 125, no. 1, pp. 151–155, 2003.
- [8] Y. Ding, H. Alias, D. Wen, and R. A. Williams, "Heat transfer of aqueous suspensions of carbon nanotubes (CNT nanofluids)," *International Journal of Heat and Mass Transfer*, vol. 49, no. 1–2, pp. 240–250, 2006.
- [9] B. C. Pak and Y. I. Cho, "Hydrodynamic and heat transfer study of dispersed fluids with submicron metallic oxide particles," *Experimental Heat Transfer*, vol. 11, no. 2, pp. 151–170, 1998.
- [10] Y. Yang, Z. G. Zhang, E. A. Grulke, W. B. Anderson, and G. Wu, "Heat transfer properties of nanoparticle-in-fluid dispersions (nanofluids) in laminar flow," *International Journal of Heat and Mass Transfer*, vol. 48, no. 6, pp. 1107–1116, 2005.
- [11] X.-Q. Wang and A. S. Mujumdar, "Heat transfer characteristics of nanofluids: a review," *International Journal of Thermal Sciences*, vol. 46, no. 1, pp. 1–19, 2007.
- [12] S. J. Kline and F. A. McClintock, "Describing uncertainties in single-sample experiments," *Mechanical Engineering*, vol. 75, no. 1, pp. 3–8, 1953.
- [13] R. L. Hamilton and O. K. Crosser, "Thermal conductivity of heterogeneous two-component systems," *Industrial and Engineering Chemistry Fundamentals*, vol. 1, no. 3, pp. 187–191, 1962.
- [14] G. K. Batchelor, "The effect of Brownian motion on the bulk stress in a suspension of spherical particles," *Journal of Fluid Mechanics*, vol. 83, no. 1, pp. 97–117, 1977.
- [15] V. Gnielinski, "New equations for heat and mass transfer in turbulent pipe and channel flow," *International Chemical Engineering*, vol. 16, pp. 359–368, 1976.

Research Article

Field Synergy Principle for Energy Conservation Analysis and Application

Qun Chen,¹ Moran Wang,² and Zeng-Yuan Guo¹

¹Key Laboratory for Thermal Science and Power Engineering of Ministry of Education, Department of Engineering Mechanics, Tsinghua University, Beijing 100084, China

²Earth and Environmental Sciences Division, Los Alamos National Laboratory, Los Alamos, NM 87545, USA

Correspondence should be addressed to Moran Wang, mwang@lanl.gov and Zeng-Yuan Guo, demgzy@tsinghua.edu.cn

Received 28 April 2009; Accepted 5 September 2009

Academic Editor: Chen Li

Copyright © 2010 Qun Chen et al. This is an open access article distributed under the Creative Commons Attribution License, which permits unrestricted use, distribution, and reproduction in any medium, provided the original work is properly cited.

Optimization of mass and energy transfer process is critical to improve energy efficiency. In this contribution we introduce the field synergy principle as a unified principle for analyzing and improving the performance of the transfer process. Three field synergy numbers are introduced for heat, mass, and momentum transfer, respectively, and three cases are demonstrated for validation. The results indicate that the field synergy numbers will increase when reducing the angle between the velocity vector and the temperature gradient or the species concentration gradient fields in the convective heat or mass transfer, and the overall heat or mass transfer capability is therefore enhanced. In fluid flows, it will reduce the fluid flow drag to decrease the synergy number between the velocity and the velocity gradient fields over the entire domain and to decrease the product between the fluid viscosity and the velocity gradient at the boundary simultaneously.

1. Introduction

Energy conservation is not only a scientific or engineering problem but also a social one that most people on this planet are facing [1–3]. Solutions of this problem include both developments of new substitutable energy products [4–6] and optimizations of current energy utilizations [7–9]. The energy efficiency is always expected maximized by enhancing the energy output for a given cost, or by minimizing the input energy loss for a given output [10]. In recent years, the multiphysical transport process in energy systems, involving mass and energy transfer, has been a hot but challenging topic [6]. The difficulties come mainly from the coupling of the multiphysical transport processes. In this work, we focus on the fluid flow coupled with species or heat transfer, which is one of the most popular transport phenomena in energy systems. In such a multiphysical process, three kinds of transports are involved: the fluid flow (momentum transport), heat transfer (energy transport), and species transfer (mass transport) [11–13].

During the past several decades, a great number of heat, mass transfer enhancement, and fluid flow drag reduction

technologies have been developed including using extended surfaces, spoiler elements, and external electric or magnetic field [14–17] for heat and mass transfer, riblet surfaces, guide plates, and drag-reduction additives of low viscosity for fluid flow [18–20]. All these methods have successfully cut down not only the energy consumption but also the cost of equipment itself. In the meanwhile, in the interest of revealing the essence of these methods from the viewpoint of velocity and temperature fields, Guo et al. [21–24] proposed a concept of field synergy for enhancing convective heat transfer. They pointed out that increasing the synergy, that is, reducing the included angle, between velocity and temperature gradient, can effectively enhance convective heat transfer. Chen et al. extended this concept to the convective mass, transfer and fluid flow [25–27].

The purpose of this work is to study the transport phenomena performance based on the field synergy theory and the analogy between heat, mass and momentum transfer. The field synergy principle is available for analyzing and improving heat, mass and momentum transfer performance. Some numerical examples will be provided for validation of this principle.

2. The Analogies and the Linear Transport Laws in Transfer Processes

Momentum, heat, and mass transfer processes are always considered to be three analogous phenomena for the following two reasons: (1) the generation mechanisms are the same, that is, viscous force, thermal conduction, and mass diffusion are all caused by the motion and interaction of molecules, and (2) the govern equations of these phenomena are similar. That is, when there exists a macroscopic gradient of velocity, temperature, or concentration in an object, and the gradient is not large enough, this transport phenomenon can be described by Newton's law of viscosity, Fourier's law of heat conduction, or Fick's law of diffusion:

$$\tau_{yx} = -\mu \frac{du_x}{dy}, \quad (1)$$

$$\dot{q} = -\lambda \frac{dT}{dn}, \quad (2)$$

$$\dot{m} = -\rho D \frac{dY}{dn}. \quad (3)$$

Equation (1) describes the linear relation of the shearing force per unit area with the velocity gradient during fluid flow processes, which is the stress strain constitutive relation of Newtonian fluid. The velocity gradient is the strain, and the shearing force is the stress.

As is shown in (2) and (3), the transferred parameters are proportional to the gradients of some corresponding physical quantities, respectively, during heat and mass transfer processes, where the gradient of the temperature and the concentration are understood as "driving forces," and heat and mass crossing a unit area per unit time are the "fluxes". Furthermore, the "fluxes" have linear relationship with their corresponding "driving forces". Thus, it can be concluded that both Fourier's law and Fick's law reflect and express the general rules of diffusion processes, not the stress strain constitutive relation. It seems that neither heat nor mass transfer process is analogous to fluid flow process.

However, Newton's law of viscosity has double meanings. It expresses not only the constitutive relation of fluids but also the relationship between the velocity gradient and the momentum flux. In this connection, the velocity gradient, caused by the fluid deformation during fluid flow processes, leads to the diffusion of momentum in fluids, where the velocity gradient and the transferred momentum can therefore be thought as the driving force and the flux as momentum transport, respectively. Newton's law is the same as Fourier's law and Fick's law, which all expresses the general rules of diffusion processes. Here, (1) can also be expressed as

$$q_{mom,y} = \rho u_x v_y^* = -\mu \frac{du_x}{dy}, \quad (4)$$

where $q_{mom,y}$ stands for the momentum flux in the y direction and v_y^* is the diffusion velocity in the y direction of x -momentum component, rather than the velocity of fluid itself.

In addition, the governing equations are the energy conservation equation for convective heat transfer

$$\rho c_p \vec{U} \cdot \nabla T = \nabla \cdot (\lambda \nabla T) + Q, \quad (5)$$

the species conservation equation for convective mass transfer

$$\rho \vec{U} \cdot \nabla Y = \nabla \cdot (\rho D \nabla Y) + M, \quad (6)$$

and the momentum conservation equation for fluid flow,

$$\rho \vec{U} \cdot \nabla \vec{U} = -\nabla P + \mu \nabla^2 \vec{U} + F, \quad (7)$$

can be rewritten to a generalized form as follows:

$$\rho \vec{U} \cdot \nabla \varphi = \eta \nabla \cdot (\nabla \varphi) + G, \quad (8)$$

where \vec{U} is the velocity vector, φ is the universal variable (e.g., temperature, mass fraction and velocity), η is the generalized diffusion coefficient, and G is the source term.

In summary, due to the aforementioned analogy between heat, mass, and momentum transfer, a unified principle can be developed to analyze these transfer phenomena.

3. Field Synergy Principle in Convective Heat Transfer

For two-dimensional boundary layer flows and heat transfer along a plate [23], the energy conservation equation is

$$\rho c_p (\vec{U} \cdot \nabla T) = \frac{\partial}{\partial y} \left(\lambda \frac{\partial T}{\partial y} \right). \quad (9)$$

Integrating (9) along the thermal boundary layer with the boundary condition at the outer edge of the thermal boundary layer being $(\partial T / \partial y)_{\delta_{t,x}} = 0$ gives

$$\int_0^{\delta_{t,x}} \rho c_p (\vec{U} \cdot \nabla T) dy = -\lambda \frac{\partial T}{\partial y} \Big|_w. \quad (10)$$

The right-hand side is the heat flux, q_w , between the solid wall and the fluid, while the left-hand side is the scalar product between the velocity vector and the temperature gradient, which can be written as

$$\int_0^{\delta_{t,x}} \rho c_p (\vec{U} \cdot \nabla T) dy = \int_0^{\delta_{t,x}} \rho c_p |\vec{U}| |\nabla T| \cos \beta_h dy, \quad (11)$$

where β_h is the included angle between the velocity vector and the temperature gradient. Thus, for two-dimensional boundary heat transfer along a plate, the boundary heat flux depends not only on the magnitude of the velocity and the temperature gradient but also on the included angle between them. It is obvious that for a fixed flow rate and temperature difference, a smaller intersection angle between the velocity and the temperature gradient will lead to a larger heat flow rate.

For a three-dimensional elliptic heat transfer process without internal heat source [28], the energy conservation equation is

$$\rho c_p \vec{U} \cdot \nabla T = \nabla \cdot (\lambda \nabla T). \quad (12)$$

Integrating this equation over the entire heat transfer domain, Ω , and transforming the volume integral to a surface integral using the Green's theorem give

$$\iiint_{\Omega} \rho c_p \vec{U} \cdot \nabla T dV = \iint_{\Gamma} \vec{n} \cdot (\lambda \nabla T) dS, \quad (13)$$

where \vec{n} is the outward normal unit vector, and Γ is the boundary of the heat transfer area, which will be divided into heat transfer surfaces, adiabatic surfaces, fluid inlets, and outlets. Thus, the right-hand side of (13) is divided into four terms:

$$\begin{aligned} \iint_{\Gamma} \vec{n} \cdot (\lambda \nabla T) dS &= \iint_{hts} \vec{n} \cdot (\lambda \nabla T) dS + \iint_{as} \vec{n} \cdot (\lambda \nabla T) dS \\ &+ \iint_{in} \vec{n} \cdot (\lambda \nabla T) dS + \iint_{out} \vec{n} \cdot (\lambda \nabla T) dS. \end{aligned} \quad (14)$$

The first term is the heat flow rate between the solid wall and the fluid. On adiabatic surfaces, the temperature gradient is zero, and so the second integral is zero. The third and fourth terms are the axial thermal diffusion at the inlet and outlet, respectively, which may be neglected when compared to the energy transferred by the fluid motion [28]. Thus, (13) is simplified as

$$\begin{aligned} &\iiint_{\Omega} \rho c_p \vec{U} \cdot \nabla T dV \\ &= \iiint_{\Omega} \rho c_p \left| \vec{U} \right| |\nabla T| \cos \beta_h dV = \iint_{hts} \vec{n} \cdot (\lambda \nabla T) dS. \end{aligned} \quad (15)$$

For a convective heat transfer process, V is the volume and S_{hts} is the heat transfer surface, and then a characteristic length, $L = V/S_{hts}$, can be defined. After introducing the dimensionless variables,

$$\vec{U} = \frac{\vec{U}}{U_{in}}, \quad \nabla T = \frac{\nabla T}{(T_{hts} - T_{in})/L}, \quad dV = \frac{dV}{V}, \quad (16)$$

equation (15) will be written in a dimensionless form as

$$Nu = \text{Re Pr} \iiint_{\Omega} \vec{U} \cdot \nabla T d\bar{V} = \text{Re Pr} \iiint_{\Omega} \left| \vec{U} \right| |\nabla T| \cos \beta_h d\bar{V}. \quad (17)$$

Equation (17) shows that the Nusselt number, that is, convective heat transfer performance, depends not only on the Reynolds number and the Prandtl number but also on the value of $\iiint_{\Omega} \vec{U} \cdot \nabla T d\bar{V}$.

According to the Webster Dictionary [29], when several actions or forces are cooperative or combined, such situation can be called ‘‘synergy’’. Thus, the above idea is named the ‘‘field synergy principle’’ by Guo et al. [21], and $\iiint_{\Omega} \vec{U} \cdot \nabla T d\bar{V}$ is named the heat transfer field synergy number, F_{ch} , which represents the synergic degree of the velocity vector and the temperature gradient over the entire volume. When the heat transfer fluid is selected and the flow rate is fixed, both the Reynolds number and the Prandtl are constant, and then the heat transfer field synergy number determines the convective heat transfer capability.

For three-dimensional turbulent heat transfer without internal heat source, the time-averaged energy conservation equation is

$$\rho c_p \langle \vec{U} \rangle \cdot \langle \nabla T \rangle = \nabla \cdot [(\lambda + \lambda_t) \langle \nabla T \rangle]. \quad (18)$$

Similarly, integrating (18) over the entire heat transfer domain and transforming the volume integral to a surface integral give

$$\iiint_{\Omega} \rho c_p \langle \vec{U} \rangle \cdot \langle \nabla T \rangle dV = \iint_{hts} \vec{n} \cdot (\lambda + \lambda_t) \langle \nabla T \rangle dS, \quad (19)$$

where $\langle \vec{U} \rangle$ and $\langle \nabla T \rangle$ are the time-averaged velocity vector and the time-averaged temperature gradient, respectively. λ_t is the turbulent thermal conductivity.

The turbulent thermal conductivity vanishes at the boundary; thus (19) is simplified as

$$\iiint_{\Omega} \rho c_p \langle \vec{U} \rangle \cdot \langle \nabla T \rangle dV = \iint_{hts} \vec{n} \cdot \lambda \langle \nabla T \rangle dS. \quad (20)$$

The right-hand side is the heat flow rate between the solid wall and the fluid. Introducing some dimensionless variables, as shown in (16), to (20) gives

$$Nu = \text{Re Pr} \iiint_{\Omega} \langle \vec{U} \rangle \cdot \langle \nabla T \rangle d\bar{V} \quad (21)$$

$$= \text{Re Pr} \iiint_{\Omega} \left| \langle \vec{U} \rangle \right| \left| \langle \nabla T \rangle \right| \cos \beta_{ht} d\bar{V},$$

where $\iiint_{\Omega} \langle \vec{U} \rangle \cdot \langle \nabla T \rangle d\bar{V}$ is the field synergy number for turbulent heat transfer, F_{cht} , and β_{ht} is the included angle between the time-averaged velocity vector and the time-averaged temperature gradient. For a given flow rate, increasing the field synergy number will enhance turbulent heat transfer.

The field synergy principle in convective heat transfer has been validated numerically and experimentally [21–24, 30, 31]. Based on this principle, some existing heat transfer enhancement methods will be furthermore understood. Tao et al. [22] showed that reducing the thickness of the thermal boundary layer, increasing the disturbance in the fluid, and increasing the velocity gradient at the solid wall are all unified by the field synergy principle. That is, all of these methods reduce the included angle between the (time-averaged) velocity vector and the (time-averaged)

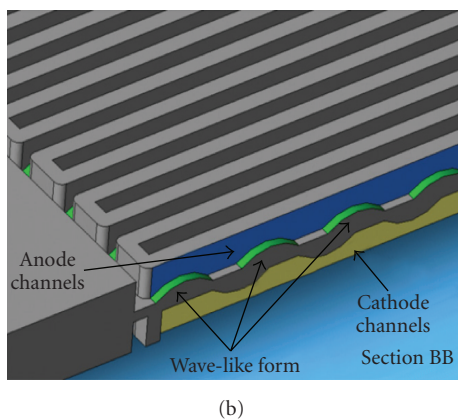
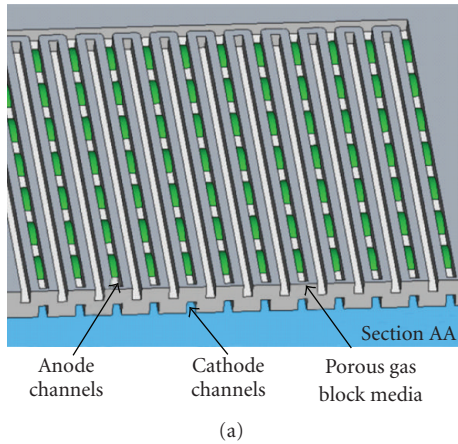


FIGURE 1: Cross-section and side view of gas flow channel with periodic wave-like geometry in bipolar plate of a PEMFC [35].

temperature gradient and finally increase the field synergy number between them [31]. Moreover, the field synergy principle led to the development of some novel heat transfer enhancement technologies, such as the alternating elliptical axis tubes [32], the discrete double inclined ribs tubes [33], and the “front coarse and rear dense” slotted fins [34].

In addition, by using the field synergy principle, Kuo and Chen [35] numerically studied a gas flow channel with a periodic wave-like geometry, shown in Figure 1, to improve the heat transfer of the bipolar plate in dissipating the heat generated during the catalysis reaction and, consequently, to improve the performance of PEMFC. In this configuration, the porosity and thickness of the gas diffusion layer are 0.5 and $300\ \mu\text{m}$, respectively. The cross-section hydraulic diameter and length of the gas flow channels are 0.015 m and 0.1 m, respectively. The bipolar plate side of the channel has a wave-like form with a period of 0.01 m.

Figure 2 shows the variation of the Nusselt number with the Reynolds number in the straight and wave-like form gas flow channels, respectively. The wave-like geometry enhances the thermal performance, particularly at higher Reynolds numbers. When $Re = 200$, the wave-like geometry increases

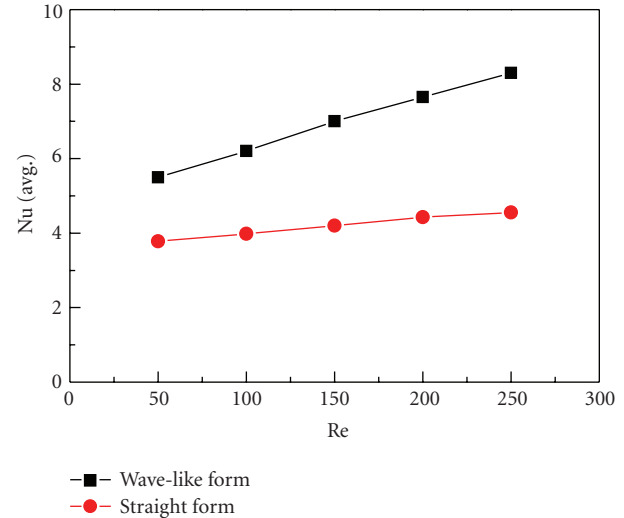


FIGURE 2: Variation of average Nusselt number with Reynolds number in two gas flow channel geometries (straight and wave-like) [35].

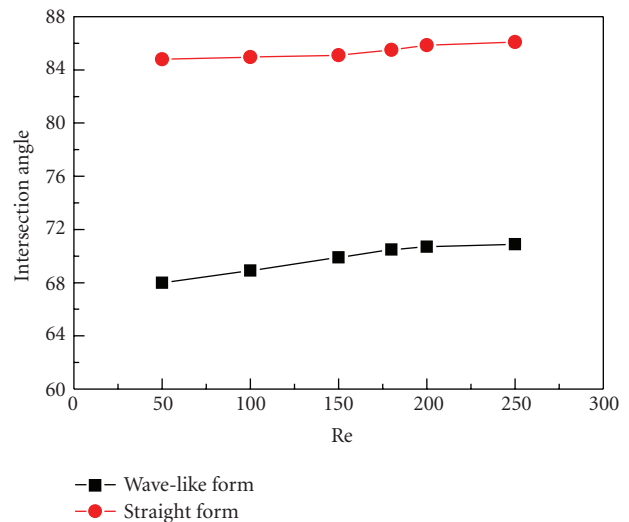


FIGURE 3: Variation of average intersection angle with Reynolds number in two gas flow channel geometries (straight and wave-like) [35].

the value of Nu by approximately 20%. Figure 3 shows the variation of the average included angle with the Reynolds number for the straight gas flow channel and for the channel with the wave-like form geometry. When $Re = 200$, the average intersection angle of the velocity vector and the temperature gradient in the straight channel is 87° , while the intersection angle is reduced to 70.5° in the gas flow channel with the wave-like form geometry. Hence, improving the field synergic degree between the velocity vector and the temperature gradient by reducing their average included angle over the entire domain will improve convective heat transfer capacity.

4. Field Synergy Principle in Convective Mass Transfer

For convective mass transfer processes [25, 26], the steady-state three-dimensional species conservation equation without mass sources can be written as

$$\rho \vec{U} \cdot \nabla Y = \nabla \cdot (\rho D \nabla Y). \quad (22)$$

Integrating this equation over the entire mass transfer domain, Ω , and transforming the volume integral to the surface integral yield

$$\iiint_{\Omega} \rho \vec{U} \cdot \nabla Y dV = \iint_{\Gamma} \vec{n} \cdot (\rho D \nabla Y) dS. \quad (23)$$

Similar to convective heat transfer processes, the domain boundary will be divided into species emitting surfaces, surface without mass transfer, inlets, and outlets. Thus (23) is written as

$$\begin{aligned} & \iint_{\Gamma} \vec{n} \cdot (\rho D \nabla Y) dS \\ &= \iint_{ms} \vec{n} \cdot (\rho D \nabla Y) dS + \iint_{nms} \vec{n} \cdot (\rho D \nabla Y) dS \\ &+ \iint_{in} \vec{n} \cdot (\rho D \nabla Y) dS + \iint_{out} \vec{n} \cdot (\rho D \nabla Y) dS. \end{aligned} \quad (24)$$

On surfaces without mass transfer, the species concentration gradient is zero, so the second integral on the right hand is zero. At the inlet and outlet, the air velocity is high and the species concentration gradient is relatively small; and so the axial diffusion of the species at the inlet and outlet, that is, the third and fourth integrals on the right hand, can be neglected. Thus, (23) is simplified as

$$\begin{aligned} & \iiint_{\Omega} \rho \vec{U} \cdot \nabla Y dV \\ &= \iiint_{\Omega} \rho |\vec{U}| |\nabla Y| \cos \beta_m dV = \iint_{ms} \vec{n} \cdot (\rho D \nabla Y) dS, \end{aligned} \quad (25)$$

where β_m is the included angle between the velocity vector and the concentration gradient. As seen from (25), the integral of the density times the dot product of the velocity vector and the concentration gradient over the entire domains equals the overall mass flow rate, \dot{m} .

Introducing some dimensionless variables to (25) leads to a dimensionless form:

$$Sh = Re Sc \iiint_{\Omega} \left| \frac{\vec{U}}{U} \right| \left| \frac{\nabla Y}{Y} \right| \cos \beta_m d\bar{V}. \quad (26)$$

Similar to turbulent heat transfer, substituting some turbulent physical parameters for laminar ones in (26) gives

$$Sh = Re Sc \iiint_{\Omega} \left| \langle \vec{U} \rangle \right| \left| \langle \nabla Y \rangle \right| \cos \beta_{mt} d\bar{V}, \quad (27)$$

where Sh and Sc represent the Sherwood number and the Schmidt number. $\langle \nabla Y \rangle$ is the time-averaged species

concentration gradient. Both (26) and (27) show that the Sherwood numbers for laminar and turbulent mass transfer depend not only on the Reynolds number and the Schmidt number but also on the integral value of $\vec{U} \cdot \nabla Y$ and $\langle \vec{U} \rangle \cdot \langle \nabla Y \rangle$, respectively. These values are defined as the mass transfer field synergy numbers, F_{c_m} or $F_{c_{mt}}$, which represent the synergy between the (time-averaged) velocity vector and the (time-averaged) species concentration over the entire volume. Similarly, when the fluid is selected, the various ways for increasing the overall strength of convective mass transfer can be classified into: (1) increasing the Reynolds number which means increasing the fluid flow rates and (2) increasing the mass transfer field synergy number. For a given fluid flow rate, the Reynolds number is constant, and the convective mass transfer capability is determined by the mass transfer field synergy number.

In the field of indoor air purification, the field synergy principle in convective mass transfer has led to the development of the decontamination ventilation designs [25] and the discrete double-inclined ribs in photocatalytic oxidation reactors [26] to enhance convective mass transfer and, consequently, to improve contaminant removal performance. To illustrate the applicability of field synergy principle for convective mass transfer processes, the decontamination quality was varied by changing the boundary conditions. The results were used to analyze the influence of the convective mass transfer field synergy on the overall mass transfer rate.

The overall mass transfer rate and field synergy number for various ventilation types are compared, including a horizontal inlet at the lower left corner (type A, Figure 4(a)), a vertical inlet at the top left corner (type B, Figure 4(b)), a horizontal inlet at the top right corner (type C, Figure 4(c)), a horizontal inlet at the top left corner (type D, Figure 4(d)), and a vertical inlet at the top right corner (type E, Figure 4(e)). The dimensions of all the rectangular cavity are: $L = 4$ mm, $H = 3$ mm, and $W_1 = W_2 = W_3 = W_4 = 0.2$ mm. The air intake velocities are 1 m/s or 2 m/s. The inlet air has a contaminant mass fraction of 0. The bottom is the contaminant source with a contaminant mass fraction of 0.01, while the left, right, and upper surfaces of the cavity all have no mass transfer.

The numerical results in Figures 5 and 6 show that for the same air inlet velocity, both the overall mass transfer rate and the mass transfer field synergy number decrease from the highest in type A to B, C, D, and the lowest in type E. For a given air inlet velocity, the Reynolds number is constant; so the overall mass transfer rate is only determined by the mass transfer field synergy number. Therefore, a better ventilation arrangement can be obtained by comparing various velocity fields for various ventilation arrangements, and by selecting the arrangement with largest mass transfer field synergy number.

5. Field Synergy Principle in Momentum Transfer-Fluid Flow

For fluid flows [27], the momentum equation for steady-state fluid flow without volume force can be written as

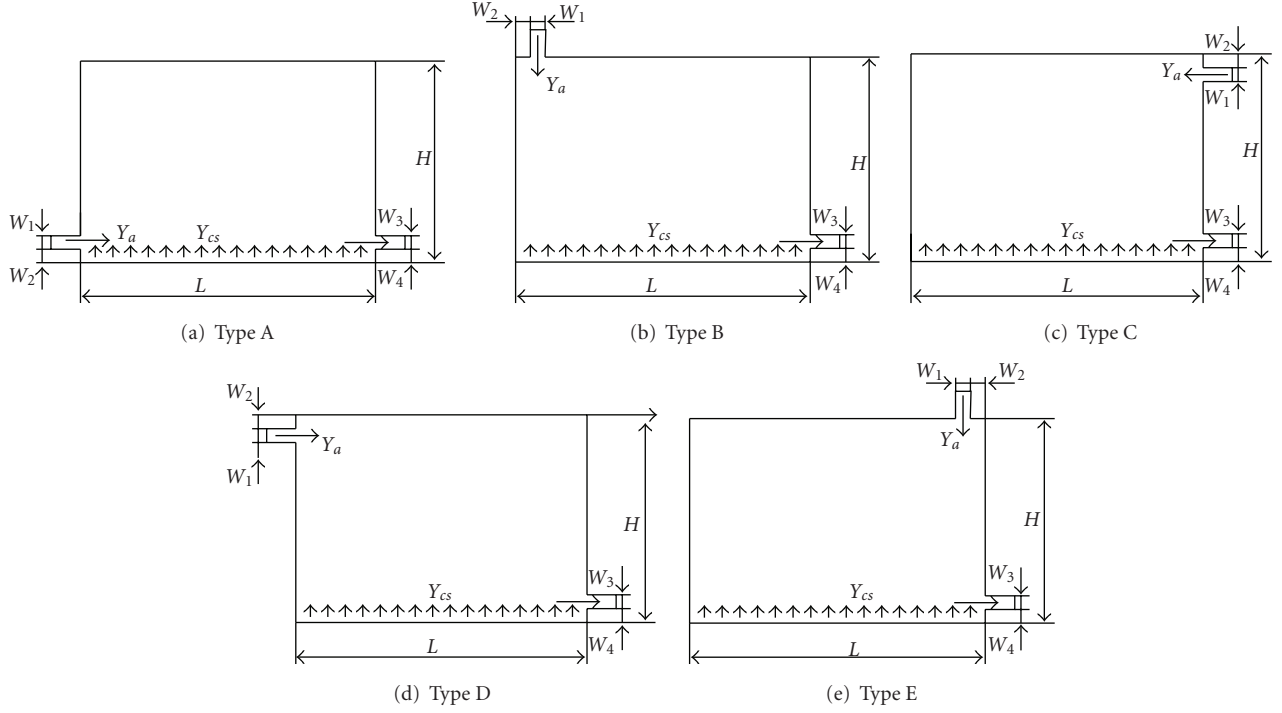


FIGURE 4: Sketches of ventilation configurations.

$$\rho u_j \frac{\partial u_i}{\partial x_j} = -\frac{\partial P}{\partial x_i} + \frac{\partial}{\partial x_j} \left(\mu \frac{\partial u_i}{\partial x_j} \right), \quad (28)$$

where P is the pressure, μ is the kinematic viscosity, and u_i and u_j are the velocity components in i, j direction. Integrating this equation over the entire domain, Ω , and transforming the volume integral into a surface integral, we have

$$\iiint_{\Omega} \rho u_j \frac{\partial u_i}{\partial x_j} dV = -\iiint_{\Omega} \frac{\partial P}{\partial x_i} dV + \iint_{\Gamma} \mu \frac{\partial u_i}{\partial x_j} \cdot \vec{n} dS. \quad (29)$$

By introducing the dimensionless variables

$$\begin{aligned} \bar{u}_i &= \frac{u_i}{u_{in}}, & \bar{u}_j &= \frac{u_j}{u_{in}}, & \nabla \bar{u}_i &= \frac{\nabla u_i}{u_{in}/D}, \\ d\bar{V} &= \frac{dV}{V}, & d\bar{S} &= \frac{dS}{S}, \end{aligned} \quad (30)$$

equation (30) can be rewritten as

$$-\frac{D}{\rho u_{in}^2} \iiint_{\Omega} \frac{\partial P}{\partial x_i} d\bar{V} = \iiint_{\Omega} \rho \bar{u}_j \frac{\partial \bar{u}_i}{\partial x_j} d\bar{V} - \frac{\mu}{\rho u_{in} D} \iint_{\Gamma} \nabla \bar{u}_i \cdot \vec{n} d\bar{S}. \quad (31)$$

The term on the left-hand side of (31) is the dimensionless pressure drop in x_i direction, denoted as the drag during the flow:

$$\Delta \bar{P}_i = -\frac{D}{\rho u_{in}^2} \iiint_{\Omega} \frac{\partial P}{\partial x_i} d\bar{V}. \quad (32)$$

The first term on the right-hand side is the integration of the dot product between the dimensionless velocity and

the velocity gradient vectors, representing the field synergy between them in the entire domain, which referred to as the flow field synergy number:

$$\begin{aligned} FS_{fi} &= \iiint_{\Omega} \bar{u}_j \frac{\partial \bar{u}_i}{\partial x_j} d\bar{V} = \iiint_{\Omega} \bar{U} \cdot \nabla \bar{u}_i d\bar{V} \\ &= \iiint_{\Omega} |\bar{U}| |\nabla \bar{u}_i| \cos \beta_{fi} d\bar{V}, \end{aligned} \quad (33)$$

where β_{fi} denotes the included angle between the velocity and the x_i -velocity component gradient vectors. The value of FS_{fi} depends not only on the velocity and the x_i -velocity component gradient but also on their included angle (their synergy). A large value of β_{fi} leads to a small value of FS_{fi} , indicating a weak synergy between the velocity and x_i -velocity component gradient fields, and consequently a small flow drag in x_i direction. In addition, it is worth noting that the fluid viscosity μ is not involved in (34). That is, the flow field synergy number is not influenced by the fluid viscosity.

The second term on the right hand is the total dimensionless boundary viscous force due to x_i -velocity component gradient, determined by both the dynamic viscosity and the velocity gradient at the boundary:

$$\bar{\tau}_i = \frac{1}{\rho u_{in} D} \iint_{\Gamma} \mu \left(-\frac{\partial \bar{u}_i}{\partial x_j} \cdot \vec{n} \right) d\bar{S}. \quad (34)$$

Substituting (32), (33), and (34) into (31) gives

$$\Delta \bar{P}_i = FS_i + \bar{\tau}_i. \quad (35)$$

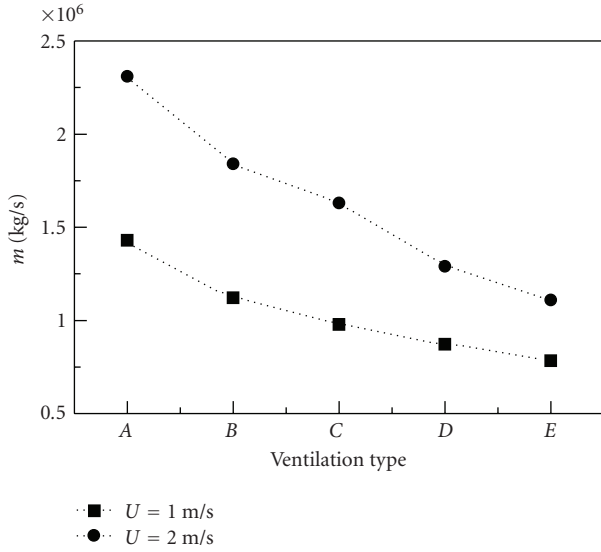


FIGURE 5: Decontamination rates for various ventilation arrangements.

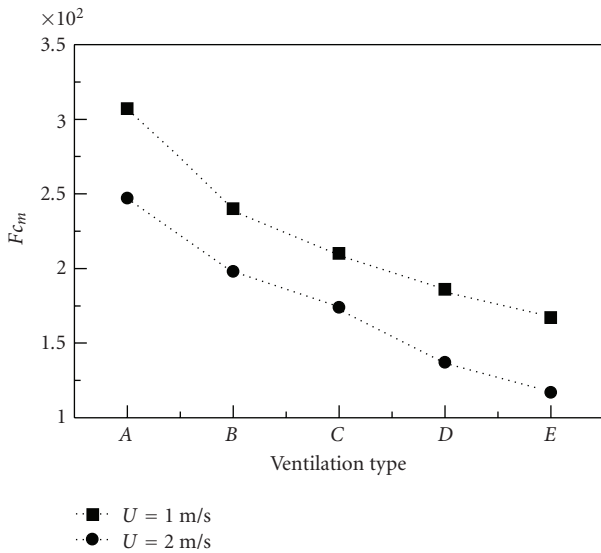


FIGURE 6: Field synergy numbers for various ventilation arrangements.

As is seen in (35), the flow drag depends on two factors: one is the synergy between the velocity and its gradient over the entire flow domain, and the other is the viscous force at the boundary. Hence, for a given flow rate, there are two ways to reduce the flow drag, such as (1) reducing the flow field synergy number by enlarging the synergy angle β_{fi} between the velocity and its x_i -velocity component gradient and (2) decreasing the fluid viscosity μ and/or the velocity gradient at the boundary Γ , rather than the entire flow domain. This field synergy principle in fluid flows also presents a novel approach for analyzing flow processes and sets the direction for developing new flow drag reduction technologies including designing suitable velocity distributors [27] for pipe networks and generating

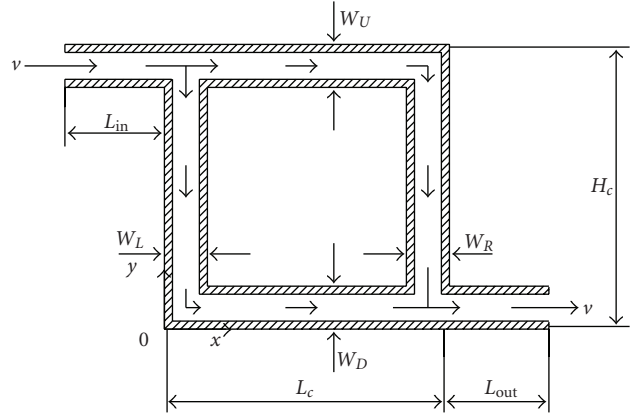


FIGURE 7: Sketch of the flow in a simple duct network.

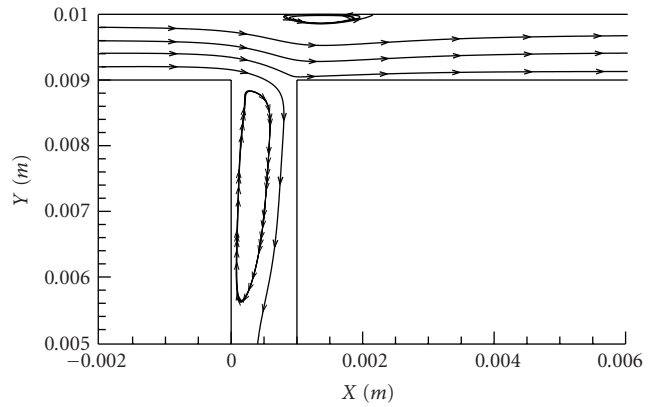


FIGURE 8: Air streamline field nearby the top left fork.

multilongitude vortices during heavy oil transport processes [36].

For instance, consider a 2D fluid flow in a simple duct network [27] shown in Figure 7. The channel splits into two paths forming the shape of a rectangle which later converge back into one channel. The dimensions are $L_c = H_c = 10$ mm, $L_{in} = L_{out} = 4$ mm, and $W_U = W_D = W_L = W_R = 1$ mm. The wall thickness of the duct is neglected. Air flows in the flow domain horizontally from the top left corner with a velocity of 5 m/s and out from the lower right corner. The air density and dynamic viscosity are 1.225 kg/m³ and 1.7894×10^{-5} kg/(m · s), respectively.

Numerical results for the air streamlines nearby the top left fork are presented in Figure 8. Due to the impact of inertia, most of the air flows in the upper path straightly, while the rest is deflected and flows in the left path. The air flow rate in the upper path is larger than the one in the left path, which increases the overall velocity gradient at the boundary. Furthermore, there exists a large clockwise vortex in the left path, which not only increases the velocity gradient at the boundary but also improves the field synergy between the velocity and its gradient. According to the field synergy principle, the above two reasons result in a large pressure

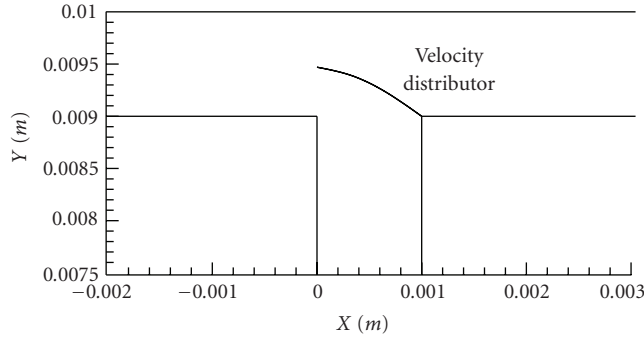


FIGURE 9: Sketch of the velocity distributor position near the top left fork.

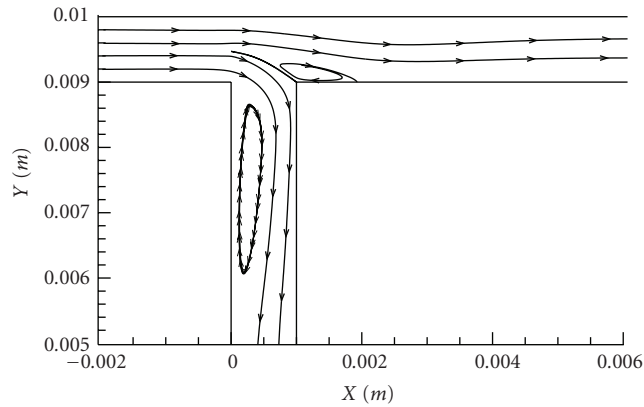


FIGURE 10: Air streamline field nearby the top left fork with a velocity distributor.

drop in the entire flow domain. In this case, the pressure drop is 47.4 Pa.

If a velocity distributor is placed along the middle streamline nearby the top left fork as shown in Figure 9, we will obtain the air streamlines as shown in Figure 10. The air flow rates in the upper and the left paths are nearly the same, which will decrease the overall velocity gradient at the boundary. In the meanwhile, compared with the result without the velocity distributor, the clockwise vortex in the left path is smaller, which reduces the field synergy number of the velocity and its gradient. As a result, the pressure drop is reduced from 47.4 to 44.9 Pa.

6. Conclusions

Due to the same generation mechanism and govern equations, momentum, heat, and mass transfer processes are the three analogous phenomena. Hence, the field synergy principle proposed earlier by Guo et al. [21] is extended from convective heat transfer to convective mass transfer and fluid flow as a unified principle for analyzing and improving the performance of these transfer phenomena.

In convective heat transfer, a smaller intersection angle, that is, a better field synergy, between the velocity and the temperature gradient will lead to a larger heat flow

rate. In convective mass transfer, the overall mass transfer capability can be enhanced by decreasing the interaction angle, that is, increasing the field synergy number, between the velocity vectors and the species concentration gradients for a given fluid flow rate. In fluid flows, the flow drag depends not only on the velocity and the velocity gradient fields but also on their synergy. For a given flow rate or inlet velocity, reducing the synergy between the velocity and the velocity gradient fields over the entire domain and decreasing the fluid viscosity and the velocity gradient at the flow boundary will decrease the fluid flow drag. Several numerical examples are also provided to show the validity and applications of the principle.

Nomenclature

- c_p : Specific heat capacity, $\text{J kg}^{-1}\text{K}^{-1}$
- D : Mass diffusion coefficient, m^2s^{-1}
- \dot{m} : Mass flux, kg m^{-2}
- n : Gradient orientation
- A : Heat transfer area, m^2
- E : Entransy, J K
- F : Volume force, N m^{-3}
- M : Mass source, $\text{kg s}^{-1}\text{m}^{-3}$
- Q : Heat source, W m^{-3}
- P : Pressure, Pa
- S : Surface area, m^2
- \dot{q} : Heat flux, W m^{-2}
- T : Temperature, K
- \vec{U} : Velocity vector, m s^{-1}
- V : Volume, m^3
- Y : Mass friction, kg kg^{-1}
- Nu : Nusselt number
- Pr : Prandtl number
- Re : Reynolds number
- Sc : Schmidt number
- Sh : Sherwood number
- β : Included angel
- ρ : Density, kg m^{-3}
- μ : Dynamic viscosity, $\text{kg m}^{-1}\text{s}^{-1}$
- η : Generalized diffusion coefficient
- ϕ : Universal variable
- λ : Thermal conductivity, $\text{W m}^{-1}\text{K}^{-1}$
- λ_t : Turbulent thermal conductivity, $\text{W m}^{-1}\text{K}^{-1}$
- $\delta_{t,x}$: Thermal boundary layer thickness, m.

Acknowledgment

This work was financially supported by the National Key Fundamental R&D Program of China (Grant no. G2007CB206901).

References

- [1] N. C. Heglund, P. A. Willems, M. Penta, and G. A. Cavagna, "Energy-saving gait mechanics with head-supported loads," *Nature*, vol. 375, no. 6526, pp. 52–54, 1995.
- [2] M. I. Hoffert, K. Caldeira, G. Benford, et al., "Advanced technology paths to global climate stability: energy for a

- greenhouse planet,” *Science*, vol. 298, no. 5595, pp. 981–987, 2002.
- [3] R. K. Thauer, A.-K. Kaster, H. Seedorf, W. Buckel, and R. Hedderich, “Methanogenic archaea: ecologically relevant differences in energy conservation,” *Nature Reviews Microbiology*, vol. 6, no. 8, pp. 579–591, 2008.
- [4] J. Goldemberg, “Ethanol for a sustainable energy future,” *Science*, vol. 315, no. 5813, pp. 808–810, 2007.
- [5] D. R. Bond, D. E. Holmes, L. M. Tender, and D. R. Lovley, “Electrode-reducing microorganisms that harvest energy from marine sediments,” *Science*, vol. 295, no. 5554, pp. 483–485, 2002.
- [6] D. Y. Goswami, “A review and future prospects of renewable energy in the global energy system,” *Advanced Technology of Electrical Engineering and Energy*, vol. 27, no. 1, pp. 55–62, 2008.
- [7] B. K. Sovacool, “The importance of comprehensiveness in renewable electricity and energy-efficiency policy,” *Energy Policy*, vol. 37, no. 4, pp. 1529–1541, 2009.
- [8] A. M. K. P. Taylor, “Science review of internal combustion engines,” *Energy Policy*, vol. 36, no. 12, pp. 4657–4667, 2008.
- [9] J. Jezowski, “Review and analysis of approaches for designing optimum industrial water networks,” *Chemical and Process Engineering*, vol. 29, no. 3, pp. 663–681, 2008.
- [10] L. L. Lai, “A review on energy loss development,” in *Proceedings of the IEEE Power and Energy Society General Meeting (PES '08)*, pp. 1–3, Pittsburgh, Pa, USA, July 2008.
- [11] V. P. Carey, G. Chen, C. Grigoropoulos, M. Kaviani, and A. Majumdar, “A review of heat transfer physics,” *Nanoscale and Microscale Thermophysical Engineering*, vol. 12, no. 1, pp. 1–60, 2008.
- [12] Q. Chen, M. Wang, N. Pan, and Z.-Y. Guo, “Optimization principles for convective heat transfer,” *Energy*, vol. 34, no. 9, pp. 1199–1206, 2009.
- [13] Q. Chen, M. Wang, N. Pan, and Z.-Y. Guo, “Optimization principle for variable viscosity fluid flow and its application to heavy oil flow drag reduction,” *Energy and Fuels*, vol. 23, no. 9, pp. 4470–4478, 2009.
- [14] L. Yang, J. Ren, Y. Song, J. Min, and Z. Guo, “Convection heat transfer enhancement of air in a rectangular duct by application of a magnetic quadrupole field,” *International Journal of Engineering Science*, vol. 42, no. 5-6, pp. 491–507, 2004.
- [15] A. E. Bergles, “Heat transfer enhancement—the encouragement and accommodation of high heat fluxes,” *Journal of Heat Transfer*, vol. 119, no. 1, pp. 8–19, 1997.
- [16] C. F. Ma, Q. Zheng, S. C. Lee, and T. Gomi, “Impingement heat transfer and recovery effect with submerged jets of large Prandtl number liquid. I. Unconfined circular jets,” *International Journal of Heat and Mass Transfer*, vol. 40, no. 6, pp. 1481–1490, 1997.
- [17] L. Cheng and Y. Qiu, “The research of complex heat transfer enhancement by fluid induced vibration,” *Journal of Hydrodynamics, Series B*, vol. 15, pp. 84–89, 2003.
- [18] D. Neumann and A. Dinkelacker, “Drag measurements on V-grooved surfaces on a body of revolution in axial flow,” *Applied Scientific Research*, vol. 48, no. 1, pp. 105–114, 1991.
- [19] L. Gaudet, “Properties of riblets at supersonic speed,” *Applied Scientific Research*, vol. 46, no. 3, pp. 245–254, 1989.
- [20] P.-W. Li, Y. Kawaguchi, and A. Yabe, “Transitional heat transfer and turbulent characteristics of drag-reducing flow through a contracted channel,” *Journal of Enhanced Heat Transfer*, vol. 8, no. 1, pp. 23–40, 2001.
- [21] Z. Y. Guo, W. Q. Tao, and R. K. Shah, “The field synergy (coordination) principle and its applications in enhancing single phase convective heat transfer,” *International Journal of Heat and Mass Transfer*, vol. 48, no. 9, pp. 1797–1807, 2005.
- [22] W.-Q. Tao, Z.-Y. Guo, and B.-X. Wang, “Field synergy principle for enhancing convective heat transfer—its extension and numerical verifications,” *International Journal of Heat and Mass Transfer*, vol. 45, no. 18, pp. 3849–3856, 2002.
- [23] Z. Y. Guo, D. Y. Li, and B. X. Wang, “A novel concept for convective heat transfer enhancement,” *International Journal of Heat and Mass Transfer*, vol. 41, no. 14, pp. 2221–2225, 1998.
- [24] W. Q. Tao, Y. L. He, Q. W. Wang, Z. G. Qu, and F. Q. Song, “A unified analysis on enhancing single phase convective heat transfer with field synergy principle,” *International Journal of Heat and Mass Transfer*, vol. 45, no. 24, pp. 4871–4879, 2002.
- [25] Q. Chen, J. Ren, and Z. Guo, “Field synergy analysis and optimization of decontamination ventilation designs,” *International Journal of Heat and Mass Transfer*, vol. 51, no. 3-4, pp. 873–881, 2008.
- [26] Q. Chen and J. Meng, “Field synergy analysis and optimization of the convective mass transfer in photocatalytic oxidation reactors,” *International Journal of Heat and Mass Transfer*, vol. 51, no. 11-12, pp. 2863–2870, 2008.
- [27] Q. Chen, J. Ren, and Z. Guo, “Fluid flow field synergy principle and its application to drag reduction,” *Chinese Science Bulletin*, vol. 53, no. 11, pp. 1768–1772, 2008.
- [28] W. M. Kay and M. E. Crawford, *Convective Heat and Mass Transfer*, McGraw-Hill, New York, NY, USA, 1980.
- [29] D. B. Guralnik, Ed., *WEBSTER’S New World Dictionary of the American Language*, William Collins, Cleveland, Ohio, USA, 2nd edition, 1979.
- [30] M. Zeng and W.-Q. Tao, “Numerical verification of the field synergy principle for turbulent flow,” in *Proceedings of the International Conference on Energy Saving and Enhancement of Heat Transfer*, Guangzhou, China, October 2004.
- [31] Y. L. He, W. Q. Tao, F. Q. Song, and W. Zhang, “Three-dimensional numerical study of heat transfer characteristics of plain plate fin-and-tube heat exchangers from view point of field synergy principle,” *International Journal of Heat and Fluid Flow*, vol. 26, no. 3, pp. 459–473, 2005.
- [32] J.-A. Meng, X.-G. Liang, Z.-J. Chen, and Z.-X. Li, “Experimental study on convective heat transfer in alternating elliptical axis tubes,” *Experimental Thermal and Fluid Science*, vol. 29, no. 4, pp. 457–465, 2005.
- [33] X. Li, J. Meng, and Z. Guo, “Turbulent flow and heat transfer in discrete double inclined ribs tube,” *International Journal of Heat and Mass Transfer*, vol. 52, no. 3-4, pp. 962–970, 2009.
- [34] Y. P. Cheng, Z. G. Qu, W. Q. Tao, and Y. L. He, “Numerical design of efficient slotted fin surface based on the field synergy principle,” *Numerical Heat Transfer, Part A*, vol. 45, no. 6, pp. 517–538, 2004.
- [35] J.-K. Kuo and C.-K. Chen, “Evaluating the enhanced performance of a novel wave-like form gas flow channel in the PEMFC using the field synergy principle,” *Journal of Power Sources*, vol. 162, no. 2, pp. 1122–1129, 2006.
- [36] Q. Chen, *Irreversibility and Optimization of Convective Transport Processes*, Tsinghua University, Beijing, China, 2008.